UNIVERSITA` DEGLI STUDI DI GENOVA

Facolta` di Ingegneria

Corso di Laurea in Ingegneria Meccanica

Paola Tropea

Tesi di Laurea

THE CERN-LHC SUPERCONDUCTING DIPOLE: ASSEMBLY AND COOL-DOWN DEFORMATION INFLUENCE ON THE MAGNETIC FIELD QUALITY

Relatori:

Prof. Ing. Alessandro Rebora

Dott. Walter Scandale
Dott. Ezio Todesco

Novembre 2000

ACKNOWLEDGEMENTS

I wish to acknowledge Professor Rebora, for giving me the opportunity of carrying out this thesis and for his many useful suggestions.

I wish to acknowledge Walter Scandale and Ezio Todesco for their invaluable help and for the encouragement they provided during the thesis work. Many thanks go also to all the personnel of the LHC/MMS group at CERN, for having given me the possibility of working in a stimulating and pleasant environment.

Special thanks to Alberto Desirelli, Paolo Fessia, Diego Perini, Giancarlo Spigo, Davide Tommasini, and Iouri Vanenkov, for precious technical suggestions. A special thanks to Paolo Ferracin, for his help and patience especially during the first approach with the FEM model.

Thanks a lot to my family and to Roberto for having being so patient in the course of my work and for their constant support.

PREFACE

The work that finally conduced to this thesis has been carried out during a fourteen months stage at CERN (European Organization for Nuclear Research), in the framework of the Large Hadron Collider (LHC) project, now under construction.

I was hosted by the MMS group, which is in charge of the construction of the superconducting dipoles and quadrupoles of the LHC. My supervisor was Walter Scandale, activity leader of the magnet quality in the MMS group. My co-supervisor was Ezio Todesco, also working in the magnet quality section. My home supervisor was Professor Rebora, from the DIMEC (Dipartimento di Meccanica e Costruzione delle Macchine).

My thesis was in part computational and in part experimental. My activity was related for two third of the time to the structural analysis of the dipole, performed with finite element models and for one third to experimentation with the aim of characterizing some crucial dipole components in terms of mechanical and thermal properties.

I was working at CERN in Geneva, but for my experimental activity I had collaboration with the EPFL (Ecole Politecnique Federale de Lausanne), where some measurements were carried out with the help of scientists of the IMAC (Institute de Mesure et Analyse des Contraintes).

The main goal of my thesis was to find correlation between geometry of the magnet and the harmonic contents of the magnetic field generated in the inner aperture. The reason of this analysis was that of determining optimal tolerances for the dipole construction.

The results of my thesis are the following:

- Improvement of the existing FEM model for structural analysis of the dipole
- Experimental determination of the mechanical properties of the superconducting coil
- Determination of tolerances for the collar and the coil sizes.

The work of the thesis was partly included in the following publications:

[1] Ferracin P., Scandale W., Todesco E., Tropea P., 1999, A method to evaluate the field-shape multipoles induced by coil deformation, 1999 Particle accelerator conference, New York: 3206-3208

[2] Scandale W., Todesco E., Tropea P., 1999, Influence of mechanical tolerances on the field quality in the LHC main dipoles, IEEE Transactions of applied superconductivity, 10/1: 56-59

[3] Scandale W., Ferracin P., Todesco E., Tropea P., Vanenkov I., 2000, Modeling of the thermo-mechanical structure of the main LHC dipole and its influence on field quality, 7th European particle accelerator conference, Vienna: 330-332

INDEX

1 INTRODUCTION

In the Large Hadron Collider, the new circular accelerator under construction at CERN (European Organization for Nuclear Research), superconducting magnets generate the high magnetic field necessary to bend and focus particle beams. For high-energy accelerators like the LHC, high particle beam intensity and high luminosity represent the most demanding achievements. In addition, a high magnetic field quality is required to assure stable particle trajectories thus allowing to reach the desired beam intensity.

In particular, in the main LHC magnets (dipoles), used to bend the particle into the desired circular orbit, the ideal field distribution should be perfectly constant. More realistically, any multipolar component must be kept small, within values determined by beam stability studies.

Indeed, magnetic field generated by superconducting magnets is affected by errors with respect to the ideal one. The field quality depends on many factors, like design geometry, induced currents effect, iron saturation and geometry errors during fabrication. In a superconducting magnet, the shape and the position of the conductors mainly determine the magnetic field distribution Nominal geometry demands a certain disposition of the superconducting cables in the magnet cross section in operating conditions, i.e. after assembly and cool-down at 1,9 K. If nominal geometry is respected, all the multipole values (harmonics) should be sufficiently small to avoid detrimental effects for beam stability.

Field harmonics have systematic components, which are identical in all dipoles, and random ones, which vary from dipole to dipole. Systematic harmonics are due to coil design or to systematic errors during production. Instead, random errors are due to tolerances on dipole components and on assembly procedure.

In this thesis we analyze the problem of the field quality in the main LHC dipoles concentrating our attention on the effects of geometry design and errors. To evaluate these effects, structural studies on the dipole cross section are requested. They must provide an estimate of the conductor positions in operational conditions. These estimates are obtained with a finite element model developed with the ANSYS® code, in which the geometry of the dipole and the thermomechanical properties of the components have to be described. Specific experiments are needed in order to quantify the mechanical properties, since the materials involved are non-standard. In fact, coils are built up using superconducting cables, wrapped by polyimide tapes, and copper spacers, therefore they can be considered as composites.

Magnetic field components, describing the field distribution, result from the harmonic analysis around the axis of the magnet. To obtain the field shape a magnetostatic code developed at CERN, ROXIE, is used. In our specific case, the output of the mechanical FEM model provides the description of the conductor position, which is used as the input for the magnetostatic computations. Indeed, no available program allows to compute with the required precision both the mechanical deformations and the magnetic field shape.

Existing FEM models have been used to evaluate the structural behavior of the magnet, but they could not evaluate the cable displacement with a precision of the order of some tenths of millimeter, required for a good estimate of the field shape harmonics. An estimate of field shape has been made using a "rigid" model of the coils, where conductor blocks are rigidly translated. While a rough estimate can thus be obtained, such a model does not take into account the displacements of the individual conductors nor the block deformations, therefore it is insufficient [1].

The usual way to calculate the effect of geometry error on the field quality is to change one by one the geometrical parameters of the model and to evaluate the consequent effect on field shape. In this way, one can build sensitivity matrices, which focus the relation between geometrical parameters and field components. This method permits to identify the area of the magnet with a paramount influence on field quality hence to specify in the most reasonable manner the tolerances for the mechanical components.

A more global manner to investigate the influence of mechanical tolerances on field shape consists in varying the geometrical parameters all together, selecting the variations on the base of the expected statistical distribution. This method is usually quoted as Monte Carlo simulation and allows validating the compatibility of the tolerances selected for the various components.

In this thesis, we will describe the improvements made on the finite element model of the dipole cross-section, the corresponding mechanical tests used to determine the material properties and the results of the analyses performed using the new model.

In Chapter 2, a description of the LHC layout and of the magnets is given and the problem of the field quality is treated. In Chapter 3, the mechanical model built up with the FEM code, its structure and the material properties values inserted in it are presented. A brief description of the model used to compute the magnetic field, built up with the magnetostatic code, is given at the end of the same chapter. In Chapter 4, all the measurements taken to evaluate the material properties are discussed, together with the computations used to extrapolate useful data. In particular, coil Young modulus and prestress loss from warm to cold temperature are treated, giving also a brief description of the tools used to make such measurements. In Chapter 5, results of the computations made using the model are reported, both for simple parametric analysis and for Monte Carlo simulation. Practical consequences on the field quality correction procedures are given too. In the last chapter, some conclusions are drawn. In the Appendix A and B, technical problems related to the finite element modelization are shown.

2 THE CERN-LHC PROJECT AND ITS MAGNET

2.1 The Large Hadron Collider

The Large Hadron Collider is a circular accelerator under construction at CERN (European Laboratory for Particle Physics). It will take the place of LEP (Large Electron Positron collider), inside the 27 Km underground tunnel in the Geneva area. The LHC is designed to collide protons at high center-of-mass energy (14 TeV), but it will also be able to collide heavy nuclei (Pb-Pb) [4].

Goals for the LHC accelerator are a high particle energy and a high number of observable objects, the so-called "physic reach" of the collider.

A high magnetic field is required to give high-energy particles the necessary curvature. Superconducting technology in magnet construction, providing a much higher magnetic field and a reduction of operating costs, has been chosen [5]. Other three accelerators in the world already use this technique: Tevatron, at FNAL (Fermi National Accelerators Laboratory), HERA, at DESY (Deutsches Elektronen-Synchrotron) and RHIC (Relativistic Heavy Ion Collider) at Brookhaven.

In the Large Hadron Collider, particles will run in a ring with ultra-high vacuum (10^{-9} bar), where a sequence of superconducting cavities will accelerate them up to 7 TeV and magnetic field will bend them along the nominal trajectories. This field will be mostly dipolar and the main magnets inside the accelerator will be superconducting dipoles.

The force applied on every single particle running inside the accelerator is given by the Lorentz equation:

$$\overline{F} = q\overline{E} + q\overline{v} \times \overline{B} \qquad (2.1)$$

where:

q = particle electrical charge;

$\overline{E}$ = time dependent electrical field (sinusoidal);

$\overline{v}$ = particle speed;

$\overline{B}$ = magnetic field.

This force has two different components, the first one depending on the electrical field, the second one on the magnetic field. Inside the cavities, only the tangential component depending from the energy is present, while inside magnets there is only the radial component that gives particle trajectory the necessary curvature. To keep the particles on the circular orbit, the magnetic field inside dipoles must satisfy:

$$B = \frac{p}{qR}, \tag{2.2}$$

where p is the momentum of the particle.

Employing high field superconducting magnets, with an operation dipole field of 8.3 T, the LHC will be able to collide protons at 7 TeV/c and heavy nuclei at 1150 TeV/c. Superconductors for such a high magnetic field should retain a large current density in a high field region. Niobium titanium (NbTi) conductors are adequate for the purpose provided they are cooled down at the very low temperature of 1.9 K with superfluid helium. Thin filaments are used to reduce as much as possible the persistent currents which distort the magnetic field, especially at the injection of the particles, when the field is 0.54 T, namely sixteen times lower than the top field [6].

The number of events during particle collision is directly proportional to the luminosity. Providing a high luminosity, it is possible to increase the so called “physic-reach” of the collider, namely the mass of observable objects, for the given proton energy. Since particles are grouped in about 3000 bunches, i.e. clouds of about 10^{11} protons each, before being injected in the LHC, while defining the following dimension we refer it to a bunched beam. The luminosity for such a beam is given by:

$$L = \frac{fkN^2}{4\pi\sigma_x\sigma_y}, \tag{2.3}$$

with:

f = particle revolution frequency;

k = number of bunches per beam;

N = number of particles per bunch;

σ_x, σ_y = beam radii at the collision point expressed in r.m.s. value of the transverse spatial distributions, assumed to be gaussian.

LHC will provide a luminosity of 10^{34} $cm^{-1}s^{-2}$ for proton-proton collisions and a value of 10^{27} $cm^{-1}s^{-2}$ for heavy ion physics. There are two principal limits for luminosity. The first comes from the beam-beam interaction, due to the action on the particles of one beam produced by the electromagnetic field of the other beam. The other finds its origins in the interaction of the beam with the vacuum chamber walls, which produces a destabilizing effect when the beam current exceeds a given limit. They can be reduced by a strong feedback system.

High energy and luminosity are somehow correlated. To obtain high energy a high magnetic field is requested. Superconducting technology employed for such a goal takes to non-negligible errors on the magnetic field. If the field is different from the ideal dipolar one, at injection, where the beam has a large size, non-linear effects generate a particle dispersion and an emittance increase. Particle loss must be controlled using a collimation system, to avoid magnet overheating and consequent transition to normal condition status of the conductors. Emittance increase indeed, can not be controlled and cause a luminosity loss when the beam has reached the requested high energy.

For such reasons, field quality is a problem of utmost importance in superconducting magnets. In LHC dipoles, the relative deviation from the ideal dipole field should not exceed a few parts in 10^{-4}. Moreover, it is not trivial to maintain such a high precision.

While in resistive magnets, field quality is defined by the shape of polar expansions in the ferromagnetic sheets and by iron yoke shape, in superconducting magnets, current lines can be assimilated to conductors, from whose positions field quality depends. This is the reason why the arrangements of current conductors and the precision of coil geometry are of utmost importance for the LHC magnetic field quality [6].

2.2 Accelerator layout and experiments

Particles are injected inside the LHC by a system constituted by four different machines (see Figure 2.1). The first beam is produced inside a Linac (Linear proton accelerator) at 50 MeV and it is sent to the PS (Proton Synchrotron) Booster, where it is accelerated to 1.4 GeV. After this procedure, protons are grouped in packets (called bunches) of 10^2 particles at 25 GeV, each one 7.5 m distant from the other.

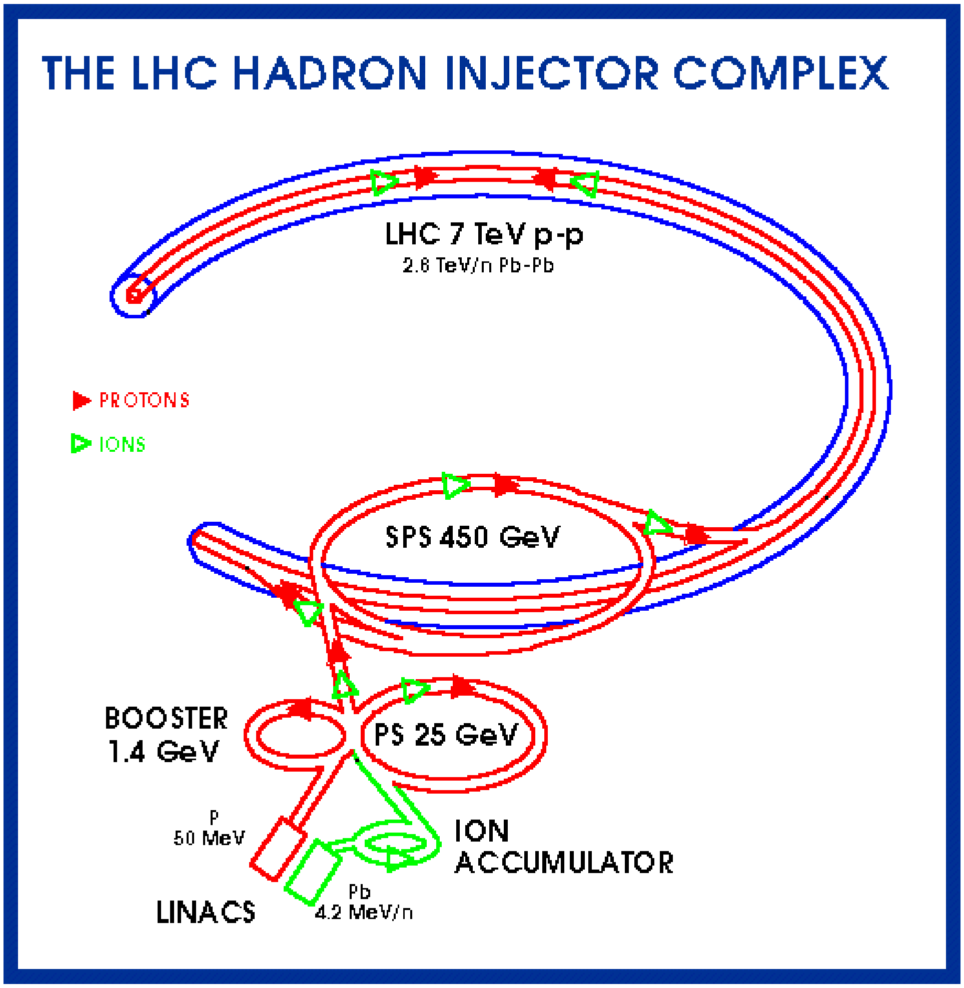

Figure 2.1: LHC layout

Three trains of 81 packets of particles each are transferred to the SPS. Here the beam is accelerated to 450 GeV and sent to the LHC. Twelve cycles of SPS are necessary to obtain two proton beams rotating in opposite directions. The LHC structure shows a succession of eight arcs separated by eight straight sections (IR). Each straight zone is approximately 500 m long and is used for experimental insertions or different utilities for the accelerator (see Figure 2.2).

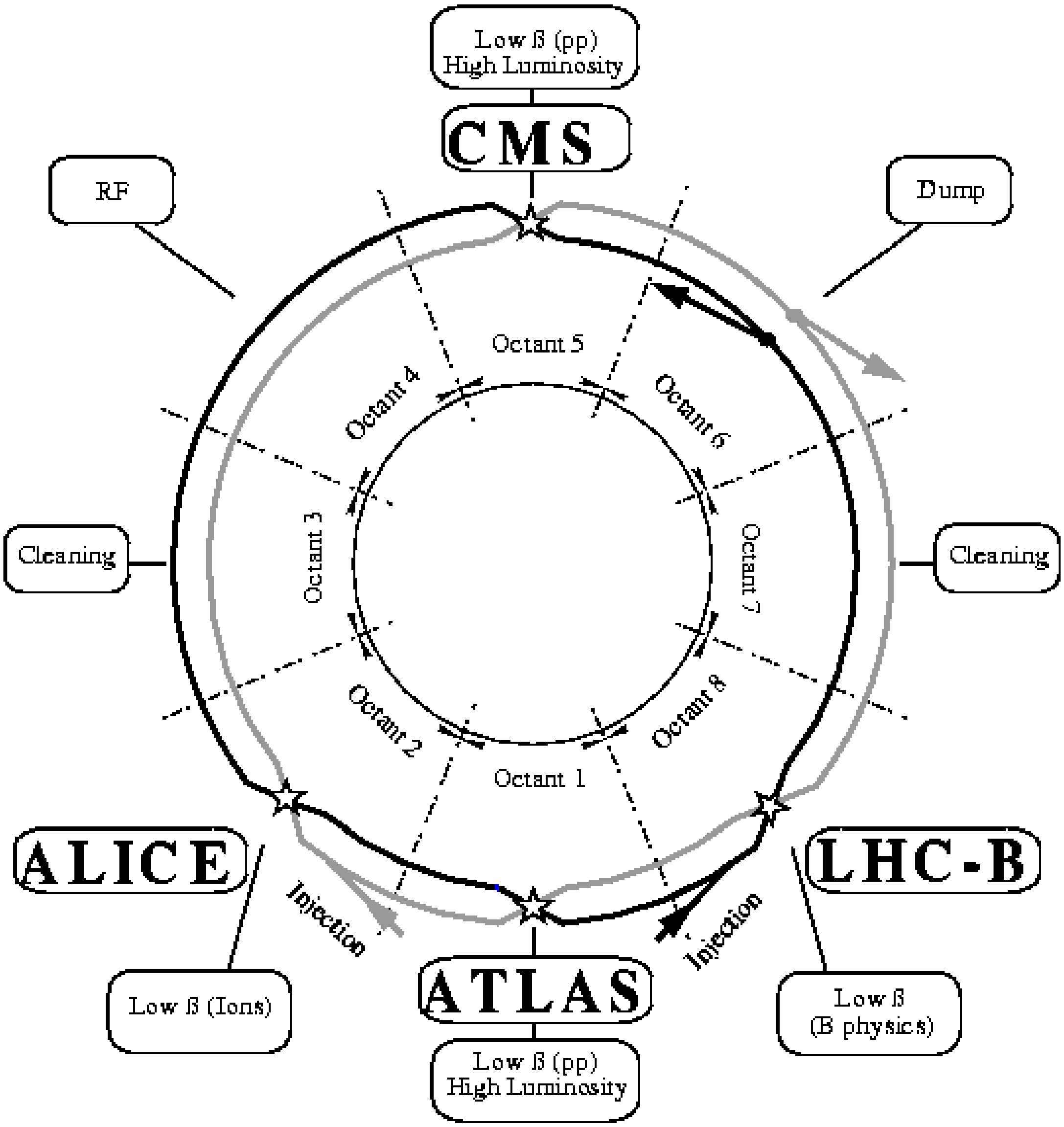

Figure 2.2: Experiments for the LHC

In correspondence to point 1 (ATLAS) and point 5 (CMS) there are two high-luminosity insertions. Two other experimental insertions are located at point 2 (ALICE Pb ions) and point 8 (B physics). These latter straight sections also contain the injection systems.

The beams, which are 194 mm distant one from the other along the most of the path, cross from one ring to the other only at these four locations. Two beam collimator systems, using only classical magnets, are placed at insertion 3 and 7. Insertion 4 contains the Radio Frequency systems, separated for the two beams, used to accelerate beam particles. The straight section at point 6 contains the beam dump insertion, where remaining particles are ejected after collision [4].

Each of the eight arcs is composed of 23 arc cells, giving a total arc length of 2456.160 m. Two identical half cells compose each single arc-cell (see Figure 2.3). The single cell consists of a string of three 14.3 m twin-aperture dipoles and one 3.10 m quadrupole. The separation between the dipoles is 1.46 m, which includes 520 mm for connections between the cryostats, while the quadrupole is 2.42 m distant from the dipoles. Sextupoles and decapoles are located on the right and left side of the cell. On the left side of the quadrupole assembly, there are a beam position monitor (BPM) and an octupole, and on its right side a combined sextupole/dipole corrector.

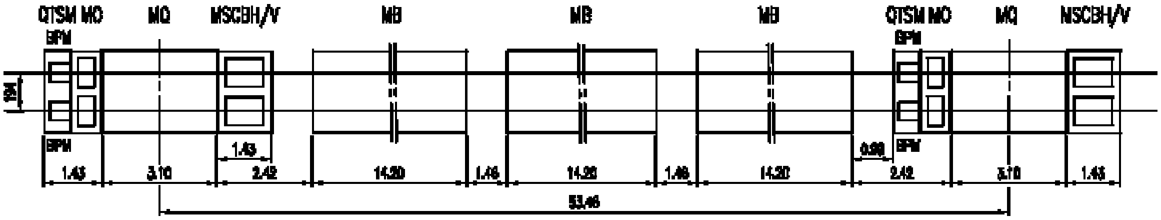

Figure 2.3: Cell scheme

Inside the LHC, superconducting magnets aligned with a precision of 0.3 mm are used to bend particle trajectories, and to stabilize them. Namely:

- Dipoles create the main vertical magnetic field, perpendicular to the particle direction, used to deflect particle motions to circular trajectories.

- Quadrupoles produce a field that is null in the center of the vacuum chamber and linearly dependent from the distance to the center, whose purpose is to focus the beam. Quadrupoles have focusing effect only in one plane, whilst they defocus in the orthogonal one (Figure 2.4). For this reason, a sequence of quadrupole focusing on one plane, dipole and quadrupole focusing on the orthogonal plane is developed. The overall problem is focusing on both planes.
- Sextupoles create a null field in the center, quadratic proportional to the distance, used to control chromaticity effects. These effects are errors that are induced by the quadrupoles focusing power and depend on small variations in the particle energy.
- Octupoles make the tune dependent on the amplitude, which is exploited to improve the stability [4].

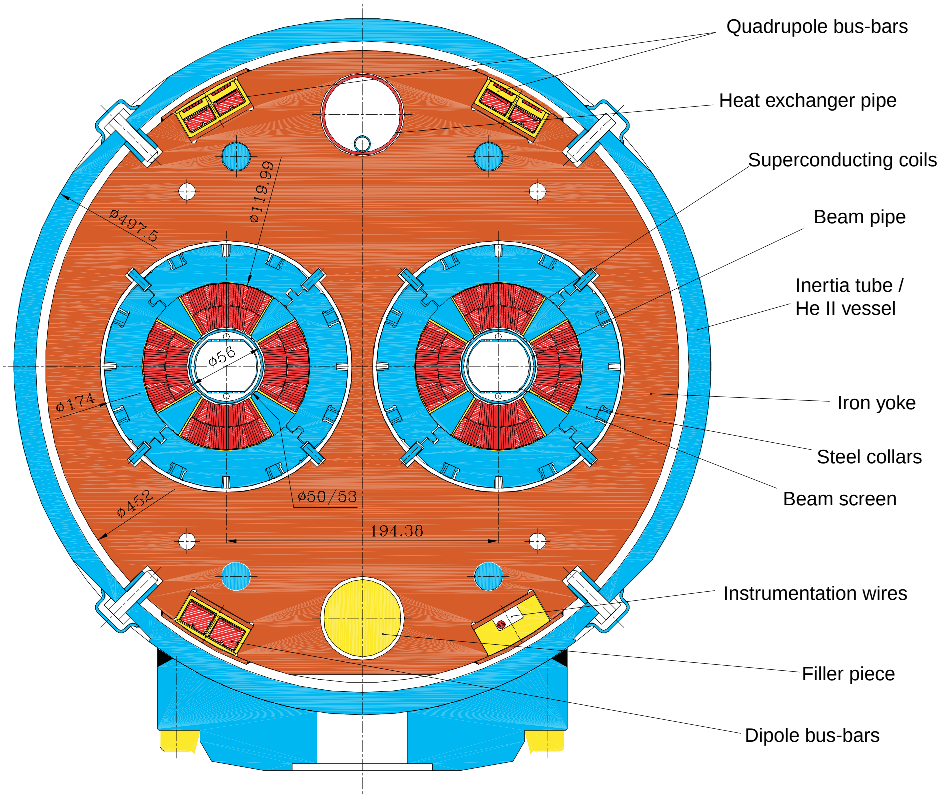

Figure 2.4: Quadrupole cross section

2.3 The magnets

The three large accelerators already mentioned, i.e. Tevatron, HERA and RHIC, use magnets built with NbTi superconductors, working at a temperature of about 4.2 K. To reach this temperature superfluid helium is used [4].

Since the LHC operational field (8.33 T) is quite higher than in Tevatron, HERA and RHIC (4, 5 and 3.45 T respectively), in this case it is not possible to use the same technology. To tolerate such a high field, NbTi superconductors have to be cooled down at about 2 K. This technique has already been successfully applied to the French Tokamak TORESUPRA in operation at Cadarache.

Since helium takes the so-called superfluid state below 2.17 K, working at 1.9 K, below the lambda point of helium, a very low viscosity is reached. Thanks to this property, it is possible to make the helium circulating inside the magnet in a uniform way and it permit a drastic reduction of the helium flow through magnets. Moreover, if the pressure is maintained at 1.6 mbar, helium provides also a very large specifics heat (4000 J/kg K).

On the other hand, the enthalpy of all metallic parts and in particular of the superconducting cables is reduced by an order of magnitude cooling down between 4 k and 1.9 K, with a consequent temperature rise for a given deposit of energy. For this reason, particular care must be taken in limiting conductor motion. In fact, the magnetic field generates Lorentz forces on the conductors, which are proportional to the square of magnetic field intensity (B). Moreover, the stored electromagnetic energy increases with it. This is why strong force-retaining structures and elaborate quench protection systems are of the most importance for superconducting magnets.

Proton-proton colliders require two separate beam channels with fields equal in strength but opposite in directions. For the LHC, the compact `two-in-one' design is adopted, whereby the two beam channels and their corresponding sets of coils are inserted in a unique structure and in a single cryostat [7].

2.4 The main dipole

2.4.1 General description

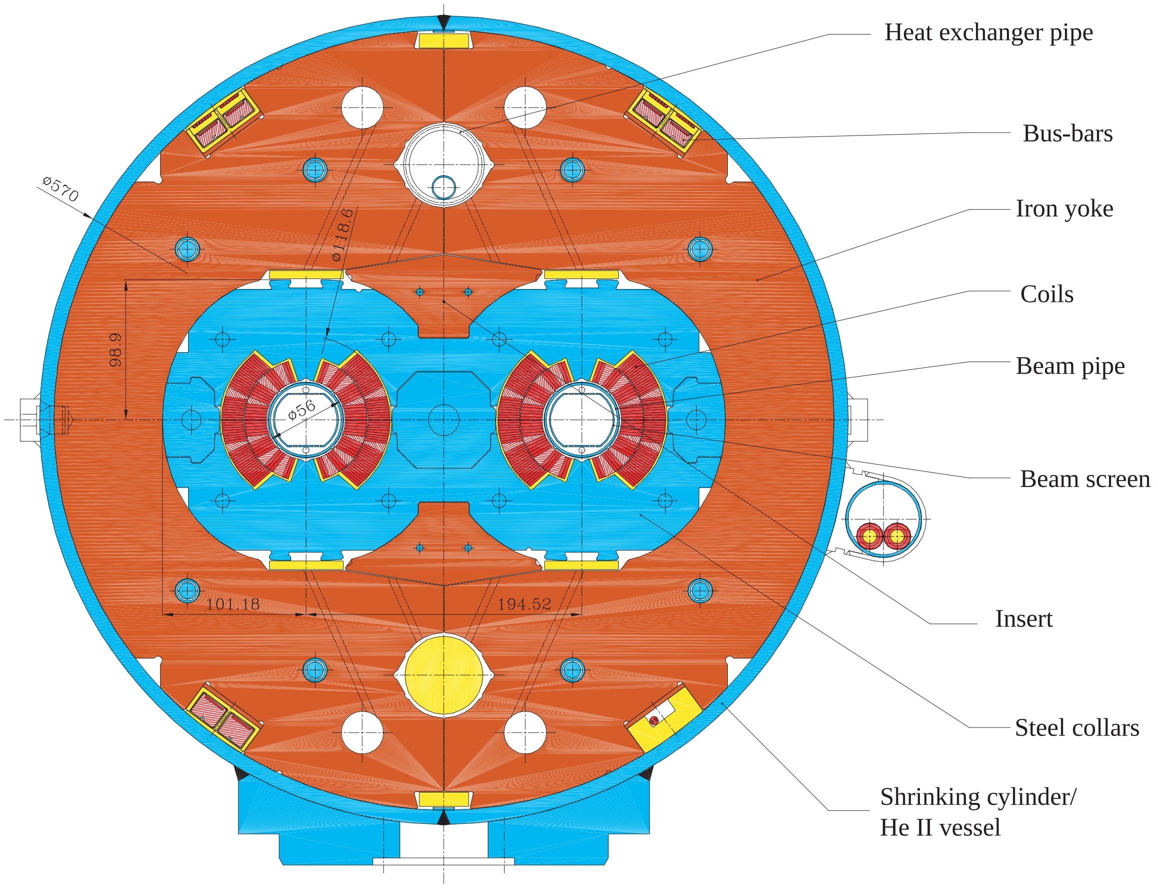

Figure 2.5: Main dipole cross section

The design of LHC main dipole is based on a twin aperture structure clamped by a unique force retaining structure. Coils of opposite polarity are inserted in each aperture. Axes distance between the two centers of the apertures is 194.52 mm (Figure 2.5). Coils, whose inner diameter is 56 mm measured at 293 K, are made by NbTi superconductors operating in superfluid helium at 1.9 K [7].

Two winding layers of cables, divided into six blocks compose the coils. Wedge-shaped copper spacers are also inserted between blocks of conductors to produce the desired field quality. To avoid conductors moving under the action of electromagnetic forces, coils are clamped by stainless steel collars, iron yoke and a shrinking cylinder. They form the force containment structure, giving the necessary azimuthal prestress to the coils.

The whole part of the magnet included inside the shrinking cylinder (i.e. the cold mass, see Figure 2.6) is cooled down to 1.9 K and is kept at this temperature while working with superfluid helium circulating inside. The cold mass also contains correction sextupoles and decapoles, mounted on both the end of the dipole.

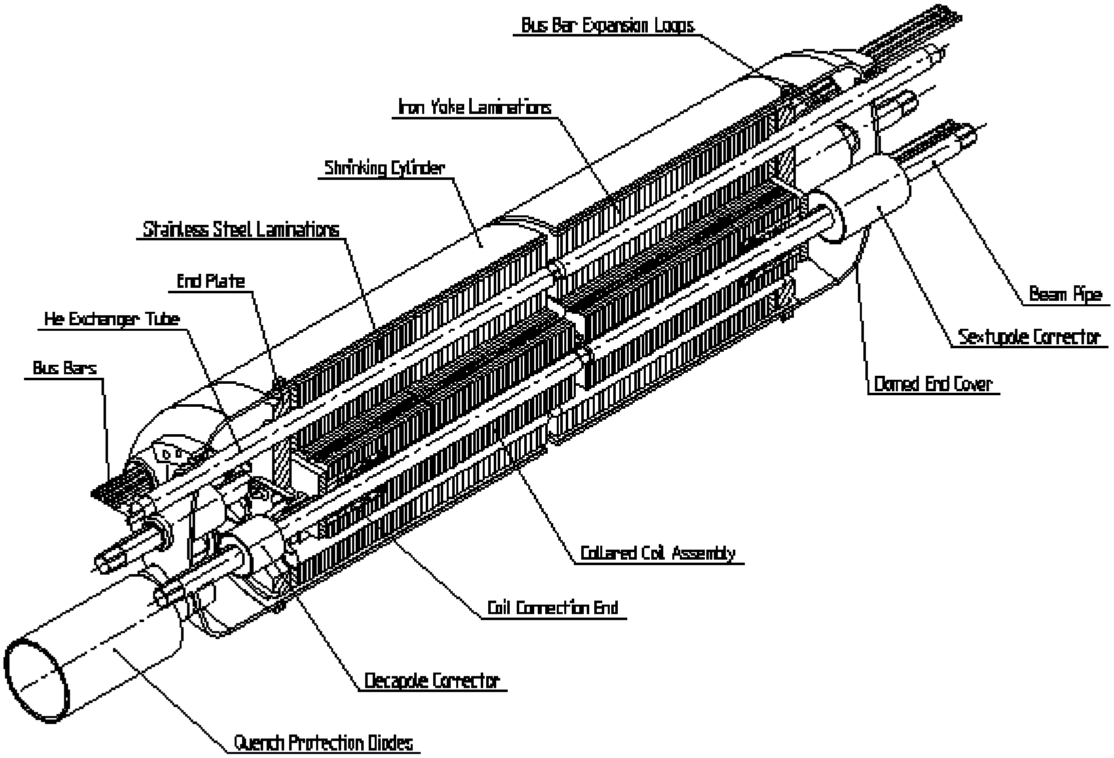

Figure 2.6: Cold mass longitudinal section.

The cold mass is installed inside a cryostat, whose main components are a radiation shield, a thermal screen and the outer cylindrical wall of the vacuum vessel. The shield, cooled by 5-20 K helium, is used to reduce heat load on the cryogenic system. To close the cold mass, two end covers are welded to the shrinking cylinder. They leave a passage for the beam vacuum chambers, a heat exchanger tube, and two pipes containing the main and the auxiliary electrical connections. The cryostat is supported by three feet made of composite material. The central one is fixed to the vacuum vessel, while the others can move on rollers to follow thermal contractions and expansions. The cold mass is bent to a 2700 m radius of curvature to match the beam paths [5].

2.4.2 The superconducting cables

On the transverse cross-section of LHC dipole coils, it is possible to see two layers of cables distributed in six blocks for each quadrant (see Figure 2.7). Cables have a trapezoidal shape, with angles of 1÷4 degrees between bases and oblique sides. These angles, called “keystoning” angles, are used to reproduce the shape of an arc in cable position, in order to have a more stable structure. They also provide more degrees of freedom in packing cables into blocks.

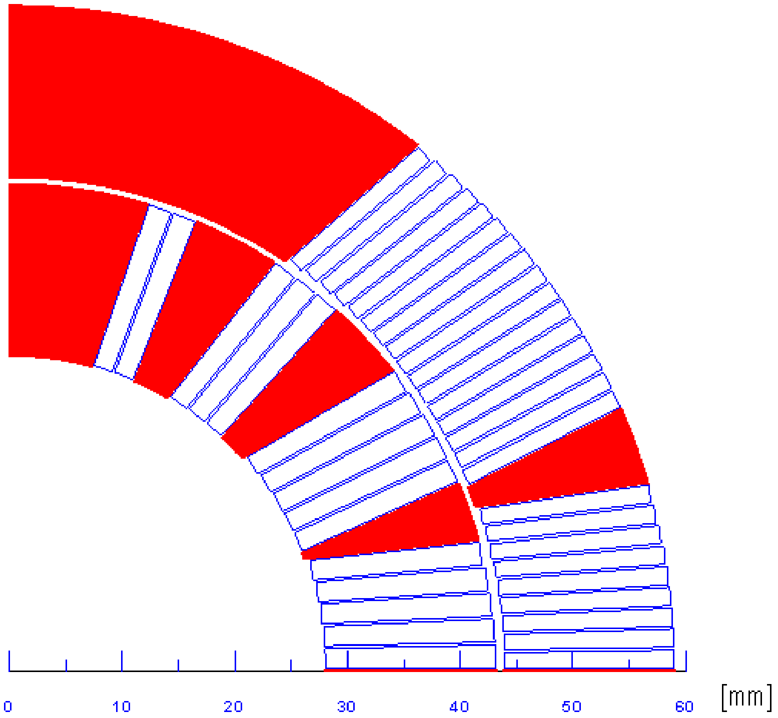

Figure 2.7: Cable distribution inside coil quadrant

Each cable is composed of a certain number of strands, 28 for the inner coil cables (each one with a diameter of 1.065 mm), 36 for the outer ones (diameter of 0.825 mm). Niobium-Titanium filaments inserted in a copper matrix form each strand. Filaments inside strands have a diameter of 7 μm (inner layer) and 6 μm (outer layer): this is in fact the better size to optimize field quality at the injection. Moreover, the lower is the filament size, the higher is the current it can carry. Different dimensions for inner and outer layers come out from the desired grading of current density, calculated for optimum use of the superconducting material. The copper matrix has first the function of a mechanical structure. Furthermore, it has a protective function on thin filaments in case of overheating [8].

A superconductor stays in the superconducting state when the temperature, the magnetic field, and the current density are below their critical surface. If this condition is not verified, for instance if temperature increases due to friction caused by conductor motion under the influence of Lorentz forces, the magnet "quenches". A quench is the transition from the superconducting to the normal state.

Since niobium titanium superconductors have high resistivity in the normal state, copper serves as an electrical by-pass. In fact, it can take over current from filaments when they are in normal state, avoiding damages on the superconducting material. To avoid superconductors overheating and consequent damage in case of quench, it is also necessary to stop current delivering. The maximum temperature T_{max} reached by the conductor after quench depends on the time employed to stop current and on the inductance of the cable itself. For the LHC dipoles, it is necessary not to reach a temperature higher than 300 K, and for this reason current delivering should stop in a time shorter than 1 second. Because of the inductance L that characterizes the magnet, current reduction creates inside the coils a difference of potential of this value:

$$V = L\frac{dI}{dt}\,. \tag{2.4}$$

To avoid electrical discharges, which could destroy the coils, cables are electrically insulated with three layers of polyimide tape, coated with an epoxy adhesive (see Figure 2.8)[5].

The first two layers are bent to be superposed one to the other for half of the cable, to guarantee necessary insulation. The last layer is constituted of a tape with an adhesive surface on the external face spiral winded with a spacing of 2 mm, to permit helium circulation. Adhesive is used to glue cables in blocks.

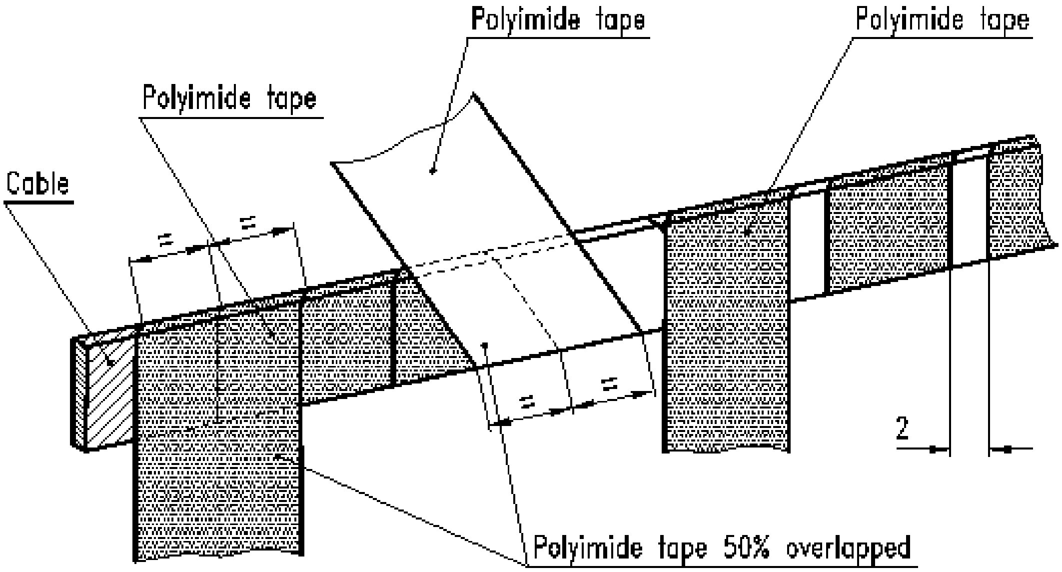

Figure 2.8: Polyimide tape layers on cables.

2.4.3 The coils

The coil is shaped to make the best use of a superconducting cable and to produce a dipole field of the best possible homogeneity over the whole range of its operational excitation. The conductor distribution in one coil quadrant was shown in Figure 2.7.

During operation, coils are heated by particles deviating from the nominal trajectory, synchrotron radiation and beam image current intercepted by the beam screen. An additional dynamic heat load results from losses during magnet ramping. This heat increases the superconductor temperature, which reduces the magnet-operating range. Particular care has therefore to be taken to provide cable insulation sufficiently porous to let the superfluid helium carry away the heat. To avoid short-circuits the insulation must also be robust, in order not to break during winding and curing.

Satisfactory shapes were determined using the approach of the minimum strain energy, in combination with empirical methods. Coils composed of two constant thickness layers with graded current density have been chosen. The two layers are joined together in the part of the inner cable that crosses over from the inner to the outer layer (ramp-splice) and are soldered to the outer layer cable.

To stabilize and reinforce the coil leads, copper strips are soldered to the superconducting cable. The amount of copper complies with the permitted maximum temperature and the discharge time of the system. The coil layers are radially separated by an insulating material. It is a perforated glass-epoxy spacer, used to provide channels for circulation of the cooling helium. The ground insulation is composed of superposed polyimide film layers and includes quench protection heaters. A slotted fiberglass epoxy net is the adopted solution. The coils require additional insulation between poles and for the collars sitting at ground potential (Figure 2.9). The ground insulation is composed of several polyimide film layers, cut azimuthally and longitudinally for reasons of assembly.

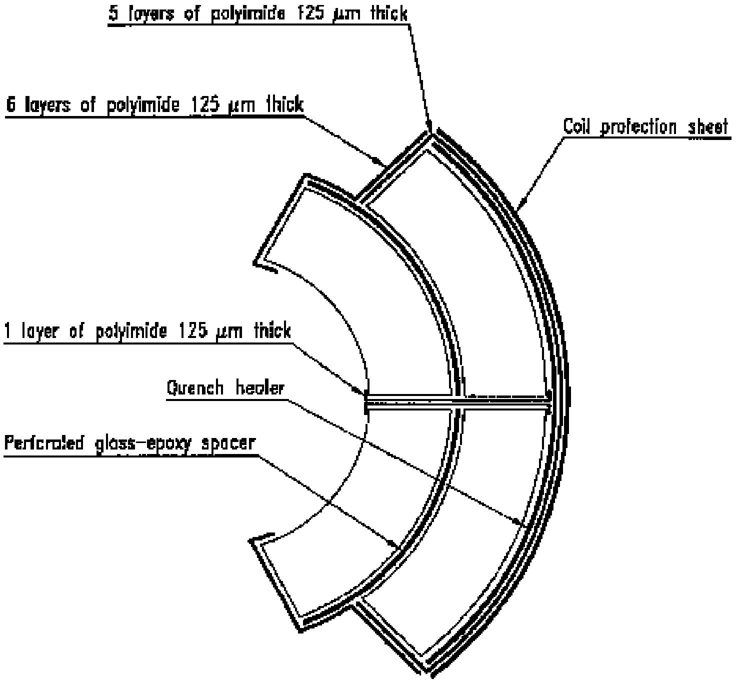

Figure 2.9: Coil protective and insulating sheets between coil layers.

Besides its electrical scope of preventing shorts from coil to coil and from coil to ground, it also has the mechanical role of providing good slip surfaces. They are necessary during collaring, such that both azimuthal and radial preloads are adequately distributed between coils and collars, to avoid the deterioration of the insulation.

Quench heaters are placed between the outer coil layers and the insulation to ground. They consist of stainless-steel strips, with about half of the length intermittently copper-clad (0.25 m with copper cladding alternating with 0.25 m without copper cladding). In case of quench, they rapidly heat up the conductors through the thermal barrier of the insulation.

Coil protection sheets, located between the outer layer ground insulation and the inner collar surface, prevent damage due to contact with the serrated edges of collars. Moreover, the coil protection sheets help to avoid wrap breakdown and provide a continuous support to the conductors. A good slip surface between the collars and protection sheets is provided by coating the sheet with dry lubricant.

Collaring shims, made of fiberglass, are located at the layer poles. The inner one is inserted in a stainless steel support called shim retainer. Shims are used to prevent damage due to collar contact during compression and to better distribute the azimuthal stress between the two layers of the coil.

After winding, each coil layer is heated in a curing mould, where the adhesive polymerizes. The mould should have a mechanical precision of ± 10 μm, because it gives coils their final dimension and shape. Winding and copper wedges are first heated at 130 ^{0}C, under a pressure of about 10 MPa. After a certain time, the pressure is increased up to 80÷100 MPa and temperature rises up to 190 ^{0}C whilst the coils are compressed in a certain size shape. External insulation layers are glued one to the other thanks to polymerization and, once at room temperature, it helps coils maintain a compact if not rigid structure [9].

2.4.4 The mechanical structure

The mechanical structure of the dipoles is designed to withstand the high forces generated in the magnet during operation and to limit as much as possible the coil deformation over the range of operation. Materials used for the most highly stressed components have, therefore, a high loadbearing capacity, high elastic moduli, good fatigue endurance and a good behavior at cryogenic temperatures down to 1.9 K. The coil support structure is formed by:

- Austenitic steel collars with two apertures. The collars are made of 3 mm thick high-strength stainless steel sheet. Coils are assembled inside the collars in a press at room temperature, so that, when force is released, an azimuthal compression prestress of about 60-70 MPa is present on them.
- An iron yoke split into two at the vertical symmetry plane of the twin-aperture magnet. The gap between the two parts is closed by the cylinder during assembling. The yoke is made of 6 mm thick low-carbon-steel laminations.
- An austenitic steel outer cylinder. This part is welded under pression around the iron yoke in such a way that the required pre-stress is applied to the half-yokes.

When current is given to the coils, they must be compressed to avoid any sudden movement of the conductors. Displacements and deformations of the coils must be limited as much as possible to have the most stable magnetic field. The necessary stiffness of the whole structure is guaranteed by:

- the welding of the cylinder;
- a good contact between the iron yoke and the collars.

All component dimensions, materials, imposed pre-stress and gap dimension must be carefully determined. Coils have to be compressed, but it is also important not to force too much, in order to avoid creep of the insulation and of the copper. Except for a short time during collaring operation, stress inside the coils should always be under 100 MPa. This solicitation happens when, inside a 15 m long press, collars are forced around coils to obtain an average compression of about 70 MPa both on the inner and the outer layer. Figure 2.10 show collars clamped on coils. During the collaring process, the compression of the coils can be 40-65% higher than the final required value depending on the method used to apply the load of the press. In fact, once the press force is released, the compressed coils expand the collars and part of the pre-stress is therefore lost. The shrinking cylinder is welded around the iron yoke, with a tensile stress of about 150 MPa. The greatest part of the force exerted by the shrinking cylinder is applied to the collar/coil assembly, that is a little deformed by it. To avoid a dangerous overloading of cables and insulation, a slot in the collar post is foreseen so that it behaves as a spring, releasing the pressure at room temperature, tracking the coil deformation, and shrinking during cooling and energizing.

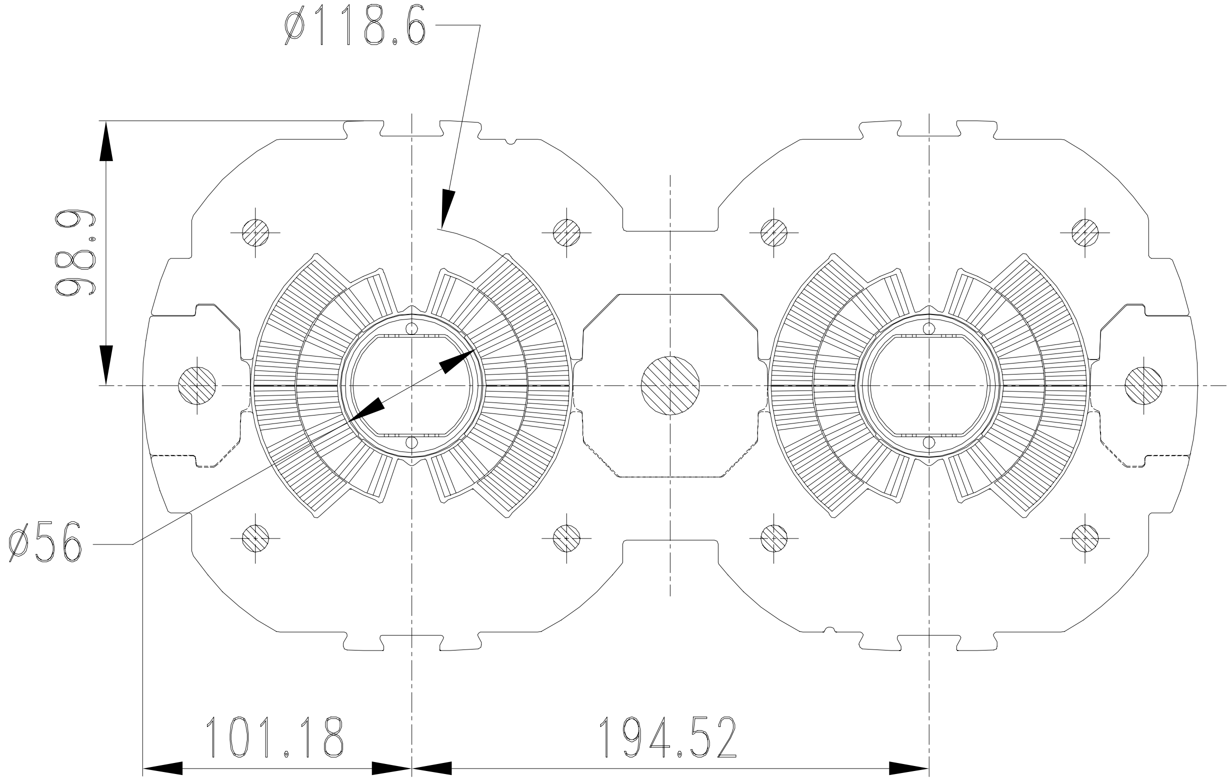

Figure 2.10: Coil and collars assembly.

During excitation, the iron gap stays closed and there is practically no change in the outer cylinder stress. The outward electromagnetic force (1700 N per mm length, per quadrant for a 8 T field) is shared between the collars and the outer structure. The radial deformation in the median plane of the collared coils at this field excitation is about 0.04 mm.

Something different happens to the coil ends, thanks to the bending of blocks of cables. The ends are mounted inside the collars with much lower pre-stress (around 20-30 MPa in the azimuthal direction). In this region, part of the iron yoke is replaced by non-magnetic material in order to decrease the field. The longitudinal resultant electromagnetic force is partly transmitted from the coils to the collars, yoke, and cylinder by friction. The remaining part directly loads the thick end plate.

2.5 MAGNETIC FIELD QUALITY

Considering LHC magnet dimensions, we can notice that their length is considerably bigger than their aperture, so that conductors run parallel to the beam over the longest part of the magnet. Therefore, it is possible to consider the magnetic field as essentially two-dimensional and apply to the magnetic field the study reported in reference [10].

To study the magnetic field inside the magnet, we consider a cylindrical coordinate system in the center of the aperture, with the *z*-axis along the axe of the magnet. We suppose to have a current, positioned in the center of the reference coordinate system, which is flowing exactly along *z*-axis in its positive direction.

We can write the magnetic field generated by this current, creating concentric circles around the axis, in a generic point distant *r* from the *z*-axis:

$$B_\vartheta = \frac{\mu_0 I}{2\pi r}, \tag{2.5}$$

where:

μ_0 = permeability of the dielectric,

I = current density.

The vector potential generated by this current has only a *z* component:

$$A_z(r,\vartheta) = -\frac{\mu_0 I}{2\pi}\ln\left(\frac{r}{l}\right), \tag{2.6}$$

where the quantity *l* is only an arbitrary number, introduced here to make the argument of the logarithm dimensionless. Taking the radial derivative, we obtain:

$$B_\vartheta = -\frac{\partial A_z}{\partial r} = \frac{\mu_0 I}{2\pi r}. \tag{2.7}$$

If we now assume that the current filament is again parallel to the *z* axe, but it is not situated in the center of the aperture, as in Figure 2.11, the equation changes a little.

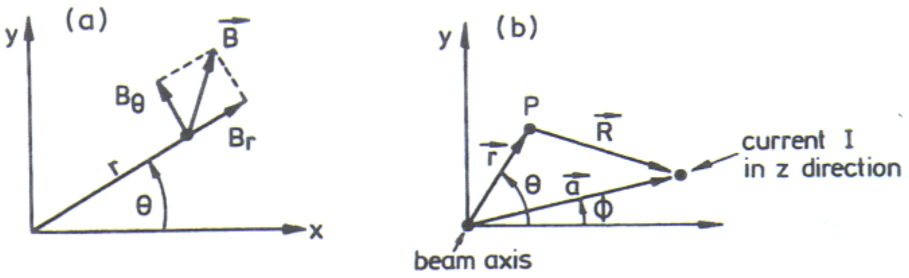

Figure 2.11: Reference coordinate system and positions of current and magnetic field.

A filament placed in a generic position ($r = a$, $\theta = \varphi$), in the r, θ plane, generates a magnetic field whose potential vector is:

$$A_z(r,\vartheta) = -\frac{\mu_0 I}{2\pi}\ln\left(\frac{R}{a}\right). \tag{2.8}$$

The only difference is that we have to put *R*, i.e. the distance between the current and the point where we want to calculate the field, instead of *r*.

$$R = \sqrt{a^2 + r^2 - 2ar\cos(\vartheta - \varphi)}\ . \tag{2.9}$$

If we consider the case in which $r < a$, it is useful to write the logarithm of R/a in this way:

$$\ln\left(\frac{R}{a}\right) = \frac{1}{2}\ln\left[1 - \left(\frac{r}{a}\right)\exp(i(\vartheta - \varphi))\right] + \frac{1}{2}\ln\left[1 - \left(\frac{r}{a}\right)\exp(-i(\vartheta - \varphi))\right]. \tag{2.10}$$

Using the Taylor expansion of the logarithm:

$$\ln(1 - \xi) = -\xi - \frac{1}{2}\xi^2 - \frac{1}{3}\xi^3 - \dots\dots\dots - \frac{1}{n}\xi^n - \dots\dots \tag{2.11}$$

we obtain the vector potential and the field components:

$$A_z(r,\vartheta) = \frac{\mu_0 I}{2\pi}\sum_{n=1}^{\infty}\frac{1}{n}\left(\frac{r}{a}\right)^n \cos[n(\vartheta - \varphi)]; \tag{2.12}$$

$$B_{\vartheta}(r,\vartheta) = -\frac{\partial A_z}{\partial r} = -\frac{\mu_0 I}{2\pi a}\sum_{n=1}^{\infty}\left(\frac{r}{a}\right)^{n-1}\cos[n(\vartheta-\varphi)];$$

$$B_{r\vartheta}(r,\vartheta) = \frac{1}{r}\frac{\partial A_z}{\partial \vartheta} = -\frac{\mu_0 I}{2\pi a}\sum_{n=1}^{\infty}\left(\frac{r}{a}\right)^{n-1}\sin[n(\vartheta-\varphi)];$$

$$B_z(r,\vartheta) = 0\ .$$

A single current line along the *z* axe creates a magnetic field with any order of multipoles. For our use, we are interested in specific configurations of the field, which can be obtained working on current distribution on the plane.

If we consider a series of different cables, arranged along the *z* axe to cover a cylinder surface of radius *a*, we can calculate the field generated by this configuration. It is possible to obtain a pure multipolar field of order $n = m$, only if the current distribution, given as a function of the azimuthal angle φ, has this behavior:

$$I(\varphi) = I_0\cos(m\varphi). \tag{2.13}$$

This statement is easily verifiable by computing the integration of the vector potential in 2π:

$$A_z(r,\vartheta) = \frac{\mu_0 I_0}{2\pi}\sum_{n=1}^{\infty}\frac{1}{n}\left(\frac{r}{a}\right)^{n}\int_0^{2\pi}\cos(m\varphi)\cos[n(\vartheta-\varphi)]d\varphi\ . \tag{2.14}$$

The integral is null for m = n, so the series remain with only one term:

$$A_z(r,\vartheta) = \frac{\mu_0 I_0}{2}\frac{1}{m}\left(\frac{r}{a}\right)^{m}\cos(m\vartheta); \tag{2.15}$$

$$B_{\vartheta}(r,\vartheta) = -\frac{\mu_0 I_0}{2}\left(\frac{r}{a}\right)^{m-1}\cos(m\vartheta);$$

$$B_r(r,\vartheta) = -\frac{\mu_0 I_0}{2a}\left(\frac{r}{a}\right)^{m-1}\sin(m\vartheta)\,.$$

These fields are the so-called “normal multipole” fields. If we rotate the current distribution by an angle of *π / 2m*, we obtain a sin ($m\varphi$) distribution, leading to “skew multipole” fields. A skew dipole, for instance, has a horizontal field. Skew components are usually quite undesirable inside circular accelerators.

It is not a trivial problem to create a current distribution with perfect cos($m\varphi$) dependence using superconducting cables with constant cross section. The field quality obtained with different configurations is expressed in terms of the coefficient of the Fourier series expansion of the field in the aperture, at a reference radius. For this purpose, we can describe the field with the so-called general multipole expansion. Reference radius has usually to be in the same order as the maximum deviation of the protons from the center axis of the magnet (ususally 2/3 of the magnet aperture). For LHC dipoles, a reference radius r_0 = 17 mm is considered. Multipolar expansion can be written as follow [10]:

$$B_\vartheta(r,\vartheta) = B_{ref}\sum_{n=1}^{\infty}\left(\frac{r}{r_0}\right)^{n-1}\left[b_n\cos(n\vartheta) + a_n\sin(n\vartheta)\right]; \tag{2.16}$$

$$B_r(r,\vartheta) = B_{ref}\sum_{n=1}^{\infty}\left(\frac{r}{r_0}\right)^{n-1}\left[-a_n\cos(n\vartheta) + b_n\sin(n\vartheta)\right].$$

Expressing the magnetic field as a complex function, it is possible to write:

$$B_y + iB_x = B_{ref}\sum_{n=1}^{\infty}(b_n + ia_n)\left(\frac{x+iy}{r_0}\right)^{n-1}; \tag{2.17}$$

where:

r_0 = reference radius;

B_{ref} = magnitude of the main field at reference radius. ($B_{ref} = B_1$, for dipoles, for instance);

b_n = normal multipole coefficients;

a_n = skew multipole coefficients.

Having chosen B_{ref} as explained above, the main coefficient remains normalized to unit: $b_1 = 1$ for dipoles, $b_2 = 1$ for quadrupoles, etc. Remaining components, for a good magnet, should be very small, typically $|a_n|,|b_n| \cong 10^{-4}$. The measure unit for multipolar coefficients is the unit of multipole ($1\cdot10^{-4}$).

From the multipolar expansion equation, we can see how the conductor distribution for LHC has been chosen. Let us consider a symmetry distribution of cables, where, for each current +I, situated at an angle φ, other three currents are present: +I at $-\varphi$, -I at $\pi-\varphi$, -I at $\pi+\varphi$ (see Figure 2.12). The potential vector results:

$$A_z(r,\vartheta)=\frac{2\mu_0 I_0}{\pi}\sum_{n=1,3,5...}\frac{1}{n}\left(\frac{r}{a}\right)^n\cos(n\varphi)\cos(n\vartheta). \qquad (2.18)$$

Therefore, from a symmetry distribution, we can only obtain normal multipoles and not skew ones. Moreover, only odd values of n appear.

The current distribution corresponding to a perfect dipole, as already shown, is $I(\varphi) = I_0\cos\varphi$. We can think to create this distribution using a single cylinder, of small thickness, inside which conductors receive a different current corresponding to their position with respect to the mid-plane. Having cables with uniform current supply, it is easier to simulate a $\cos\varphi$ distribution using a different density of cables inside the cylinder. The simplest current shell arrangement with dipole symmetry is shown in Figure 2.12. We assume a constant current density J and compute the vector potential inside the coil:

$$A_z(r,\vartheta)=\frac{2\mu_0 J}{\pi}\sum_{n=1,3,5,....}\frac{1}{n}\int_{a_1}^{a_2}\left(\frac{r}{a}\right)^n a\,da\int_0^{\phi_1}\cos(n\varphi)\cos(n\vartheta), \qquad (2.19)$$

ϕ_1 = limiting angle of the current shell;

a_1, a_2 = internal and external radii of the current shell.

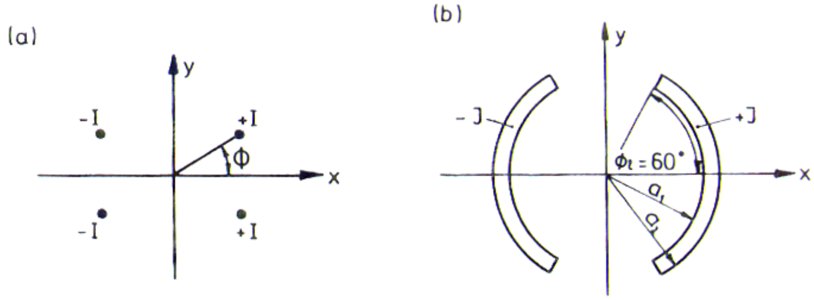

Figure 2.12: Dipolar symmetry current lines and shells.

For a thin current shell, with a thickness $\Delta a=a_2-a_1<<a=1/2(a_1+a_2)$, the expression reduces to:

$$A_z(r,\vartheta)=\frac{2\mu_0 J}{\pi}a\Delta a\sum_{n=1,3,5,....}\frac{1}{n^2}\left(\frac{r}{a}\right)^n\sin(n\phi_l)\cos(n\theta). \tag{2.20}$$

The magnitude of the field of multipole order n is:

$$B_n=\frac{2\mu_0 J}{\pi}\Delta a\frac{1}{n}\left(\frac{r}{a}\right)^{n-1}\left|\sin(n\phi_l)\right|. \tag{2.21}$$

Choosing a limiting angle $\phi_l = 60^0$ the sextupole term n =3 vanishes. Then the first non-vanishing higher multipole is the decapole n= 5. For typical coil dimensions the ratio:

$$\frac{B_5}{B_1}=\frac{1}{5}\left(\frac{r}{a}\right)^4\frac{\left|\sin 300^0\right|}{\sin 60^0}, \tag{2.22}$$

is a few percent, two orders of magnitude larger than its tolerance. A single-layer current shell arrangement with constant current density is therefore too rough an approximation for a dipole coil. With two current shells, the sextupole and the decapole can both be made to vanish by choosing a limiting angle of about 72^0 in the inner and 36^0 in the outer layer.

It is possible, once the base geometry has been decided, to optimize the conductors distribution and the blocks positions to avoid certain components in the magnetic field or to permit some of them. In LHC dipoles, six blocks geometry has been chosen. Each block having two degrees of freedom in the plane, there are twelve parameters to be used to optimize the field. Copper wedges and blocks are disposed in such a way as to create a dipole field but also some other components are allowed. The multipolar components, intentionally present in the nominal field or not, describe the perturbations with respect to the ideal dipole field. They are due to different reasons:

- design geometry, optimized to contrast the effects of persistent currents;
- eddy currents;
- iron yoke influence;
- fabrication tolerances of the different components and tooling used to assemble them.

While the first are multipoles which respect at least the symmetry given by the horizontal mid-plane, the second and third may present components which do not respect any symmetry and are responsible for any skew components appearing in the apertures. All components may be systematic, although in a series fabrication every effort will be made to keep them as small as possible. Systematic multipole errors represent the average of the measured field components in different magnets. Random errors indeed, represent the standard deviations of the measured multipoles [11].

Table 2.1: Expected multipole performance at injection and at 8.4 T (in units of 10^{-4} relative field error at 17 mm)

N	At injection, 0.58 T				At nominal operation, 8.4 T			
	Mean		Random		Mean		Random	
	Norm	skew	Norm	skew	Norm	Skew	norm	skew
	b_n	a_n	$\sigma [b_n]$	$\sigma [a_n]$	b_n	a_n	$\sigma [b_n]$	$\sigma [a_n]$
2	±0.85	±0.5	0.7	1.7	1.7±0.9	±0.5	0.7	1.7
3	-10.4±0.9	±0.9	1.4	0.4	1.4±0.9	±0.9	1.7	0.4
4	±0.98	±0.98	0.5	0.5	±0.98	±0.98	0.5	0.5
5	1.5±0.4	±4.2	0.7	0.3	0.5±0.4	±4.2	0.4	0.3
6	-0.06	0.0	0.3	0.1	-0.07	0.0	0.085	0.15
7	-0.6	0.0	0.2	0.2	0.1	0.0	0.2	0.07
8	0	0.0	0.2	0.2	0	0.0	0.04	0.08
9	0.4	0.0	0.2	0.3	-0.07	0.0	0.07	0.07
10	0	0.0	0.2	0.2	0	0.0	0.0	0.0
11	1.6	0.0	0.2	0.2	1.6	0.0	0.0	0.0

In the next chapters, we will show how to evaluate random errors on multipolar components using a finite element model of the magnet, which is able to compute deformations and stresses in correspondence of different load and geometry cases. The spread to be expected for all random multipoles is given in Table 2.1. Here, multipole components are obtained by scaling the random errors of HERA, RHIC and LHC prototypes measured magnets to the dimensions of the LHC main dipoles. Multipoles are expressed in relative field errors in 10^{-4} at the reference radius R_{ref} = 17 mm, both at magnet excitation corresponding to beam injection and at nominal operation. In the following paragraph, we will analyze the different reasons for multipole component errors with respect to the nominal field.

Persistent magnetization currents are the source of severe field distortions at low excitation of a superconducting accelerator magnet [10]. There are different types of induced currents:

- eddy currents between different strands inside a single cable;
- coupling currents between different filaments inside a strand;
- magnetization currents inside individual filaments.

The latter are the only ones that can be considered truly persistent currents, whilst eddy and coupling currents tend to decay exponentially with a time constant below a second. Persistent currents, indeed, can be considered long living. They are currents induced in the superconducting filaments by field variations and, contrary to normal conductors where they are rapidly reduced by resistance, they circulate as long as the superconductor is kept below its critical temperature.

Persistent current errors affect all field multipole components allowed by the symmetry configuration of the magnet, including the fundamental one. Their importance decreases with excitation, but they are particularly disturbing at low field level and especially at injection. At injection, the multipoles created by persistent currents in the filaments (mainly sextupole, b_3, and decapole, b_5) are very large. When raising the current these perturbations die away. They also depend on the previous powering of the magnet and vary with time and, therefore, require a careful study of the magnetic excitation cycle. Persistent currents are proportional to the effective diameter of the superconducting filaments, so they have to be as thin as possible, to comply with economy and quality of production.

Eddy currents indeed occur during field sweep in multistrand conductors, both inside the strands, mainly due to coupling between filaments, and between the strands. They distort the magnetic field, and their effects depend on the geometrical and electrical characteristic of strands and cables (matrix and inter-strand resistance, cable aspect ratio, distribution of superconducting filaments).

Another source of errors in the magnetic field components is due to the effect of iron yoke magnetization. Its influence can be analyzed using the method of image currents, provided the iron is not saturated and the permeability μ is uniform.

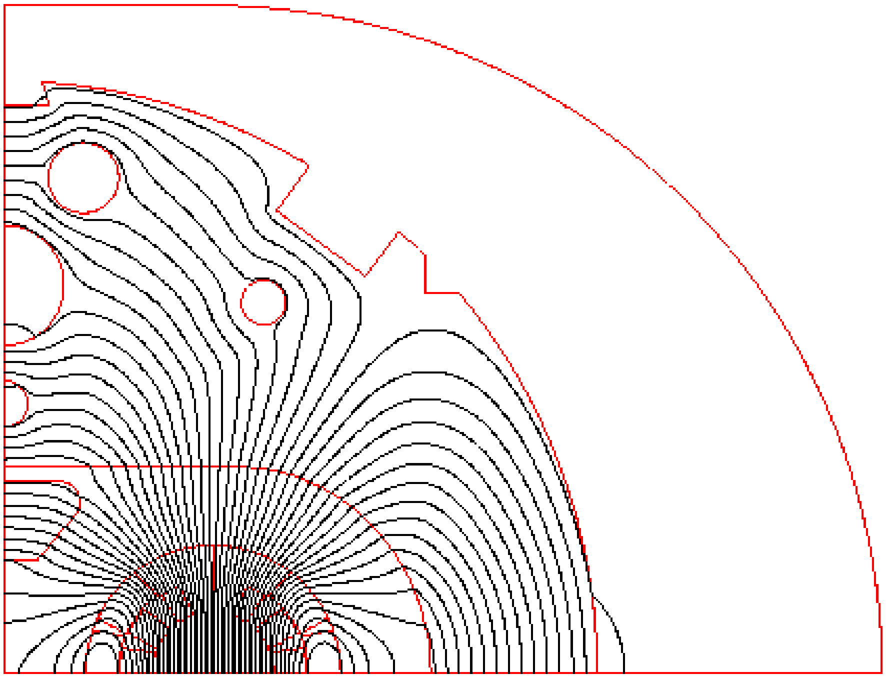

Figure 2.13: Magnetic flux as design.

Indeed, in the LHC cold dipoles, iron saturates in a significant way in its center part. Therefore, the permeability dependence on position leads to the necessity of finite element codes to compute the field pattern. With iron saturation, the dependence of dipole field B_1 on current I is no longer linear. During the energy ramp, multipoles caused by iron yoke saturation will appear. These consist of sextupole and decapole components, but also of quadrupole, octupole, and higher-order components induced by the two-in-one geometry. The yoke magnetic design was aimed at keeping these multipoles and especially their variation over the whole range of excitation, to a minimum, while reaching at the same time the highest possible dipole field. Figure 2.13 shows the flux plot as computed for the coil collar yoke assembly [3].

Other sources of errors in the multipolar field are due to geometry production errors on the magnet components and assembly procedures. As already seen, field quality strictly depends on conductor positioning inside the magnet. The induced errors can be computed at design stage from the known possible or imposed manufacturing tolerances. Sensitivity matrices can be computed for displacements of single conductors or for conductor blocks, to obtain a relation between geometry variations and field components. This theme will be discussed in the next chapter.

3 MECHANICAL AND MAGNETIC MODELS OF THE DIPOLE

3.1 The mechanical finite element model

To build up a model of the cross section of the dipole, the finite element code ANSYS® has been used. Finite element methods are approximation to continuum problems, such that [12]:

- continuum is divided into a finite number of parts (elements), whose behavior can be described by a finite number of material properties;
- the solution of the complete system is given as an assembly of its elements, and follows exactly the same rules as those applicable to standard discrete problems.

We used a two dimensional model where all the areas have been modeled with the same kind of structural solid elements, i.e. PLANE42. We used them with the plane strain option, since dipoles are much longer than their transversal dimension. Thickness parameter has been used to permit the modeling of the two layers of collars (see 3.1.2). Each area is given the appropriate material properties, i.e. Young modulus, Poisson modulus and thermal expansion coefficient, for both room and low temperature. Contact between surfaces of different components has been described using CONTACT52 elements, which will be discussed in the next paragraphs. Contact elements also have the function of loading the model, using their interference values (see 3.1.4).

Only one quarter of the dipole is modeled, because the cross section has two perpendicular axes of symmetry. Boundary conditions have been put on symmetry axes. The model is used to compute the field of deformations and the stresses at warm and at cold temperature, i.e., 293 K and 1.9 K.

3.1.1 The coils

The coils are modeled taking into account their two principal components, i.e., superconducting cables and copper wedges. Different areas describe conductor blocks and copper spacers. Due to the geometry and to the different components of the blocks (see section 1.2), their elastic modulus is not constant, and varies according to the load. The most influencing factors that causes such a behavior are the presence of kapton (polyimide film) layers around conductors and the presence of empty spaces between conductors and insulation. Kapton in fact, can be compressed until a certain load reacting in a soft manner. Once reached certain compression, layers become denser, previously empty spaces are filled with kapton, and surfaces do not slide as before one over the other. At this moment, the elastic modulus of the coils become higher and the reacting force increases respect to the imposed displacements. Such a nonlinear behavior has to be taken into account to correctly evaluate the conductor displacements and their position at working conditions. In particular, it is crucial to determine the correct elasticity curve in the tangential direction, where the main stresses are applied.

A specific tool is used to measure coils elastic behavior (see chapter 3.2), from which a set of stress/displacement data is obtained. As explained in Appendix A [13], a stress/strain curve is fitted from those data and inserted into the model to describe coil material behavior at room temperature. Also at cold (1.9 K), a curve describes coils answer to solicitation, but in this case its slope is smaller than the previous one. Physical explanation of such assumption, which seems not in agreement with the measured properties, will be given in Chapter 4. In theory in fact, once cooled down, the coil becomes more rigid and the Young modulus should be higher than the room temperature one.

The coefficient of thermal expansion has also to be involved in the material properties. For both the inner and the outer layers, the same value has been assumed, i.e.:

$$\int_{1.9}^{293} \alpha(T)dT = 8 \pm 1 \cdot 10^{-3} \tag{3.1}$$

Being the thermal gradient of about 300 K, the average thermal expansion coefficient is $\alpha = 2.7 \cdot 10^{-5}$. This value is interpreted by the FEM code ANSYS® as mean value [14].

Poisson's ratio is set at a value of 0.2, because of the influence of kapton, which leads to some decrease respect to the 0.3 value typical for metallic materials.

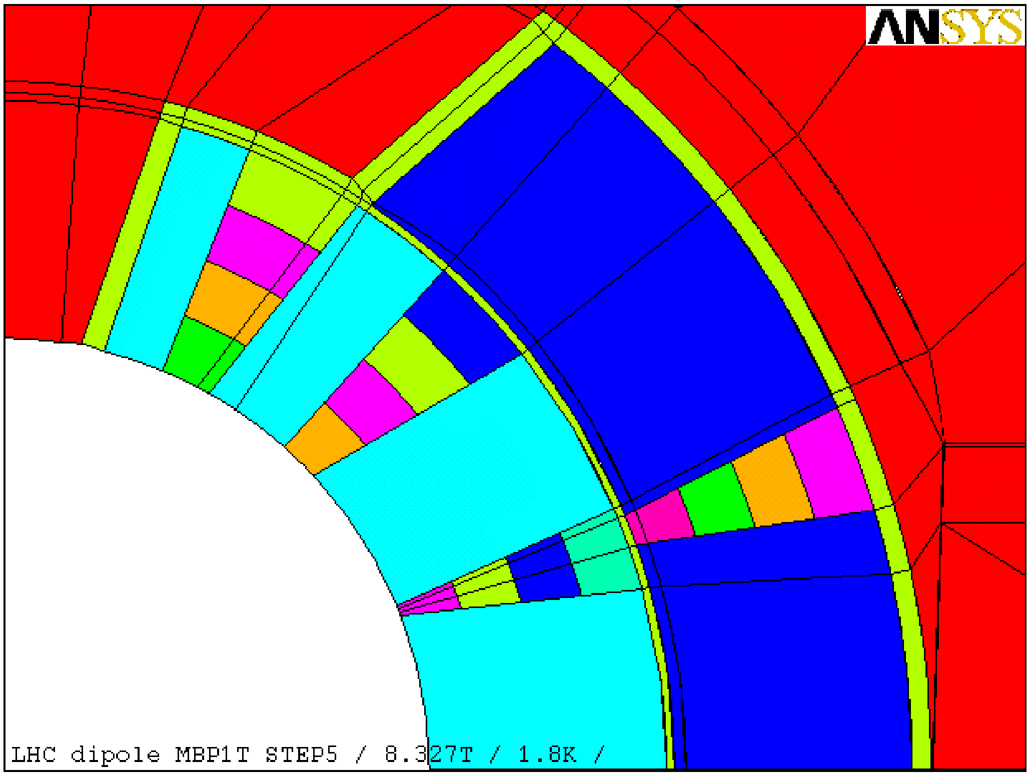

Figure 3.1: Coils areas modeled in ANSYS®.

Copper wedges areas are divided into four pieces along the radial direction (see Figure 3.1), to count also the insulation layer contribution in the elastic moduli computation. Each zone of the copper is given a material property depending on the proportion between copper and insulation thickness. The resulting Young modulus is given by equation (3.2).

$$E_{eq} = \frac{E_1 E_2 l_{tot}}{E_1 l_2 + E_2 l_1}. \tag{3.2}$$

In (3.2):

E_1 = 136000 MPa (293 K), 150000 MPa (1.9 K), copper elastic modulus;

E_2 = 3000 MPa (293 K), 4500 MPa (1.9 K), insulation layer elastic modulus;

l_1, l_2 = copper and insulation thickness;

$l_{tot} = l_1+l_2$.

Poisson's ratio is set to $\nu = 0.3$, as usual for metallic materials. Average thermal expansion coefficient is taken from literature and is given a value of $\overline{\alpha} = 1.1\cdot10^{-5}$.

Coils dimensions are determined taking care of the conditions for which nominal geometry has been defined. Nominal lengths in azimuthal direction in fact, are given for a coil having a tangential prestress of about 40 MPa at 1.9 K. To recover this conditions, longer coils are defined in the model at room temperature and in absence of solicitations. These values are optimized using a code called ANSIA [15], which automatically evaluates the deformation and the coil length increase at room temperature needed to recover the nominal length at cold.

3.1.2 The collars

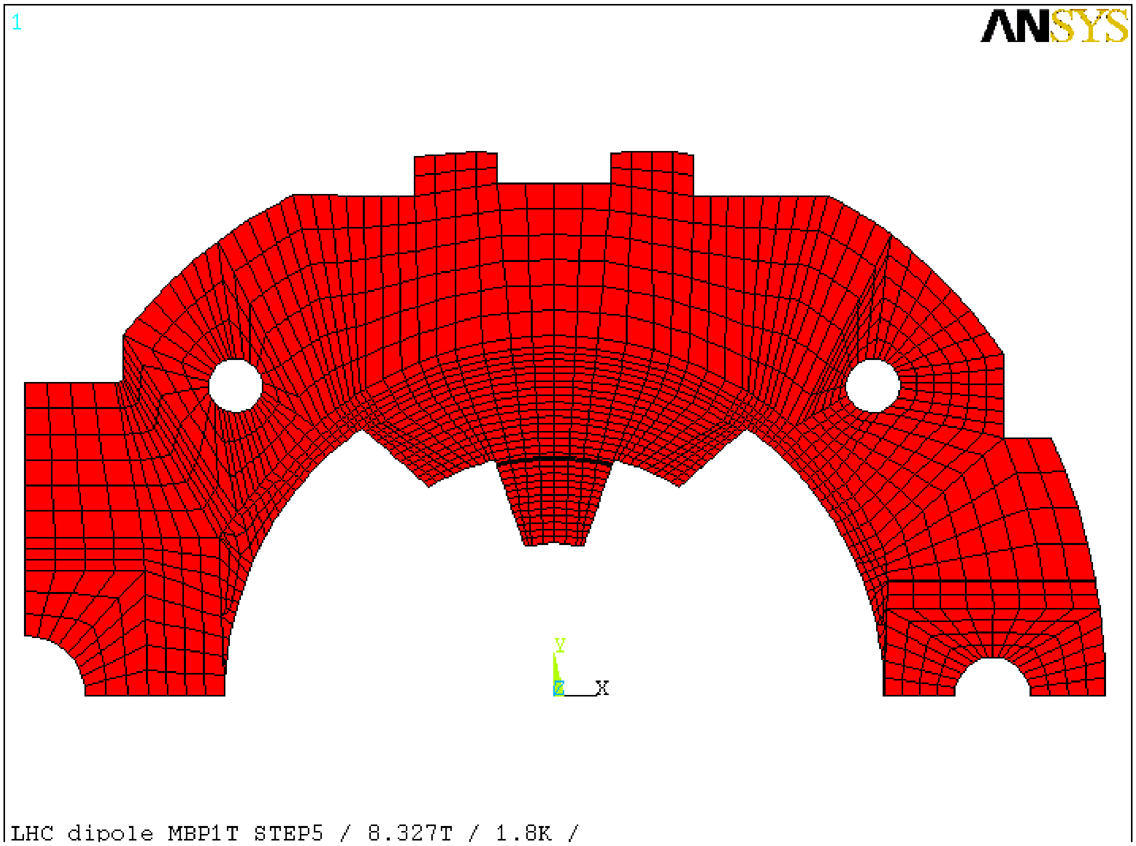

Figure 3.2: One layer model of the collar in ANSYS®.

The collars are built up with austenitic steel sheets. Collars layers are superposed one to the other to create packs, assembled using little pins. Each layer is composed of two different parts, the so-called "long-collar" and the "short-collar". The "long-collar" contains the holes where to put the bars used to lock the collars around the coils. The short one has indeed a pure filling function. Different layers of collars are assembled putting alternatively the long collars on the upper part and on the lower part of the magnet. In our model, we have two layers of collars, the first one composed by two pieces, whose contact is simulated using contact elements, the second one composed only by one piece (see Figure 3.2).

Each collar layer is given a thickness of 0.5 mm, while all the other components of the dipole are modeled with PLANE42 elements 1 mm thick. In this way, the assembling effects of the two collars of the same layer and the presence of different layers are taken into account.

The presence of different sheets creates a particular stress distribution in the collars, which, in correspondence of the mid-plane, tend to be opened by the compressed coils. In Figure 3.3, long and short collar interaction in correspondence of the mid-plane is shown. Boundary conditions to give the two layers the same displacements in *x* direction and the opposite in *y* direction in correspondence of the mid-plane are imposed.

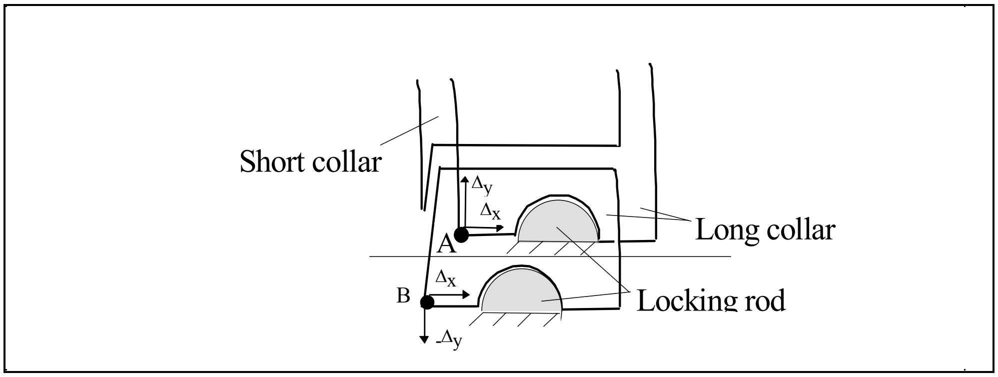

Figure 3.3: Long and short collars interaction on the mid-plane.

Austenitic steel properties are reported in Table 3.1. They are given without specification of direction, since material is isotropic.

Table 3.1: Collars material properties.

Austenitic steel	1.9 K	293 K
Young modulus E	210000 MPa	190000 MPa
Expansion coefficient α	$0.9 \cdot 10^{-5}$	
Poisson's modulus ν	0.3	

3.1.3 The yoke and the cylinder

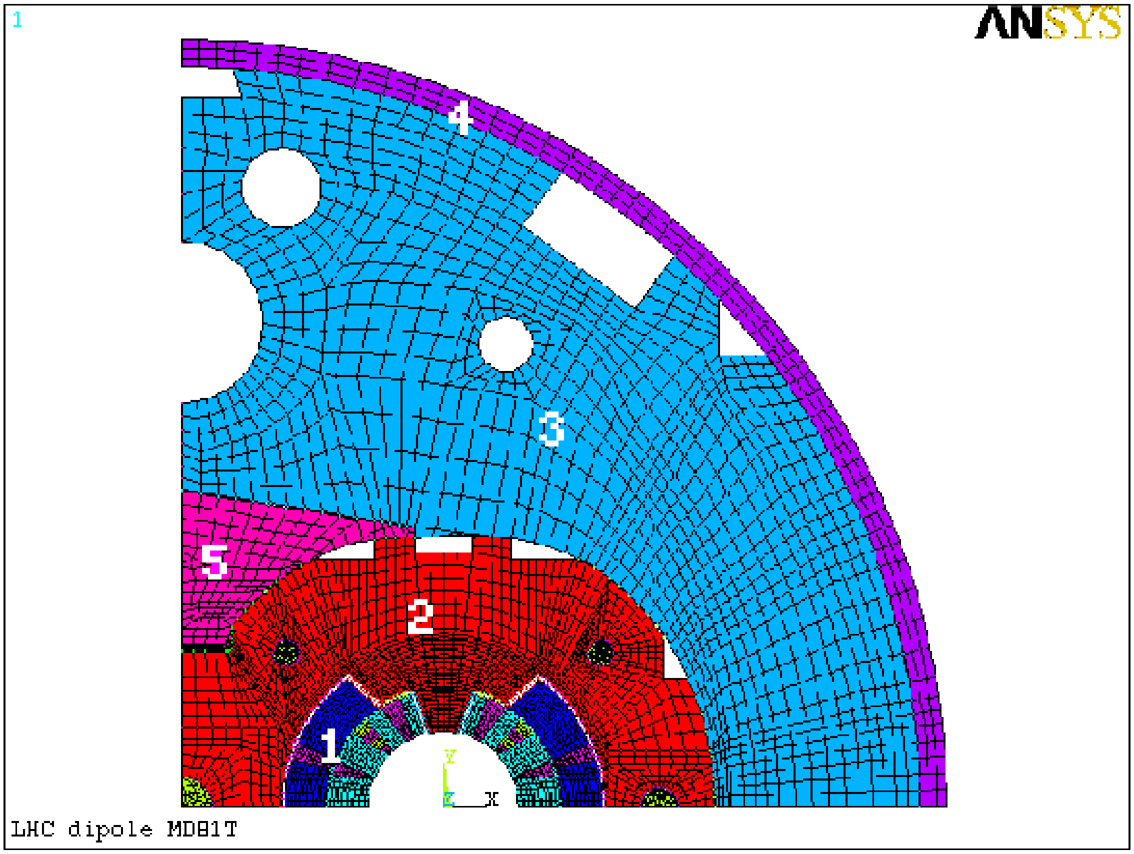

Figure 3.4: Assembled model of the LHC dipole.

On the outer part of collars, the iron yoke (3) is positioned and blocked by the cylinder (4) soldered around it. Between them, in correspondence of the vertical axe of symmetry, an iron insert (5) is put. In Table 3.2 and in Table 3.3, yoke and cylinder material properties input in the model are listed.

Table 3.2: Iron yoke material properties.

Iron yoke	1.9 K	293 K
Young modulus E	225000 MPa	210000 MPa
Expansion coefficient α	$0.7 \cdot 10^{-5}$	
Poisson's modulus ν	0.3	

Table 3.3: Shrinking cylinder material properties.

Shrinking cylinder	1.9 K	293 K
Young modulus E	209000 MPa	195000 MPa
Expansion coefficient α	$1.0 \cdot 10^{-5}$	
Poisson's modulus ν	0.3	

The insert has essentially a filling function and its presence helps the assembling. Iron insert material properties are listed in Table 3.4.

Table 3.4: Iron insert material properties.

Shrinking cylinder	1.9 K	293 K
Young modulus E	209000 MPa	195000 MPa
Expansion coefficient α	$1.0 \cdot 10^{-5}$	
Poisson's modulus ν	0.3	

3.1.4 The contact interfaces

Interfaces between all the surfaces of the magnet components have been modeled using contact elements. In ANSYS® there are different types of contact elements, used to simulate different situations (i.e. contact between points, between points and surfaces, between surfaces) [14]. In our model of the dipole, the problem of interaction between components of the magnet, which are not glued but only assembled with pins, has been solved using Contac52 ANSYS® elements.

These elements represent two surfaces, which may maintain or break physical contact and may slide relative to each other. This element is capable of supporting only compression in the direction normal to the surfaces and shear (Coulomb friction) in the tangential direction. Everywhere in our model, we choose not to model any friction, assuming that its effect is negligible. The zone where it could have more influence, i.e., between coils and collars, some kapton layers are positioned to permit gliding.

Contac elements assume as surfaces in contact the two ideal planes perpendicular to their direction (see Figure 3.5, *IJ* direction), so one must build them up exactly perpendicular to the real surfaces in contact.

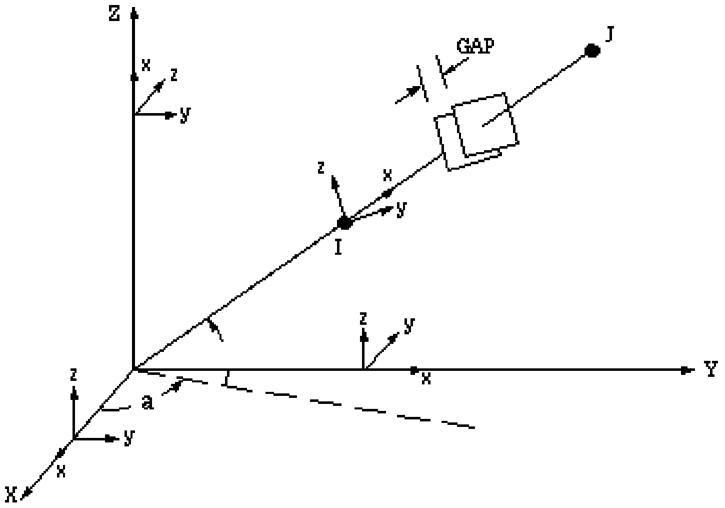

Figure 3.5: Contac52 reaction directions.

Even a few degrees error in the construction gives a mistake in the transmission of forces between the two materials that may be relevant (see Appendix B). These elements react as springs in their normal direction, the answer to solicitation being directly proportional to their deformation and to their normal stiffness. We need to separate two different cases in order to define the value of this stiffness. This is because in the model of the magnet we simulate both direct and indirect contact between two surfaces, i.e., the contact between two surfaces without any interlayer or with the presence of some filling material not explicitly modeled.

In the first case contact elements have to transfer forces between the two surfaces and must avoid penetration between bodies, possible in FEM code, but not in reality. For this reason, we establish a small value ($d_{max} \approx 10^{-4}$ mm) for maximum accepted compenetration. This entity can be written as a function of the pressure applied (P), the area on which each element insists (A) and the contact element stiffness (K).

$$d = \frac{P \cdot A}{K} \tag{3.3}$$

Imposing $d < d_{max}$, we obtain an estimate for the minimum normal stiffness (K_{min}) useful to contain the compenetration under the maximum allowed:

$$K = \frac{P \cdot A}{d_{\max}}, \tag{3.4}$$

where A is the area on which the element insist. Usually, we will obtain values of K with an order of magnitude between 10^4 and 10^8 [MPa·m].

In the second case, there is not a direct contact between two sliding surfaces, but contact elements are used to simulate the presence of thin layers of different materials, not explicitly modeled, i.e. shims, ground insulation, quench heaters. This situation happens in all the zones between coils and collars and in the zone between the inner and the outer coil. In this case, we have to take in account filling materials deformation under loading. One has to define an equivalent Young modulus (E_{eq}) for all the materials simulated, treating them as series springs. If there are three materials to be considered, the modulus becomes:

$$E_{eq} = \frac{E_1E_2 + E_1E_3 + E_2E_3}{E_1E_2E_3} \tag{3.5}$$

and we calculate K as follow:

$$K = \frac{AE_{eq}}{h}, \tag{3.6}$$

where:

A = area on which every contact element insist;

h = length of the contact element;

E_{eq} = Young elastic equivalent modulus

Since it is always necessary to know on which area the contact elements transfer the pressure to evaluate K_n, a uniform distribution has been given to nodes along the lines. In this way, the only two contact elements that insist on different size areas are the first and the last of each set of contact. For these two elements, the area is one half respect to the others and also K is set equal to the half of the one calculated for this zone of contact.

Let us now show the values of the contact element stiffness calculated for our model. Macros have been computed to automatically calculate these values, on the base of the two equations (3.4) and (3.6). They are given in input respectively the maximum permitted compenetration and the estimated pressure in the first case, the equivalent Young modulus in the second one. The latter is given both for warm temperature and for cold temperature. Macros create contact elements automatically in zone defined by four keypoints, two belonging to one surface and the others to the facing one.

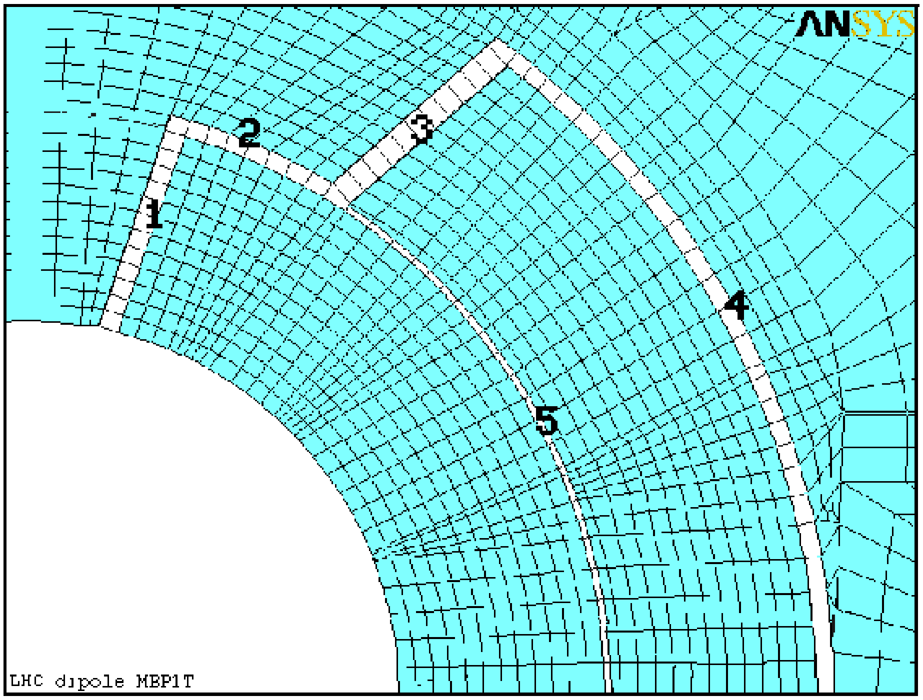

Figure 3.6: Different zones of contact between coils and collars.

Interface between coils and collars has been modeled using contact elements to simulate the behavior of the insulation layers, the quench heaters and the shims, which are not explicitly modeled. Contact elements length corresponds to their total thickness in each zone in study. All the zones interested by this kind of contact element are shown in Figure 3.6. In Table 3.5, filling materials with their thickness and their Young moduli are listed for each zone.

Table 3.5: Filling materials thickness and Young moduli.

Zone	**Filling material**	**Thickness [mm]**	**E at 1.9 K [MPa]**	**E at 293 K [MPa]**
1	Shim retainer - Austenitic Steel	0.6	215000	190000
	Shim - EP GC 3#	0.4	20000	20000
	Insulation sheets - Polyimide	0.5	4500	3000
	Interlayer	0.5	7500	6000
2	Inter layer	0.5	7500	6000
	Insulation sheets - Polyimide	0.5	4500	3000
	Shim retainer - Austenitic steel	0.3	215000	190000
3	Coil protection sheet - Austenitic steel	0.3	215000	190000
	Shim - EP GC 3#	1.0	20000	20000
	Insulation sheets - Polyimide	1.2	4500	3000
4	Coil protection sheet - Austenitic steel	0.6	214000	190000
	Insulation sheets - Polyimide	0.7	4500	3000
5	Interlayer	0.5	7500	6000

In Table 3.6, the calculated equivalent Young moduli corresponding to each sandwich are listed, for both room and cold temperature.

Table 3.6: Equivalent Young moduli for contact zones between coils and collars.

N	Zone of contact	E_{eq} at 1.9 K [MPa]	E_{eq} at 293 K [MPa]
1	inner coil /collar - radial	10000	7300
2	inner coil /collar - azimuthal	7300	5200
3	outer coil/collar - radial	7900	5500
4	outer coil /collar - azimuthal	8200	5500
5	inner coil/outer coil	9500	6000

The "initial status" of the elements has also to be considered. In fact, contact elements can be initially preloaded in the normal direction or they can be given a gap specification. Test made on simple models had shown that giving an interference to contact elements means simulating a different dimension of one of the two surfaces in contact, so that the spring is already loaded at the beginning of the calculation (see Appendix B).

Regarding interference properties, in zones 1 and 3 of Figure 3.6, these values represent shims thickness and can be varied to obtain certain prestress in the coils or to simulate different shapes of the collar, as it will be shown in chapter 4. All in the other zones, interference is set to 0. This will provide a simple gliding behavior between the two surfaces in contact.

In the other zones of interface, i.e., between collars, between collars and rods, between cylinder and yoke, etc., contact elements only have to simulate interaction between the two surfaces, avoiding any friction and compenetration.

3.2 The magnetic model

To evaluate the magnetic field components corresponding to the configurations studied, the magnetostatic code ROXIE [3] has been used. ROXIE (Routine for the Optimization of magnet X-section, Inverse field calculation and coil End design) is a code developed at CERN to optimize LHC coils and yokes design. The program consists of procedures for the geometrical optimization of the coil cross section, for magnetic field calculation and inverse problem solving.

Block position is calculated with respect to the initial status of the coil, described by the number of conductors per block, the type of conductor used, the inner and the outer radii of the coil and the angular position of blocks itself. Each conductor is given a certain current density value, different from zone to zone of the same conductor, depending on the number of strands in that zone. Once determined the nominal geometry, it is possible to assign component rotational or translational displacements. This option has not been used in our computations, since component deformations have been evaluated thorough the ANSYS® calculations.

To transfer ANSYS® deformations into ROXIE [3], it is necessary to extrapolate from ANSYS® output the single cable displacements, which can be given as ROXIE input. ROXIE indeed, is able to give single conductors a certain displacements, as shown in Figure 3.7, where conductor number 27 has been shifted by 2 mm to the center of the aperture.

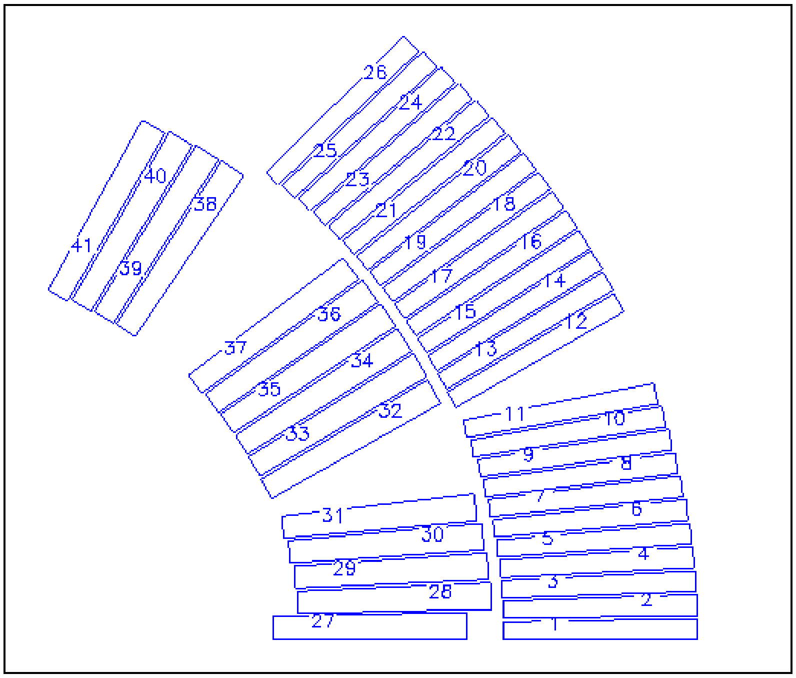

Figure 3.7: Example of deformed geometry in ROXIE.

The finite element code used to evaluate deformation presents some differences on data treatment. First of all, ANSYS® undeformed coil is longer than nominal one, as explained in 3.1.1, moreover, the ANSYS® output results are not given with respect to each cable, but for each node of the model mesh. For this reason, it is necessary to calculate a correspondence between node displacements and cable displacements. Looking at the undeformed geometry in ANSYS®, in each block modeled, nodes corresponding to conductor position have been listed. They correspond to each conductor medium thickness, as shown in Figure 3.8. For each of these nodes, displacements under loading have been evaluated. In some cases, if nodes were not exactly corresponding to midpoints, a linear interpolation has been done between the two nearest nodes.

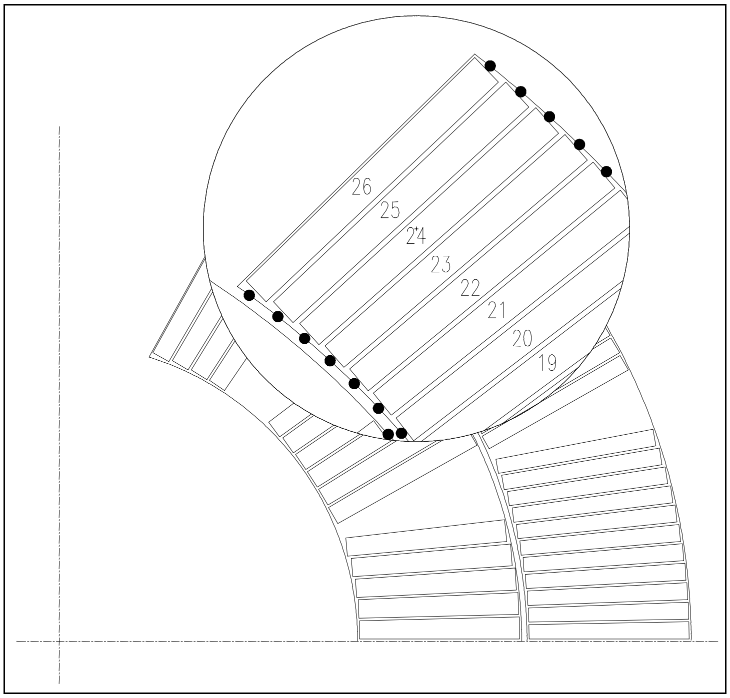

Figure 3.8: Reference points for data transfer between ANSYS® and ROXIE.

Once evaluated displacements with respect to ANSYS® unloaded geometry, they have to be reduced to ROXIE nominal geometry. For this purpose, final positions of these points is evaluated and displacements inserted in ROXIE correspond to the difference between this geometry and the ROXIE nominal one.

4 MECHANICAL PROPERTIES MEASUREMENTS

4.1 Capacitive force transducers

Capacitive force transducers have been developed at CERN to measure the stress inside magnets, both at room and at cold temperature [16]. Their behavior is based on the well known relation (4.1):

$$C = \frac{S\varepsilon}{\delta}. \tag{4.1}$$

which gives the value of the capacitance C for a simple electrostatic transducer, constituted of two electrodes of area S. Between the electrodes, made by two plane sheets, a dielectric material with δ thickness and ε electric permittivity is inserted.

When an external pressure is there applied, if the elastic modulus of the dielectric is much smaller than the modulus of the electrodes, the capacitance changes with respect to this relation:

$$C = \frac{S\varepsilon}{\delta\left(1 - \frac{\sigma}{E}\right)}, \tag{4.2}$$

where σ is the applied stress and E is the dielectric Young modulus. Factors that may influence Eq. (4.2) are the mechanical properties of the dielectric and its boundary conditions. Deformations of the dielectric in orthogonal direction with respect to the load application, due to Poisson's moduli value, can be avoided by applying an hydrostatic stress. This condition is obtained by gluing the layers of the gauge one to the other. In this way, electrodes work not only with electrical purpose, but also as containment structure for the dielectric.

The gauge consists of a sandwich of stainless steel foils interleaved with polyimide films glued together (see Figure 4.1). Stainless steel 316LN has been chosen for the electrodes for two reasons: gauges have to support, without plastic deformation, high pressures and they have to work inside magnets without interfering with the magnetic field. For this purpose, non-magnetic stainless steel is required. Moreover, to better support high pressures, layers used for building gages are usually pre-plastified under a load of about 200 MPa.

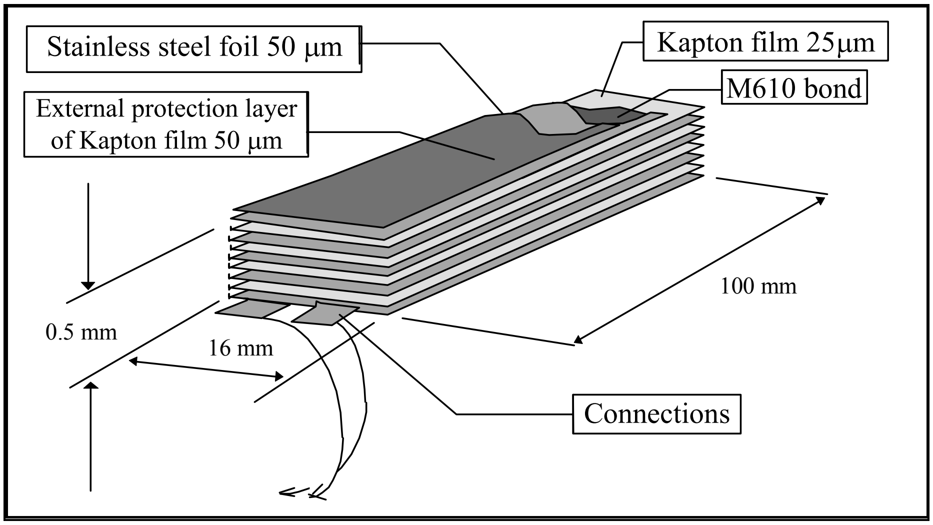

Figure 4.1: Capacitive force transducer.

The dielectric is chosen on the base of its elastic modulus and its electrical permittivity, from which gauge sensitivity directly depends. For magnet measurement gauges, kapton tapes were chosen as dielectric material. To glue the whole device, a special high-performance epoxy resin is used (Micro-Measurements®, M610). Its best properties are the good elongation capacity and the possibility of operating in a temperature range between 1.9 K and 430 K.

Gauges are fabricated in two steps: first components are prepared and cut. Then, they are superposed one to the other. After assembling, the sandwich of components is cured in a mould at 140^0 C during 2 hours. After curing, the dielectric layers, kept a little bit wider than electrodes to facilitate manufacturing, are cut precisely to electrodes dimension. Once fabricated, the gauge needs to be pre-cycled at a pressure 20% higher than the operating one, during a certain number of thermal cycles in liquid nitrogen.

Before use, gauges have to be calibrated. They are given a loading curve up to about 100 MPa and in the meantime, capacitance is measured. The output curves pressure/ capacitance show a small non-linearity at the very beginning of the load and some hysteresis during load-releasing cycles. These effect are in general small, and even with a linear approximation the error is of about 5% over a range of pressure up to 200 MPa.

Fringe capacitance of the wires and the connections must be taken in account while measuring. For gauges working at 77 K, the zero of the calibration curve results shifted of a about 800 pF compared to the zero at 300 K. This is the Apparent Capacitance value (AC). It is due essentially to the change of permittivity of the polyimide at cold temperature and to the thermal contraction after cooling. Sensitivity of the transducers is reduced of the 30% because of this effect when gauges are cooled.

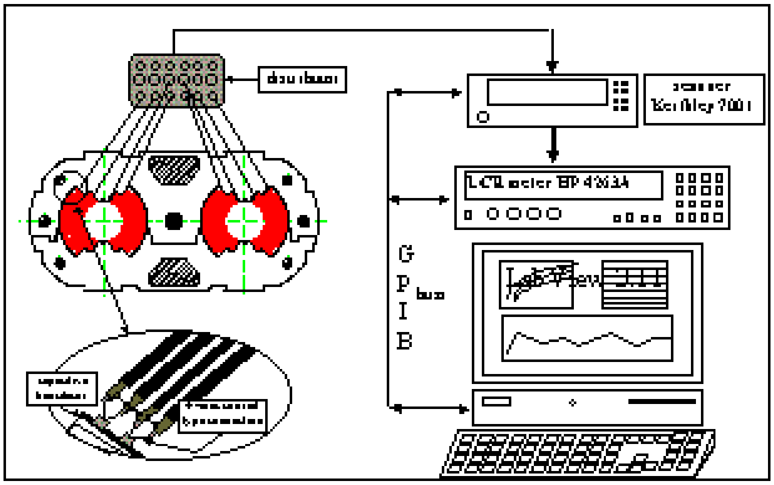

Figure 4.2: Schematic layout of the data acquisition system.

Usually it is necessary to acquire data from several capacitive probes at the same time. For this purpose, a data acquisition system with multichannel, driven by a PC, was developed for a series of magnet tests at CERN. A schematic structure of the system is shown in Figure 4.2. Through the GPIB interface, a program written in LabView® activates one channel each time in scan mode. Data are stored into the PC. After each scan, the data is transformed into pressure in a table format, according to the individual calibrations of the various transducers connected to the system.

4.2 Coils elasticity curve

Experimental data relative to the coil elasticity curve have been worked out in the CERN Short Dipoles laboratory through a mechanical test where the coils are compressed at room temperature (293 K). The coils are put inside a press, made up of two rigid blocks of steel, the upper one moved by an hydraulic system, the lower one fixed to a basement. A rigid mould dimensioned as coils nominal shape (see Figure 4.3) is positioned on the lower block.

Between the mould and the section of the coil that is tested, a thin layer of kapton is inserted, to permit better slide of the two surfaces and to avoid a non-uniform stress distribution. On the mobile block, in correspondence of the press mid-plane, displacement sensors are soldered, whilst, in correspondence of the zone where coils will be in contact with the upper block, capacitive force transducers, described in 4.1, used to measure pressure are glued.

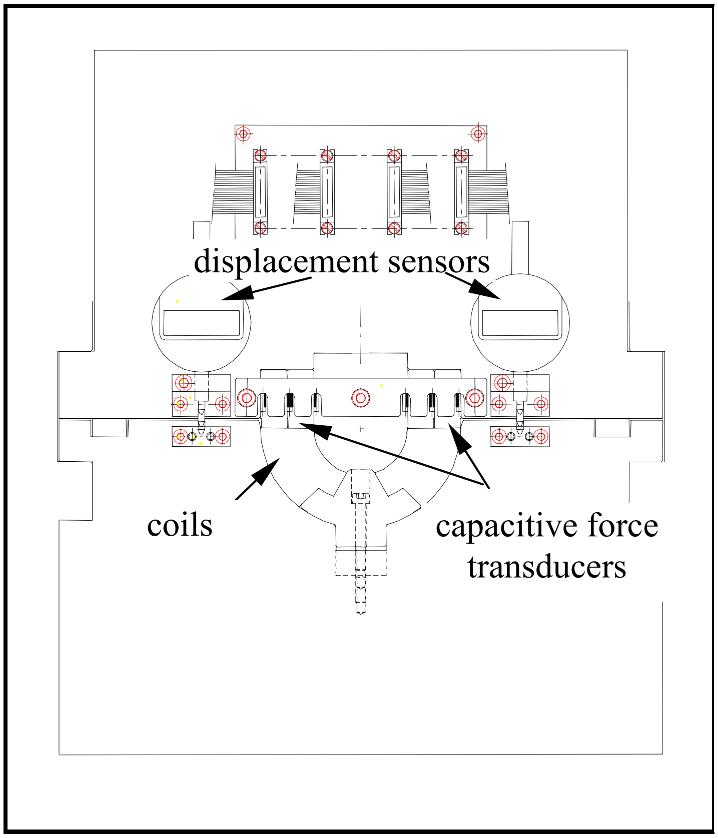

Figure 4.3: Coils elastic modulus measuring press.

Coils are positioned, only one for each measurement, inside the mould. During the test, the upper block displacement, assumed equal to the coil azimuthal contraction, is measured simultaneously to the pressure data acquisition, in steps of load determined by manual feed on the hydraulic system. Gauges indeed, give pressure values interpolated along the coils compressed section.

A series of measurements has been taken both on the inner and on the outer coil separately. During each measure, a loading/unloading cycle has been applied whose maximum value has been increased of 20 MPa from one cycle to the sequent one. The first compression cycle runs from zero to about 40 MPa, the last runs from zero to about 100 MPa. In this way, all the coil range of solicitation is covered by our tests. Each load case is evaluated twice.

Resulting data come out in the form of a table and of a plot, containing the pressure applied and the correspondent displacements measured both for loading and unloading steps. The experimental data examined in our computations are shown in Figure 4.4, Figure 4.5, Figure 4.6 and in Figure 4.7, for each one of the two cases measured for the same maximum load.

All data corresponding to a cycle have been fitted using two polynomial curves of the second order, one for the loading data and one for the unloading ones. Fitting curves are different for loading and unloading because of the hysteresis presented by coil answer to solicitation. Curves are built up starting from data corresponding to a pressure of more than 5 MPa. This is because, under this value of solicitation, we are not interested in the deformation field. Fitting curves are drawn on Figure 4.4, Figure 4.5, Figure 4.6 and in Figure 4.7: continuous lines correspond to loading and dotted lines correspond to unloading, while dots correspond to acquisition points.

The zero of the graphics depends on the calibration of the acquisition system. Coils dimension in azimuthal direction is not well defined in absence of loading, because of the different components which are not glued but only compressed and heated into a press before assembling (see 2.3.1.3). For this reason, the acquisition system has been calibrated such in a way that measured displacements are null when coils are loaded with a pressure of approximately 50 MPa.

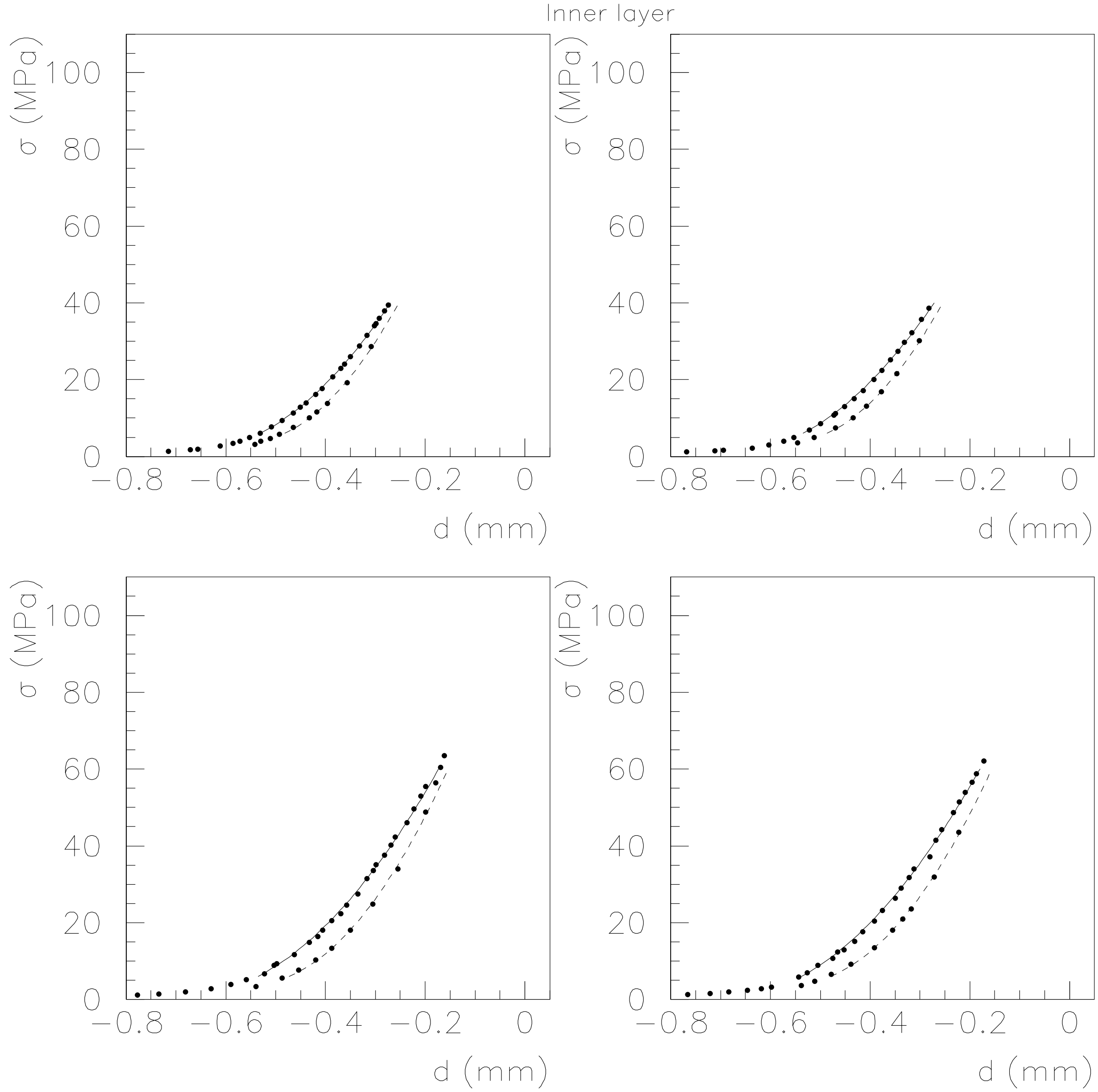

Figure 4.4: Inner coil experimental data, sets for two loading cycles with maximum value of 40 MPa and other two with a maximum value of 60 MPa. Continuous line: loading fitted curve. Dotted line: unloading fitted curve.

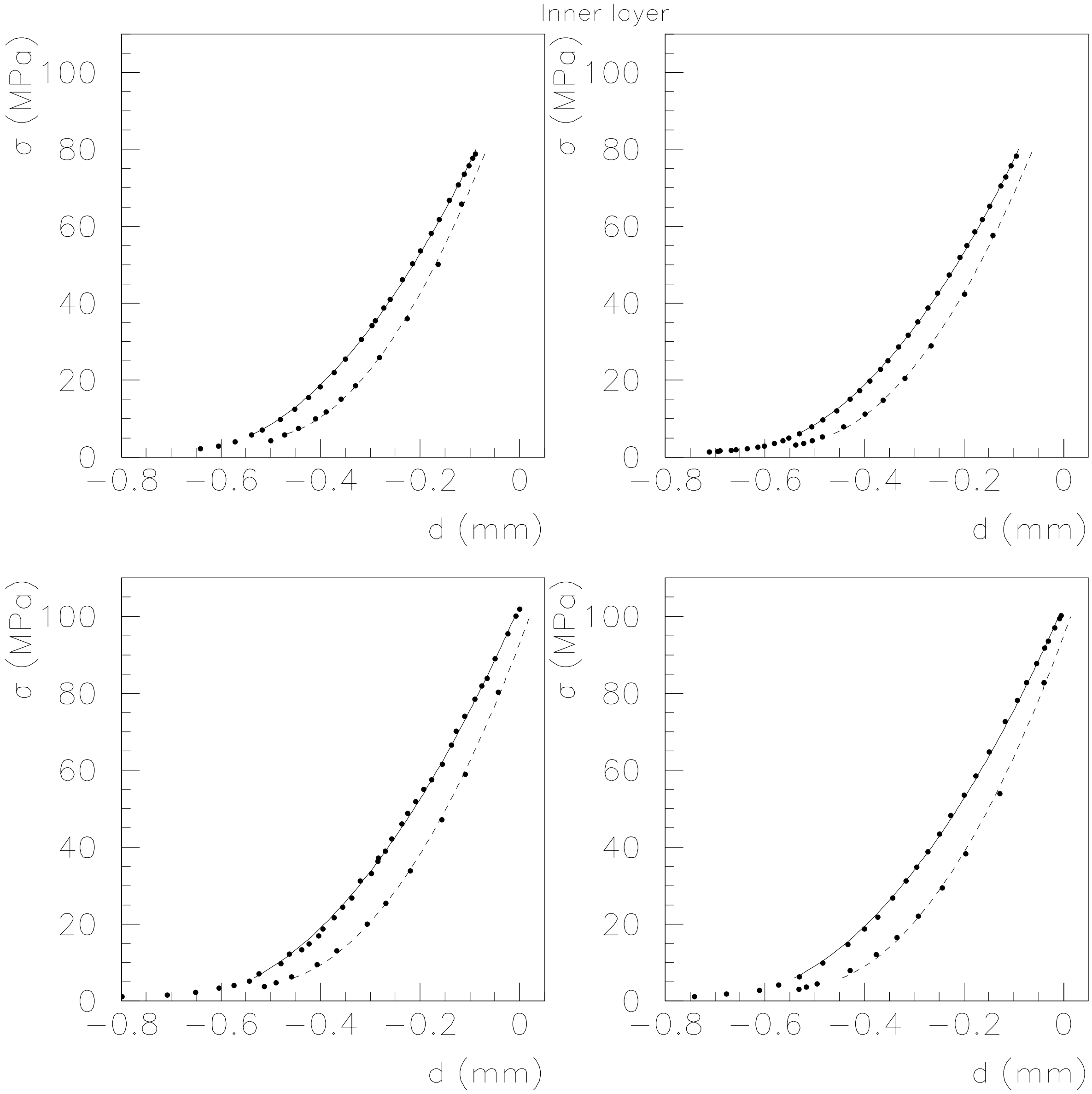

Figure 4.5: Inner coil experimental data, sets for two loading cycles with maximum value of 80 MPa and two other with a maximum value of 100 MPa. Continuous lines: loading fitted curve. Dotted lines: unloading fitted curves.

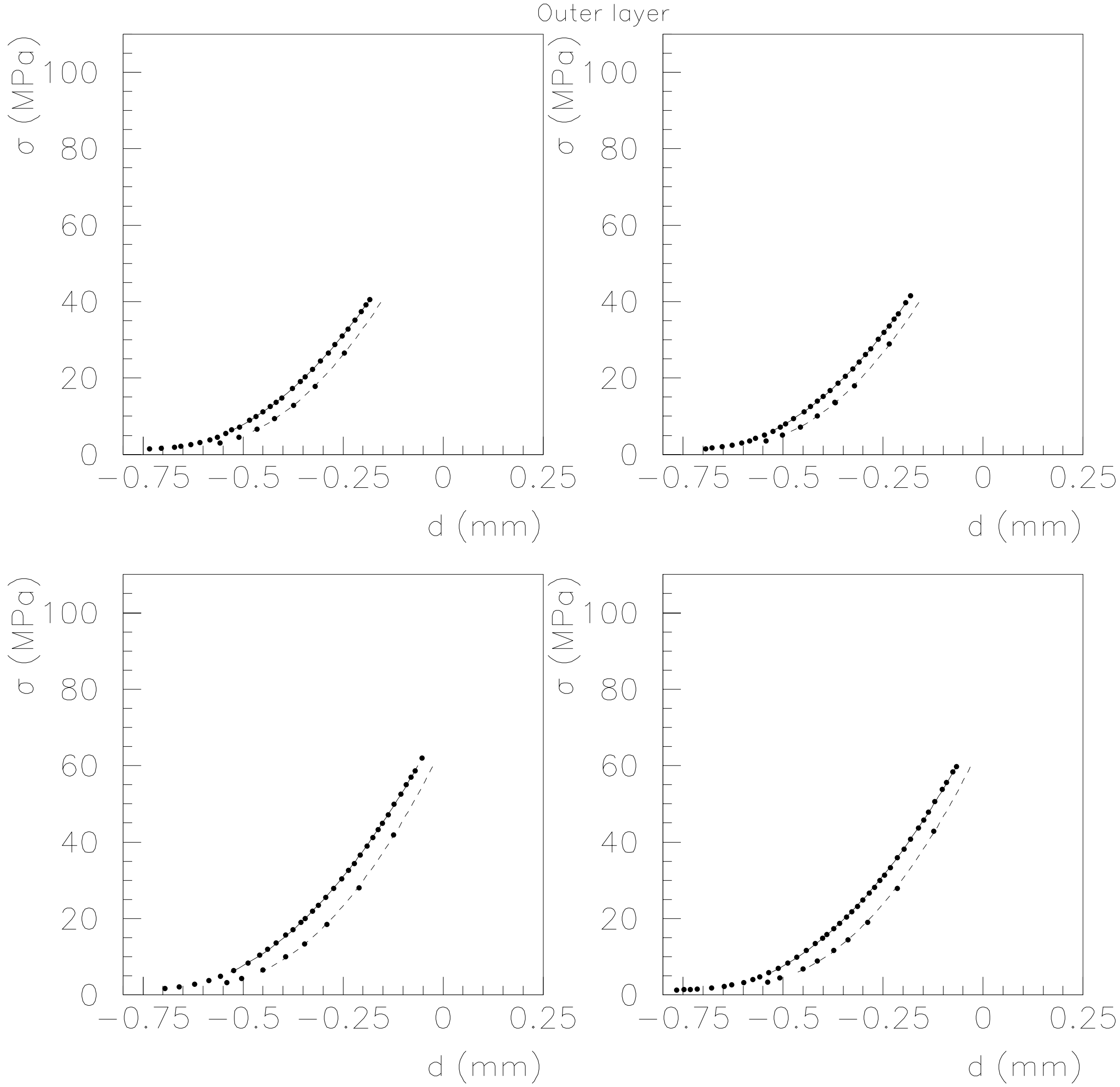

Figure 4.6: Outer coil experimental data, sets for two loading cycles with maximum value of 40 MPa and two other with a maximum value of 60 MPa. Continuous line: loading fitted curve. Dotted line: unloading fitted curve.

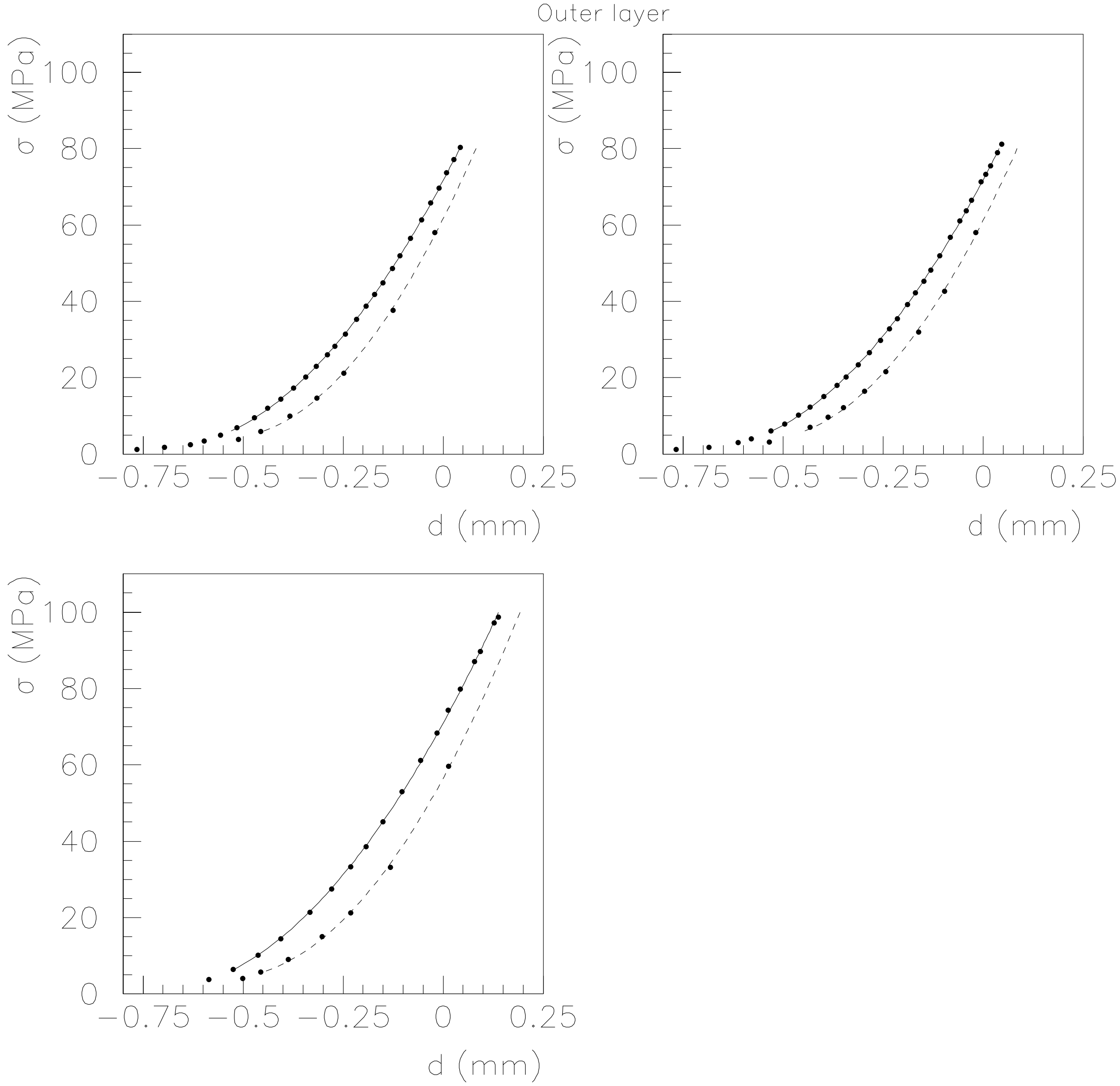

Figure 4.7: Outer coil experimental data, sets for two loading cycles with maximum value of 80 MPa and two other with a maximum value of 100 MPa. Continuous line: loading fitted curve. Dotted line: unloading fitted curve.

To extrapolate the Young modulus of the coil blocks from these data, it is necessary to postprocess them. First, a best fit is made on both the ascending and the descending curves, using a second order polynomial curve. In this way, for each loading cycle, two fitting curves are obtained. In Table 4.1and in Table 4.2, their coefficients are given, analyzing two different experimental cases for each load. They represent the following relation:

$$\sigma = ad^2 + bd + c \tag{4.3}$$

where σ is the applied stress and d is the measured displacement.

We carry out the fit on displacements instead of on the deformation: in fact, in order to evaluate the deformation one has to fix a coil length d_0 at 0 MPa, that is difficult to evaluate with great precision. One can overcome this problem according with the following strategy. We assume that copper wedges are uncompressible and the deformation reads:

$$\varepsilon = \frac{d - d_0}{l} \tag{4.4}$$

where d is the measured displacement and, d_0 is the unknown coil length at 0 MPa and l is the blocks azimuthal nominal length.

One can work out the relation between the elastic modulus and the applied stress. The Young modulus is defined as the first derivative of the $\sigma(\varepsilon)$ curve and can be calculated either directly as the slope of the straight line connecting two consecutive measurements, or evaluating the first derivative of the fitting curve. We use this second method, which leads to more precise numerical estimates.

Taking into account the expression of the deformation as a function of the displacement (4.4), the derivative of the (4.3) results:

$$E = \frac{d\sigma}{d\varepsilon} = \frac{\partial \sigma}{\partial d} \cdot \frac{\partial d}{\partial \varepsilon} = l \cdot (2ad + b) = 2adl + bl \,. \tag{4.5}$$

In order to derive a relation between E and σ, we write the deformation as a function of the elastic modulus $d = \frac{E}{2al} - \frac{b}{2a}$ and then substituting this expression inside (4.3), we obtain:

$$\sigma = a\left(\frac{E}{2al}-\frac{b}{2a}\right)^2 + b\left(\frac{E}{2al}-\frac{b}{2a}\right)+c \tag{4.6 a}$$

$$\sigma = \frac{E^2}{4al^2}+\frac{b^2}{4a}-\frac{Eb}{2al}+\frac{Eb}{2al}-\frac{b^2}{2a}+c \tag{4.6 b}$$

$$\sigma = \frac{E^2}{4al^2}-\frac{b^2}{4a}+c\,. \tag{4.6 c}$$

Therefore E as a function of σ reads:

$$E \;= \sqrt{4al^2\left(\sigma - c + \frac{b^2}{4a}\right)} = 2l\sqrt{a}\sqrt{\sigma + \left(\frac{b^2}{4a}-c\right)}\,. \tag{4.7}$$

As it is possible to see in Table 4.1 and in Table 4.2, (last columns), the quantity $\left(\frac{b^2}{4a}-c\right)$ has values representing a few per cent of the usual working values of σ (≈ 40÷80 MPa). Moreover, these values are not physical since they are negative. Therefore, it is reasonable to assume that E ($\sigma = 0$) = 0 and therefore $\left(\frac{b^2}{4a}-c\right)=0$:

$$E \;= 2l\sqrt{a}\sqrt{\sigma} \tag{4.8}$$

In this way, we obtain an estimate of the Young modulus without using the coil length d_0, which is very difficult to measure.

If in Eq.(4.8) we take into account the relation $\varepsilon = \sqrt{\frac{\sigma}{F}}$, we can write:

$$E = \frac{d\sigma}{d\varepsilon} = 2F\varepsilon = 2\sqrt{F\sigma} \tag{4.9}$$

Examining the data in Table 4.1 and in Table 4.2, it is interesting to notice that, while all loading curves can be perfectly superposed one to the other, unloading curves do not seem so correlated. Indeed, the correspondence also of these curves is shown. We can say that unloading curves result shifted of a certain amount if we increase the maximum load value in the cycle. This shift is probably due to a certain plastic deformation of the coil components and to an hysteresis behavior of the coils.

Table 4.1: Inner coil measurements interpolation curve coefficients.

INNER COIL								
Max load [MPa]	LOADING CURVE				UNLOADING CURVE			
	a $\left[\frac{MPa}{mm^2}\right]$	b $\left[\frac{MPa}{mm}\right]$	c [MPa]	$\frac{b^2}{4a}-c$ [MPa]	a $\left[\frac{MPa}{mm^2}\right]$	b $\left[\frac{MPa}{mm}\right]$	c [MPa]	$\frac{b^2}{4a}-c$ [MPa]
40	245	326	110	-2	377	426	124	-3
40	230	315	109	-1	374	424	124	-4
60	225	309	107	-1	360	395	112	-4
60	224	312	109	0	350	390	112	-4
80	225	305	105	-1	361	378	104	-5
80	231	311	106	-2	321	353	101	-4
100	210	293	103	0	324	339	93	-5
100	209	292	103	-1	332	348	95	-4

Analyzing the data relative to the coefficient *a*, we can evaluate the averages and their errors for both inner and outer layers and for loading and unloading curves. The analysis of Figure 4.4 to Figure 4.7, and of the data in Table 4.1and Table 4.2, shows that the curves for different maximal loading are approximately the same.

The plots of the obtained experimental σ (E_t) curves are given in Figure 4.8 and Figure 4.9. Therefore we assume that there are only two curves $\sigma(\varepsilon)$, one for loading and one for unloading for each coil layer.

Table 4.2: Outer coil measurements interpolation curve coefficients

OUTER COIL								
Max load [MPa]	LOADING CURVE				UNLOADING CURVE			
	a	b	c	$\frac{b^2}{4a} - c$	a	b	c	$\frac{b^2}{4a} - c$
[MPa]	$\left[\frac{MPa}{mm^2}\right]$	$\left[\frac{MPa}{mm}\right]$	[MPa]	[MPa]	$\left[\frac{MPa}{mm^2}\right]$	$\left[\frac{MPa}{mm}\right]$	[MPa]	[MPa]
40	139	198	72	-2	175	216	69	-2
40	145	204	74	-1	178	220	71	-3
60	142	200	72	-2	184	214	65	-3
60	142	201	72	-1	186	216	66	-3
80	139	197	72	-1	190	209	62	-4
80	140	199	72	-1	184	206	61	-4
100	130	192	71	-1	239	228	60	-6

The data for the estimates of a and F are given in Table 4.3, where 2 sigmas are taken for the error (97.7 % of confidence level).

Table 4.3: Fitting curves coefficient a: average and sigma values.

	INNER COIL		OUTER COIL	
	Loading	Unloading	Loading	Unloading
a average [MPa/mm^2]	225	350	140	182
a sigma [MPa/mm^2]	11	20	4	5
F [MPa]	$2.3 \cdot 10^5$	$3.6 \cdot 10^5$	$2.6 \cdot 10^5$	$3.4 \cdot 10^5$

The analysis of Table 4.3 also shows that both inner and outer layers have approximately the same behavior, within the experimental errors. The elastic modulus varies from about 6500MPa to about 10500 MPa in the range of the coil solicitation (30÷80 MPa). One can also verify that the coils result harder during unloading. This is why, once certain compression is given, spaces between conductors are filled by kapton, which moreover stops gliding after some compression and add resistance to more deformations. In this case, even if the pressure is released, certain deformation remains and the elastic modulus results bigger than the correspondent one at the same value of stress but on the loading curve.

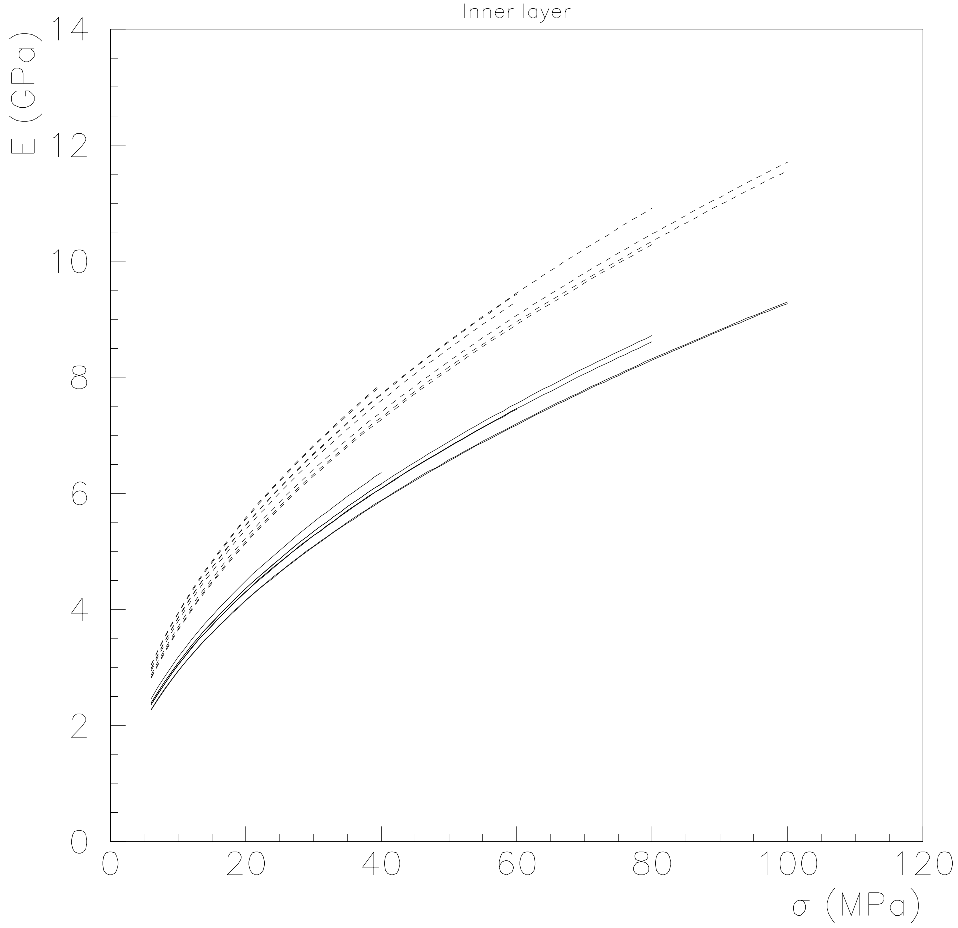

Figure 4.8: Inner coil experimental relations between *E* and *σ*.

If we connect all the experimental data with a line, the shape obtained is that one of a typical hysteresis cycle. It is not trivial to implement these experimental data and the so evaluated material properties inside the finite element model. A first approximation is made deciding to use the data relative to the unloading curve. This is because, in our model, we always start calculation from the dipole already assembled. What we study in fact, is the position of cables and the component stress after assembling the dipole or after cooling. Both in these cases, the coil stress decreases, for materials relaxing after compression and for the thermal contraction too in the cold case. A way of implementing the elastic curve inside the finite element model is shown in Appendix A [10].

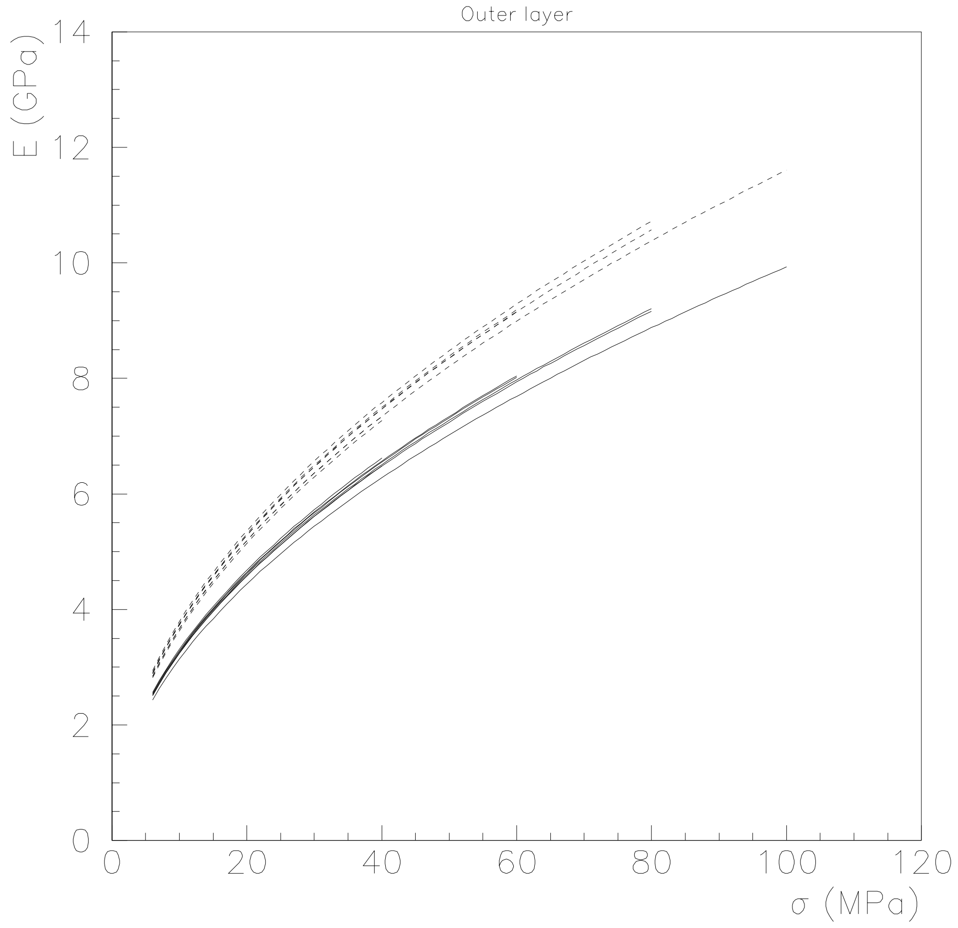

Figure 4.9: Outer coil experimental relations between *E* and *σ*.

4.3 Coils prestress at room and at cryogenic temperature

Coils stress measurements on short models of the LHC dipoles have been done at CERN by the Short Dipole Section of the LHC/MMS group [2].

Table 4.4: Prestress measurements on the coils

PRESTRESS MEASUREMENTS						
After collaring [MPa]		After yoking [MPa]		At cold 1.9K [MPa]		Magnet model
Inner	Outer	Inner	Outer	Inner	Outer	
100	122	109	133	42	60	v2 re-collared with SS collars
100	122	94	105	36	47	v4 without support from the yoke
86	104	92	110	38	48	Re-collared with mixed collars (Al+SS)
69	94	77	101	28	47	SS, 6-blocks
58	63	66	71	26	24	v2, , re-collared, with a less pre-stress
88	97	93	103	38	43	
88	97	93	103	33	38	v4 without axial support (no bullets)
58	74	66	80	23	30	SS, 6-blocks
58	69	64	76	27	35	Re-collared with 0.15-mm shims more
62	78	72	87	28	32	Re-assembled: all ferromagnetic yoke
54	73	62	80	26	30	V2, Re-collared on the bore tube
70	94	74	97	30	37	v1, only inner layer ULTEM spacers
50	57	62	68	21	23	SS, 6-blocks, ULTEM spacers
59	82	66	86	18	31	SS, 6-blocks, Apica

59	82	66	86	15	29	V1+ 50kN/bullet (instead 15kN before)

Capacitive force transducers described in 4.1 have been put inside the magnet, between collars and coils, in correspondence of the collars "noses". Measurements are taken both at room temperature after collaring and after yoking, and at cold. The data relative to several magnet models are given in Table 4.4.

Analyzing such measurements, it is possible to find a law that connects the prestress on the coils after assembling at room temperature with the ones at cold temperature.

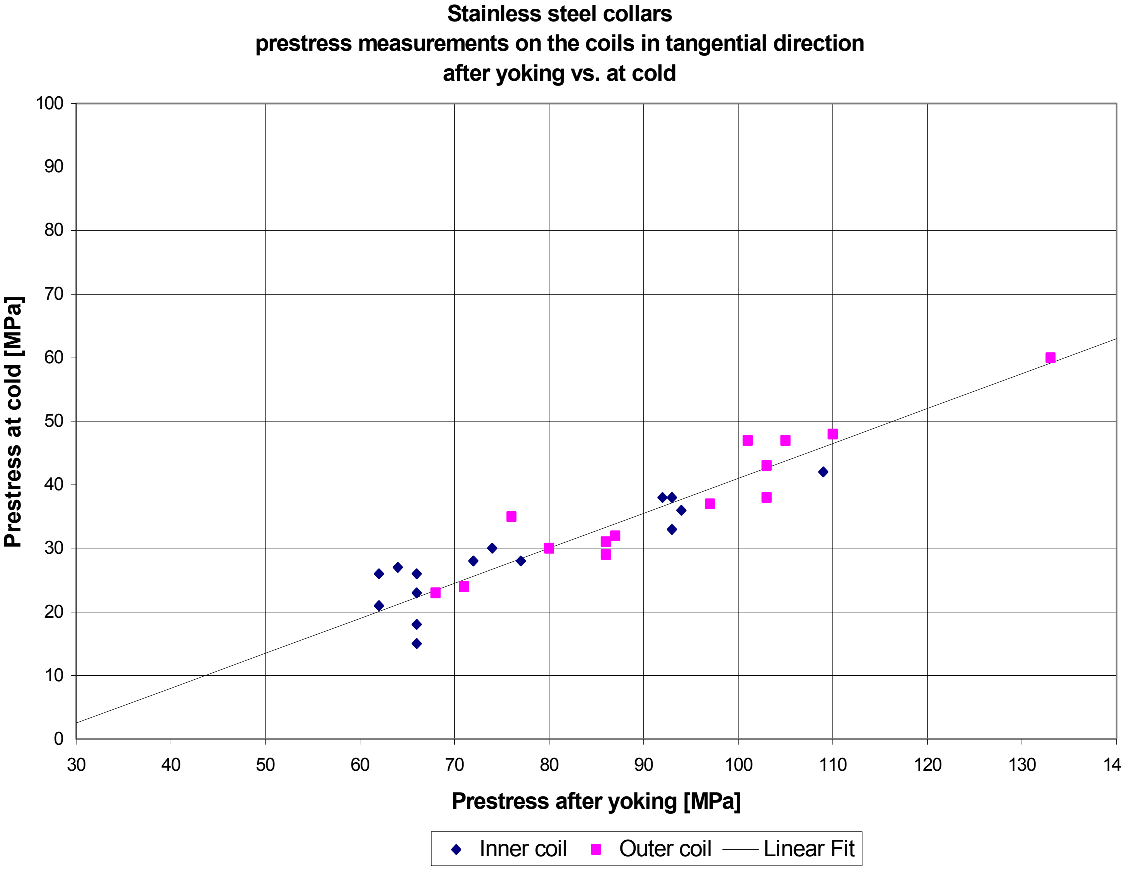

Figure 4.10: Inner and outer coil stresses after yoking and at cold: experimental data and linear interpolation.

Looking at Figure 4.10, we can notice that the relation between cold and warm measurements can be fitted with a linear curve:

$$\sigma_c = A(\sigma_w - B), \tag{4.10}$$

with:

A ≅ 0.55±0.09

B ≅ (20±10) MPa.

Both errors correspond to two sigmas.

The analysis of these data provides a way to check the agreement with the measured coefficient of thermal expansion of the coils. Moreover, it is possible to give estimates of coils Young modulus at cold temperature.

4.3.1 Check of the contraction coefficient of the coils

Experimental data show that a prestress of 0 MPa at cold temperature is reached for a coil compressed at warm temperature of around 20 MPa (see Eq. (4.10)). From these data, one can estimate the thermal contraction coefficient of the coils. In fact, in this load case the coil length compression at warm temperature must be equal to the thermal contraction.

$$l_{bw0}\alpha_b + l_{kw0}\alpha_k - l_{cw0}\alpha_c = \varepsilon_{bw} l_{bw0} + \varepsilon_{kw} l_{kw0}\,, \tag{4.11}$$

where:

l_{bw0} = blocks azimuthal length at warm temperature in absence of loading;

l_{kw0} = copper wedges azimuthal length at warm temperature in absence of loading;

l_{cw0} = collars azimuthal length at warm temperature in absence of loading;

α_b = coils thermal expansion coefficient;

$\alpha_k = 3.3\cdot10^{-3}$ = copper wedges thermal expansion coefficient, interpolated on 292 K;

$\alpha_c = 2.6\cdot10^{-3}$ = collars thermal expansion, interpolated on 292 K;

ε_{bw} = blocks deformation at warm temperature;

ε_{kw} = copper wedges deformation at warm temperature.

In Table 4.5, length values are reported for both the inner and the outer coil.

Table 4.5: Warm temperature components azimuthal lengths.

	l_{cw0} [mm]	l_{bw0} [mm]	l_{kw0} [mm]
Inner coil	46.2	32.1	14.1
Outer coil	48.7	43.5	5.2

One can derive α_b from (4.11):

$$\alpha_b = \frac{\alpha_c l_{cw0} - \alpha_k l_{kw0}}{l_{bw0}} + \varepsilon_{bw} + \varepsilon_{kw} \frac{l_{kw0}}{l_{bw0}} = \alpha_{b1} + \alpha_{b2} + \alpha_{b3} \tag{4.12}$$

We separately calculate the contributes of the different terms in (4.12). The first term (α_{b1}), depending on the thermal expansion coefficients, can be evaluated for both inner and outer coils using the constant values given above. It results:

α_{b1} (inner coil) = $2.3 \cdot 10^{-3}$;

α_{b1} (outer coil) = $2.5 \cdot 10^{-3}$.

To calculate the second (α_{b2}) and the third (α_{b3}) terms values, we first have to write blocks and copper wedges deformations as functions of their elastic modulus (E) and of the applied stress (σ = 20 ± 10 MPa). For copper wedges, whose Young modulus is a constant (100000 MPa), we obtain:

$$\varepsilon_{kw} = \frac{\sigma}{E_{kw}} = 0.2 \cdot 10^{-3} . \tag{4.13}$$

Contribution of the second term results:

α_{b2} (inner coil) = $0.09 \cdot 10^{-3}$;

α_{b2} (outer coil) = $0.02 \cdot 10^{-3}$.

For blocks, whose elastic modulus is given by Eq. (4.9), using the definition of elastic modulus, i.e., $E = \frac{\partial \sigma}{\partial \varepsilon}$, we can derive and substitute the Eq. (4.9) in it, obtaining:

$$\varepsilon_{bw} = \sqrt{\frac{\sigma}{F_{bw}}} \tag{4.14}$$

The experimental value of F_{bw} is $3.6 \cdot 10^{5}$.

From Eq. (4.14), we obtain the error estimate:

$$\frac{\Delta \varepsilon_{bw}}{\varepsilon_{bw}} = \frac{1}{2}\frac{\Delta \sigma}{\sigma} + \frac{\Delta l_{bw}}{l_{bw}} = 0.25 + 0.06 = 0.31 \tag{4.15}$$

where Δ are the errors on the measured values. Therefore, the third term contribution is:

$$\alpha_{b3} = \varepsilon_{\mathrm{bw}} = (7.5+2.3)\ 10^{-3} \tag{4.16}$$

Evaluation of α_b can be done neglecting the second term, two orders of magnitude smaller that the others. We get:

α_b (inner coil) = $(9.8 \pm 2.3) \cdot 10^{-3}$;

α_b (outer coil) = $(10 \pm 2.3) \cdot 10^{-3}$.

Neglecting the second term, it means that copper wedges deformation is negligible with respect to blocks one. It can be demonstrated that this is true for all the cases treated. For sake of simplicity, in the following, this term will be left out in the computation of the coil deformations.

4.3.2 Modeling the prestress loss from room to cryogenic temperature

We want now to calculate a theoretical relation between the stress/strain curve at cold and at warm temperature for the coils and to compare it with the experimental one. First, we assume that the relation between ε and σ is linear for all the components, conductors blocks included and that collar deformations are negligible both at warm and at cold temperature. This is because collar elastic modulus is much bigger than coils one. Therefore, we can write:

$$\varepsilon_{bw} = \frac{l_{bwo} - l_{bw}}{l_{bwo}} = \frac{\sigma_w}{E_{bw}}; \quad (4.17\ a)$$

$$\varepsilon_{bc} = \frac{l_{bco} - l_{bc}}{l_{bco}} = \frac{\sigma_c}{E_{bc}}; \quad (4.17\ b)$$

$$\varepsilon_{cw} = \frac{-l_{cwo} + l_{cw}}{l_{cwo}} = \frac{\sigma_w}{E_{cw}} \cong 0; \quad (4.17\ c)$$

$$\varepsilon_{cc} = \frac{-l_{cco} + l_{cc}}{l_{cco}} = \frac{\sigma_c}{E_{cc}} \cong 0; \quad (4.17\ d)$$

where relations *a* and *b* are written for the blocks, whilst relations *c* and *d* are written for the collar. From these expression, we obtain blocks and collar azimuthal lengths under compression once supposed known the relation between σ and E from experimental data.

$$l_{bw} = l_{bw0}\left(1 - \frac{\sigma_w}{E_{bw}}\right) \quad (4.18\ a)$$

$$l_{bc} = l_{bc0}\left(1 - \frac{\sigma_c}{E_{bc}}\right) \quad (4.18\ b)$$

$$l_{cw} = l_{cw0} \quad (4.18\ c)$$

$$l_{cc} = l_{cc0} \quad (4.18\ d)$$

Due to thermal expansion, the coils and collars unloaded lengths (at cold and at warm temperature) are given by:

$$l_{bw0} = l_{bc0}(1 + \alpha_b) \quad (4.19\ a)$$

$$l_{cw0} = l_{cc0}(1 + \alpha_c) \quad (4.19\ b)$$

Substituting the (4.19 *a*) into the (4.18 *a*) and the (4.19 *b*) into the (4.18 *c*), we obtain:

$$l_{bc0}(1 + \alpha_b)\left(1 - \frac{\sigma_w}{E_{bw}}\right) = l_{bw} \quad (4.20\ a)$$

$$l_{cc0}\left(1+\alpha_c\right)=l_{cw} \tag{4.20 b}$$

We neglect, as already explained, the influence of copper wedges, so that we can assume that blocks dimension under loading is equal to collar dimension, both at cold and at warm temperature.

$$l_{bc}=l_{cc} \tag{4.21 a}$$

$$l_{bw}=l_{cw} \tag{4.21 b}$$

From these relations, we can equate the first term of (4.20 *a*) with the first term of (4.20 *b*) and the second term of (4.18 *b*) with the second term of (4.18 *d*) obtaining:

$$l_{bco}\left(1+\alpha_b\right)\left(1-\frac{\sigma_w}{E_{bw}}\right)=l_{cco}\left(1+\alpha_c\right) \tag{4.22 a}$$

$$l_{bc0}\left(1-\frac{\sigma_c}{E_{bc}}\right)=l_{cc0} \tag{4.22 b}$$

Dividing Eq. (4.21 *b*) by Eq. (4.21 *a*), we get:

$$\left(1+\alpha_b\right)\left(1-\frac{\sigma_w}{E_{bw}}\right)=\left(1+\alpha_c\right)\left(1+\frac{\sigma_c}{E_{bc}}\right). \tag{4.23}$$

In Eq. (4.22), we can make a simplification, considering only the first order terms of the products. In fact, having all the terms an order of magnitude of 10^{-3}, the products between them become three orders of magnitude smaller (10^{-6}). Thanks to this simplification, we get:

$$\alpha_b-\frac{\sigma_w}{E_{bw}}=\alpha_c-\frac{\sigma_c}{E_{bc}}. \tag{4.24}$$

And, consequently:

$$\alpha_b-\alpha_c=\frac{\sigma_w}{E_{bw}}-\frac{\sigma_c}{E_{bc}}. \tag{4.25}$$

Reordering the terms, we obtain:

$$\alpha_b - \alpha_c = \frac{\sigma_w}{E_{bw}} - \frac{\sigma_c}{E_{bc}} . \tag{4.26}$$

Writing the stress at cold as a function of that one at warm:

$$\sigma_c = \frac{E_{bc}}{E_{bw}} \sigma_w - (\alpha_b - \alpha_c) E_{bc} . \tag{4.27}$$

It follows that the ratio between blocks elastic moduli at cold and at warm temperature should be equal to 0.55 to satisfy the relation find out examining the experimental data (4.10), but an elastic modulus that results bigger at warm than at cold temperature has not physical meaning. Indeed, after cooling, coil material becomes more rigid and the modulus consequently increases, so that the ratio should be bigger than one. For this reason, this ratio can be consider valid only if we suppose linear the relation between ε and σ relative to the blocks. In the following, we will show that this paradox comes out from the linear approximation of the $\sigma(\varepsilon)$ curve. The ratio between Young moduli in fact becomes bigger than 1, as expected, if the nonlinear behavior of the coils is taken into account.

Now, we consider in the computation of the elastic moduli the experimental laws, still neglecting the influence of collar deformations:

$$\varepsilon_{bw} = \frac{l_{bwo} - l_{bw}}{l_{bwo}} = \sqrt{\frac{\sigma_w}{F_{bw}}} \tag{4.28 a}$$

$$\varepsilon_{bc} = \frac{l_{bco} - l_{bc}}{l_{bco}} = \sqrt{\frac{\sigma_c}{F_{bc}}} \tag{4.28 b}$$

$$\varepsilon_{cw} = \frac{-l_{cwo} + l_{cw}}{l_{cwo}} = \frac{\sigma_w}{E_{cw}} \cong 0 \tag{4.28 c}$$

$$\varepsilon_{cc} = \frac{-l_{cco} + l_{cc}}{l_{cco}} = \frac{\sigma_c}{E_{cc}} \cong 0 \tag{4.28 d}$$

If one extrapolates lengths of collar and blocks under no load, one gets:

$$l_{bw} = l_{bw0}\left(1-\sqrt{\frac{\sigma_w}{F_{bw}}}\right) \tag{4.29 a}$$

$$l_{bc} = l_{bc0}\left(1-\sqrt{\frac{\sigma_c}{F_{bc}}}\right) \tag{4.29 b}$$

$$l_{cw} = l_{cw0} \tag{4.29 c}$$

$$l_{cc} = l_{cc0} \tag{4.29 d}$$

Calling the thermal contraction relations, Eq. (4.18 *a*) and Eq. (4.18 *b*), substituting into the Eq. (4.28 *a*) and into the Eq. (4.28 *c*), one obtains:

$$l_{bw} = l_{bc0}\left(1+\alpha_b\right)\left(1-\sqrt{\frac{\sigma_w}{F_{bw}}}\right) \tag{4.30 a}$$

$$l_{cw} = l_{cc0}\left(1+\alpha_c\right) \tag{4.30 b}$$

In this calculation too, we assume that copper wedges deformations are negligible, so that (4.21 *a*) and (4.21 *b*) are still valid. For this, we can equate the second terms of (4.30 *a*) and of (4.30 *b*), and the second terms of (4.29 *b*) and (4.29 *d*). We obtain:

$$l_{bc0}\left(1+\alpha_b\right)\left(1-\sqrt{\frac{\sigma_w}{F_{bw}}}\right) = l_{cc0}\left(1+\alpha_c\right) \tag{4.31 a}$$

$$l_{bc0}\left(1-\sqrt{\frac{\sigma_c}{F_{bc}}}\right) = l_{cc0} \tag{4.31 b}$$

Dividing term by term, one obtains:

$$\left(1+\alpha_b\right)\left(1-\sqrt{\frac{\sigma_w}{F_{bw}}}\right) = \left(1+\alpha_c\right)\left(1-\sqrt{\frac{\sigma_c}{F_{bc}}}\right) \tag{4.32}$$

$$\alpha_b - \alpha_c = \sqrt{\frac{\sigma_w}{F_{bw}}} - \sqrt{\frac{\sigma_c}{F_{bc}}} \tag{4.33}$$

Reordering the terms and squaring, we obtain:

$$\sqrt{\frac{\sigma_c}{F_{bc}}} = \sqrt{\frac{\sigma_w}{F_{bw}}} - (\alpha_b - \alpha_c) \tag{4.34}$$

$$\sigma_c = F_{bc}\left(\frac{\sigma_w}{F_{bw}} - 2(\alpha_b - \alpha_c)\sqrt{\frac{\sigma_w}{F_{bw}}} + (\alpha_b - \alpha_c)^2\right). \tag{4.35}$$

Now, we impose, as in Eq. 4.3.1, a zero coil prestress at cold temperature. In this case, we have:

$$\sigma_w = (\alpha_b - \alpha_c)^2 F_{bw} \tag{4.36}$$

from which we obtain:

$$\alpha_b = \alpha_c + \sqrt{\frac{\sigma_w}{F_{bw}}} \tag{4.37}$$

$\sigma_w = 20 \pm 10$ MPa

$F_{bw} = 3.6 \cdot 10^5$;

$\alpha_c = 2.6 \cdot 10^{-3}$

One obtains also in this case $\alpha_b = 10 \cdot 10^{-3}$. Let us now derive the slope of the relation σ_w / σ_c. One has to derive the expression of σ_c with respect to σ_w and then to impose the experimental results $\frac{\partial \sigma_c}{\partial \sigma_w} \cong 0.55$.

$$\frac{\partial \sigma_c}{\partial \sigma_w} = F_{bc}\left(\frac{1}{F_{bw}} - \frac{2(\alpha_b - \alpha_c)}{2\sqrt{\sigma_w}\sqrt{F_{bw}}}\right) = \frac{F_{bc}}{F_{bw}}\left(1 - \frac{(\alpha_b - \alpha_c)\sqrt{F_{bw}}}{\sqrt{\sigma_w}}\right) = 0.55 \tag{4.38}$$

We can now use this relation to derive F_{bc}:

$$F_{bc} = \frac{0.55 \cdot F_{bw}}{1 - \frac{(\alpha_b - \alpha_c)\sqrt{F_{bw}}}{\sqrt{\sigma_w}}} = \frac{0.55 \cdot F_{bw}}{1 - \frac{(7.5 \cdot 10^{-3})\sqrt{3.6 \cdot 10^5}}{\sqrt{\sigma_w}}} \tag{4.39}$$

It is then possible to calculate the ratio between F_{bc} and F_{bw}. For a warm prestress of 80 MPa, this value becomes 1.08. We can now calculate, on this base, the ratio between the Young modulus at warm and at cold temperature. We remember the relations already given:

$$\varepsilon_{bw}\sqrt{\frac{\sigma_w}{F_{bw}}} \tag{4.28 a}$$

$$\varepsilon_{bc} = \sqrt{\frac{\sigma_c}{F_{cw}}} \tag{4.28 b}$$

From them, squaring, one can deduce:

$$\sigma_w = \varepsilon_{bw}^2 F_{bw} \tag{4.40 a}$$

$$\sigma_c = \varepsilon_{bc}^2 F_{bc} \tag{4.40 b}$$

from which:

$$E_{bw} = \frac{\partial \sigma_{bw}}{\partial \varepsilon_{bw}} = 2\varepsilon_{bw} F_{bw} \tag{4.41 a}$$

$$E_{bc} = \frac{\partial \sigma_{bc}}{\partial \varepsilon_{bc}} = 2\varepsilon_{bc} F_{bc} \tag{4.41 b}$$

The ratio between the two Young moduli is:

$$\frac{E_{bc}}{E_{bw}} = \frac{\varepsilon_{bc}}{F_{bw}}\frac{F_{bc}}{\varepsilon_{bw}} = \sqrt{\frac{\sigma_c}{F_{bc}}}\frac{F_{bc}}{F_{bw}}\sqrt{\frac{F_{bw}}{\sigma_w}} \cong \sqrt{\frac{F_{bc}}{F_{bw}}} = 1.04$$

In this way, we can see that the real ratio between cold and warm Young moduli is more than one, as expected from physical considerations. It our simulation model, the ratio will be 1.

5 RESULTS OF THE FINITE ELEMENT MODEL OF THE DIPOLE

5.1 General remarks

The finite element model of the dipole cross section built up with ANSYS® (see section 3) has been used to evaluate stress loading and displacements. All calculations have been done at cryogenic temperature (1.9 K), fixing the coil azimuthal prestress at 40 MPa. The most important goal is to know the position of coil cables, from which field components depend. We evaluate the cable displacements and corresponding multipoles at injection conditions, that is the most critical for field quality, omitting the force of Lorentz effects on the cables.

The induced deformations found with ANSYS® are post-processed by a set of "ad hoc" developed programs, called ANSIA [15], that transforms the displacements file into an input file readable by ROXIE [3], the magnetostatic code. Input files for ANSIA are:

- the ROXIE file containing the nominal geometry;
- the ANSYS® output file containing the coil node positions at nominal geometry;
- the ANSYS® output file containing the coil node positions in the test case (depending on the coil length used);
- the file containing ANSYS® node numbers corresponding to conductor blocks vertexes;
- the ANSYS® output file containing the coil node displacements.

ANSIA produces the ROXIE input files describing undeformed and deformed geometry. These files are input in ROXIE, which computes the magnetic field and the multipolar components induced by deformations (see Chapter 4.3). Results are used to find the effect of coil deformations on the multipolar components (see Eq.2.17) in the magnetic field. Moreover, the influence of coil length and collar shapes on the field quality is evaluated.

In each calculation, resulting multipolar components are compared to nominal values, i.e. the ideal magnetic field component values expected for the nominal geometry without any construction error. Expected multipoles result from a process of optimization where the cross section of the magnet is designed as to minimize the effect of persistent currents (see Chapter 2.3). Effects of parameter variation and of dimensional variations within mechanical tolerances on field quality are always expressed in terms of the error with respect to the nominal field. Multipolar coefficient nominal values are reported in Table 5.1.

Table 5.1: Nominal values of the geometrical multipole components at injection. Units of 10^{-4} at the reference radius R_{ref} = 17 mm

Normal components	**Values**
b_2	4.25
b_3	7.32
b_4	0.01
b_5	-1.05
b_6	0.00
b_7	0.63
b_8	0.00
b_9	0.10
b_{10}	0.00
b_{11}	0.61
b_{12}	0.00
b_{13}	0.08
b_{14}	0.00
b_{15}	0.03
b_{16}	0.00
b_{17}	-0.05

5.2 ANSYS® output results

Since we are mostly interested in displacements and stress solicitations for coils, we used a polar coordinate system centered in the geometrical center of the aperture to analyze the results. ANSYS® output gives plots and list of values, from which it is possible to evaluate the stress and the displacement distribution in azimuthal and radial direction. The stresses and displacements values are given for each node where the solution is calculated.

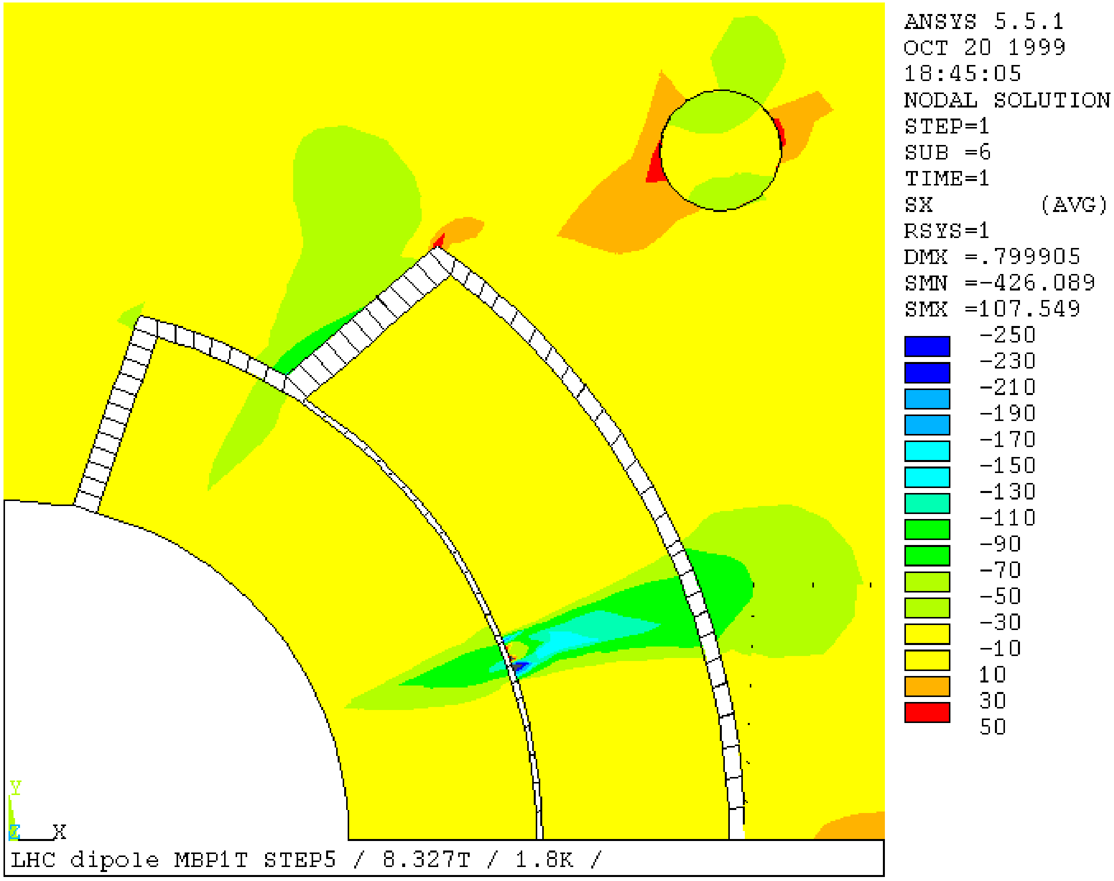

Figure 5.1: Stress distribution of the coils in radial direction for ¼ aperture cross section. Calculations at 1.9 K, average tangential prestress -40 MPa.

As shown in Figure 5.1, the radial stress has a uniform distribution except for the contact zone between the inner coil and outer coil copper wedge. The maximum value of the coil stress is -30 MPa, i.e. compression stress, whilst there are some tension peaks around the pins and on the collar, at the top corner in front of the external coil.

Looking at Figure 5.2, we can see that in the azimuthal direction the stress has a uniform distribution along the whole coil length, with an average of –40 MPa. Both coils have zones of higher stress, in their inner part and in correspondence of the outer coil copper wedge.

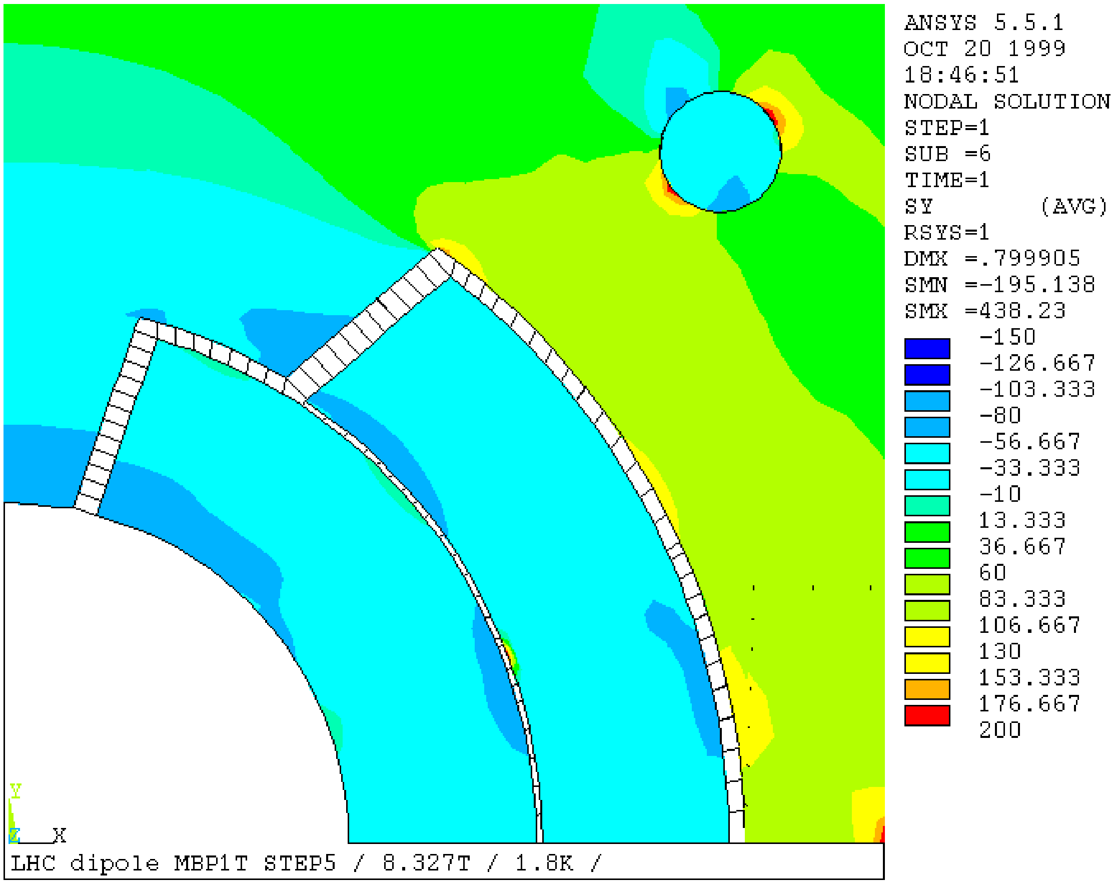

Figure 5.2: Stress distribution for the coils in azimuthal direction for ¼ aperture cross section. Calculation at 1.9 K, average tangential prestress -40 MPa.

The coil deformation is a field of 2D vectors that is evaluated on a finite set of nodes in the magnet cross section and then interpolated to give a surface distribution over all the areas. In Figure 5.3 and Figure 5.4, the distributions of displacements in the coil are shown.

Along the radial direction, displacement values stay between -0.4 mm and -0.08 mm, with the inner part less deformed. In the tangential direction, displacements vary between -0.3 mm on the top of the coils to -0.02 mm on the bottom, next to the mid-plane, where displacements are not permitted by boundary conditions.

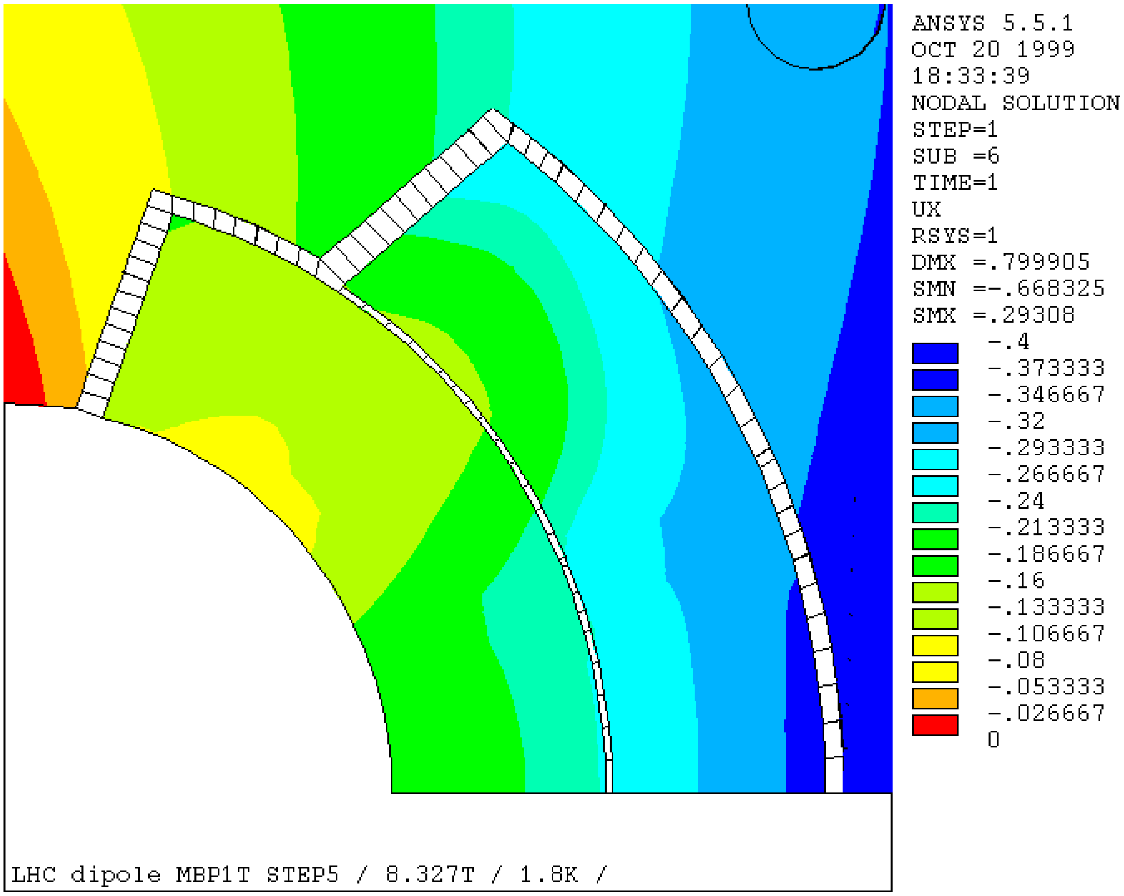

Figure 5.3: Displacements distribution in the radial direction on ¼ of the coil cross section.

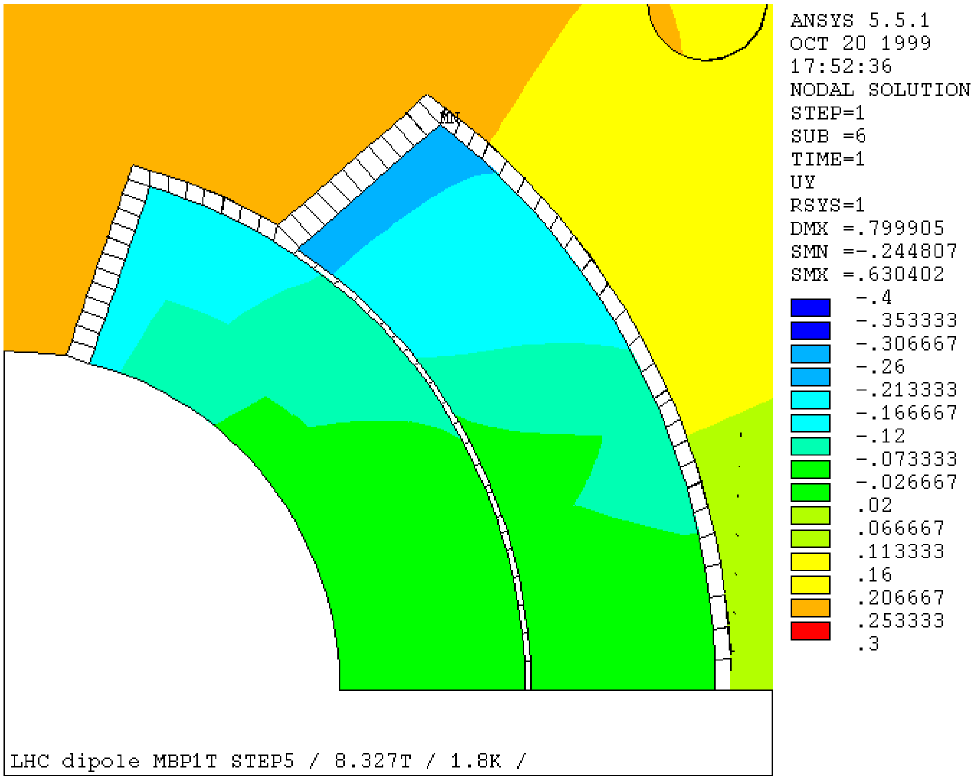

Figure 5.4: Displacements distribution along the tangential direction

5.3 Decomposition of displacements

Since the deformation field is rather smooth, we propose to parameterize it with a low order Taylor and Fourier series. In this way, all the information relative to the deformations can be reduced to a few coefficients, thus simplifying the analysis of the relation between deformation and multipoles. We numerically estimate the influence of single deformation modes on the multipoles, thus identifying the most dangerous [17].

Deformations are implemented in ROXIE as rigid movements of conductor blocks. For this reason, we consider a field deformation defined over the four radii (r_1, r_2, r_3, r_4) = (28, 43.4, 43.9, 59.3) mm that surround the inner and the outer layer of the coils. The field then depends on the discrete variable r_i and on the continuous angular variable φ. Deformations are then decomposed into a radial $dr(r_i, \varphi)$ and a tangential $dp(r_i, \varphi)$ component.

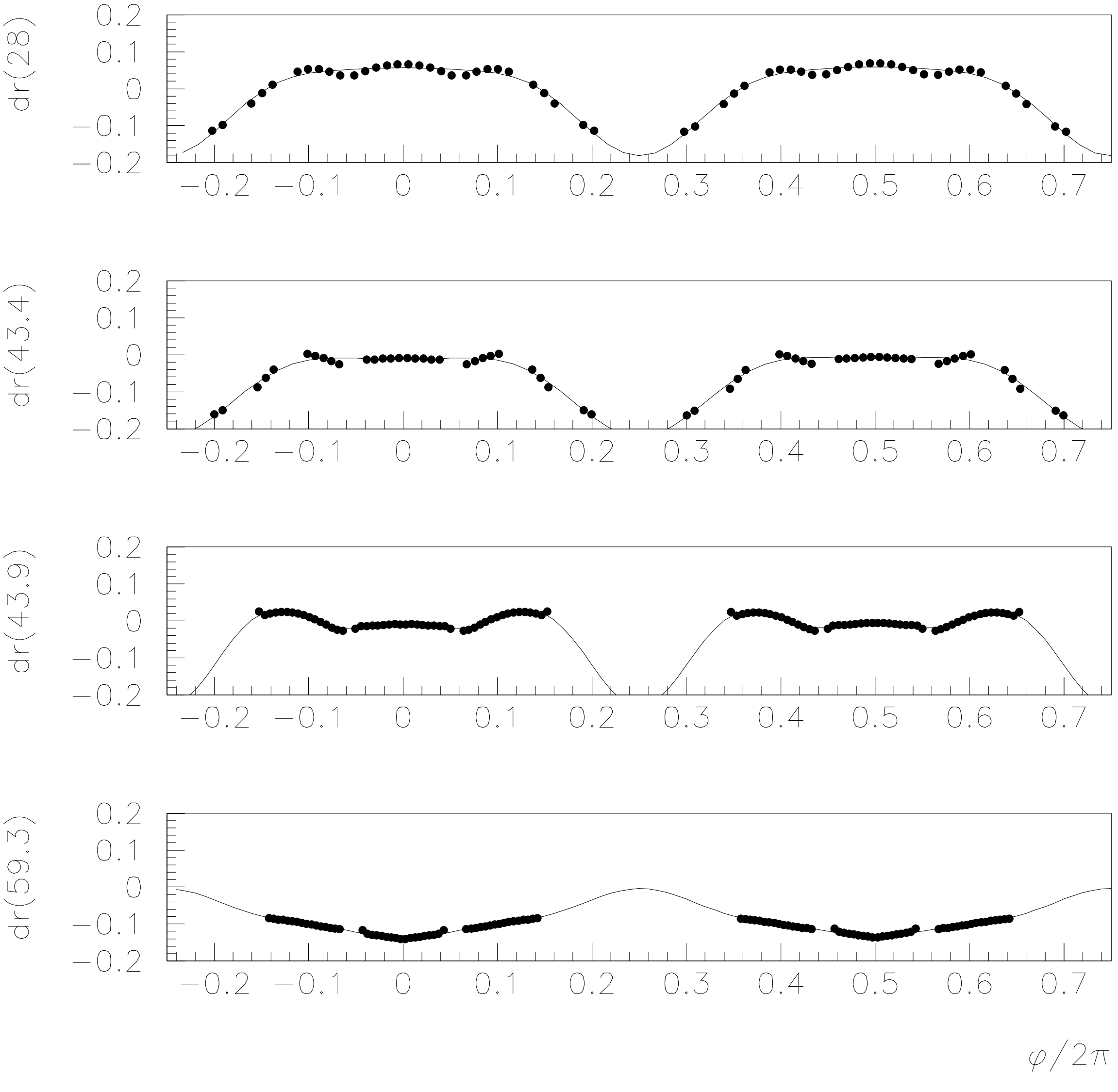

Figure 5.5: Plot of radial deformations for each of the four coils contours, stainless steel collars. Dots, ANSYS® values. Lines, series approximation.

Radial deformations are well described using the first terms of an even Fourier series in the azimuthal variable φ.

$$dr(r_i, \varphi) = \sum_{k=0}^{K} a_{k,i} \cos(k\varphi) \tag{5,1}$$

Here the index i runs over the four concentric circles that surround inner and outer coils, and k run over the modes. The mode zero ($a_{0,i}$) gives rise to a contraction or to a dilatation of the coil; the mode one ($a_{1,i}$) produces an horizontal shift in the coil, whilst higher order modes correspond to radial waves of deformation with decreasing period. The up-down symmetry is responsible for the absence of sine terms in the Fourier series.Tangential deformations are also well approximated by the first terms of an odd Taylor series in each half of the aperture:

$$d\varphi(r_i, \varphi) = \sum_{j=0}^{J} b_{j,i} \varphi^{2j+1} \qquad i=1,4 \qquad \varphi \in [-\pi/2, \pi/2]; \tag{5,2}$$

$$d\varphi(r_i, \varphi) = \sum_{j=0}^{J} c_{j,i} \varphi^{2j+1} \qquad i=1,4 \qquad \varphi \in [\pi/2, 3\pi/2]. \tag{5,3}$$

The zero modes ($b_{0,i}$ and $c_{0,i}$) correspond to tangential compression or dilatation, uniform along the azimuth. Higher order modes correspond to tangential waves of compression and dilatations. Also in this case, the up-down symmetry implies the presence of odd terms only.

In Figure 5.5 and in Figure 5.6, we show the radial and tangential deformations evaluated through ANSYS® (dots) and the series approximation (solid lines) with seven radial modes and two tangential modes (K=6 and J=1). If the displacements evaluated with ANSYS® are replaced by the interpolated field, the resulting multipoles agree with the ANSYS® results (see Table 5.2, last two rows).

This means that low order Taylor and Fourier series can take into account the part of the deformation that are relevant to evaluate multipoles. Each mode contributing to the multipoles is given in Table 5.2. In this table and in the following ones, the multipole component variations are expressed as the difference between the calculated and the nominal components at the injection. The convention adopted gives values as follow:

$$\Delta b_i = b_{i,calc} - b_{i,nom}. \tag{5,4}$$

For symmetry reason, even radial modes only contribute to odd multipoles and odd radial modes to even multipoles.

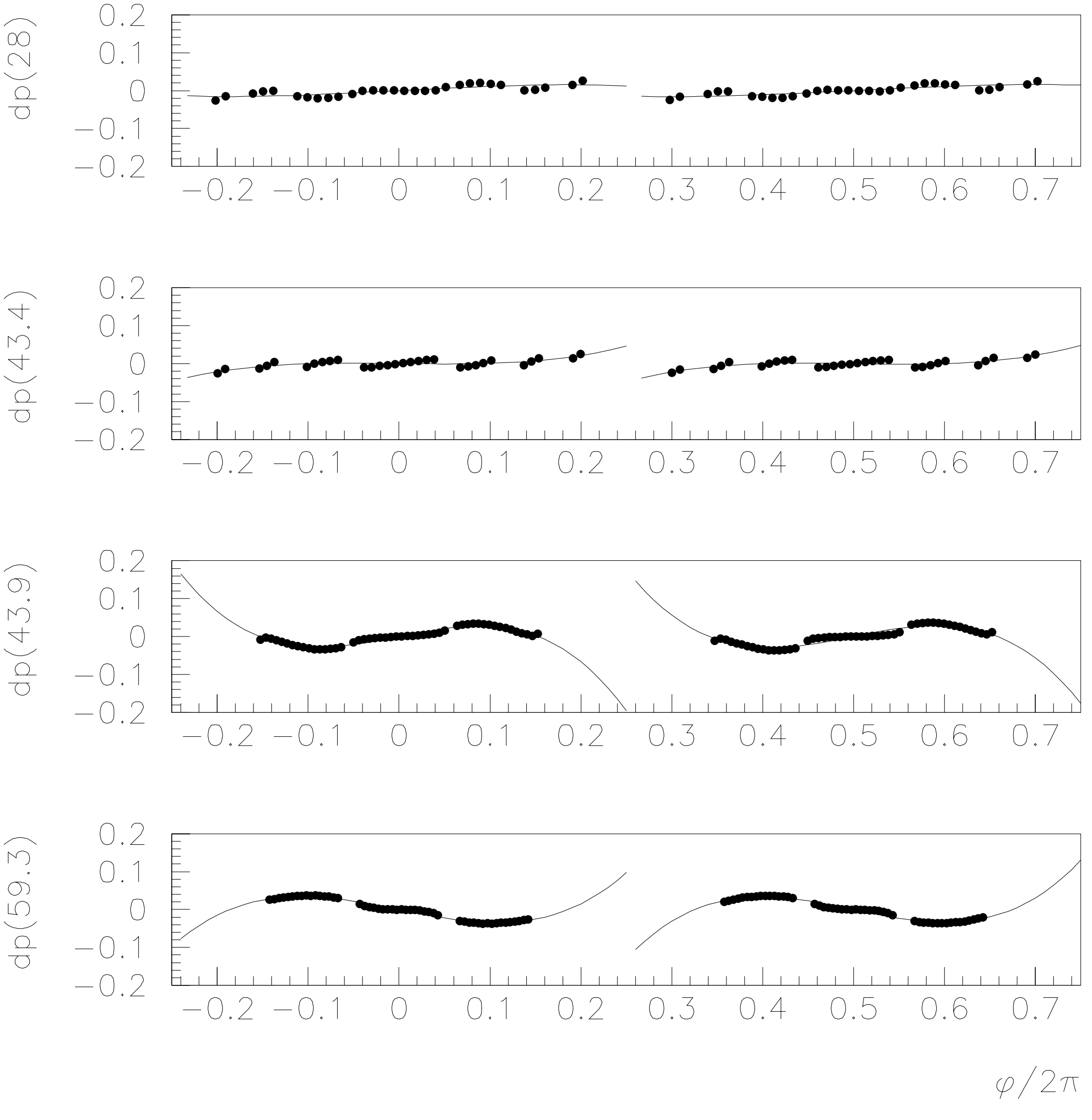

Figure 5.6: Plot of tangent deformations for each of the four coils contours, stainless steel collars. Dots: ANSYS® values. Lines: series approximation.

Table 5.2: Contribution of radial and tangent modes to the multipole components variations induced by deformation, total effect of 7 radial and 2 tangential modes, and comparison with ANSYS® results. Values are given in units of 10^{-4} at R_{ref}=17 mm.

	Δb_2	Δb_3	Δb_5	Δb_7
Radial				
k=0	0.00	0.10	-0.06	0.01
k=1	0.03	0.00	0.00	0.00
k=2	0.00	-3.14	0.18	-0.04
k=3	0.08	0.00	0.00	0.00
k=4	0.00	0.53	0.69	0.01
k=5	0.00	0.00	0.00	0.00
k=6	0.00	0.02	-0.05	-0.07
Tangential				
j=0	0.05	-0.24	-0.06	-0.02
j=1	-0.01	0.01	0.02	0.00
Total	0.15	-2.73	0.72	-0.11
ANSYS®	0.16	-2.79	0.73	-0.12

One can distinguish two main effects.

- The radial deformations of order 2 (i.e. circles are deformed into ellipses, see Figure 5.7) have a strong effect on the sextupole ($\Delta b_3 \cong$ -3 units) and on the decapole ($\Delta b_5 \cong$ 0.2 units).
- Radial deformation of order 4 yields to 0.5 units of b_3 and 0.7 units of b_5.

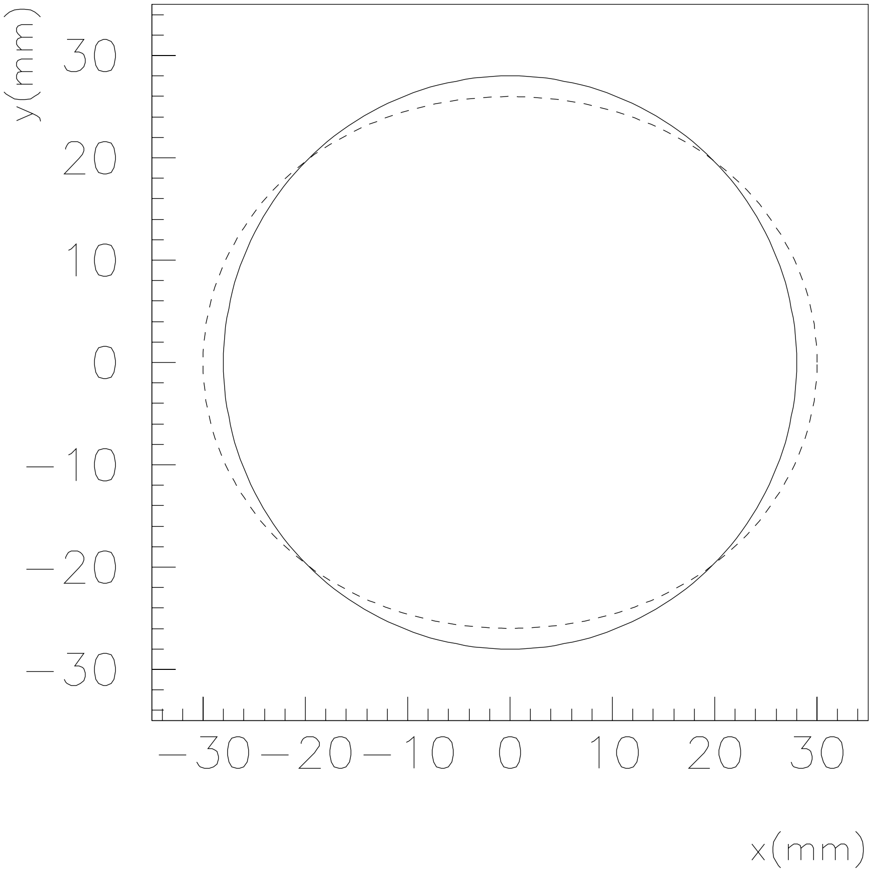

Figure 5.7: Plot of radial deformations, mode 2, in Cartesian coordinates. Undeformed circle (solid line) versus deformed circle (dotted line).

Simulations have also shown that the radial and tangential deformations are rather well decoupled. In Table 5.2 the effect of the tangential modes seems to be very limited, giving only some contribution to b_3. This is because, in our computations, we fixed the initial coil length to an optimal value that allows recovering the nominal length after deformations, at 1.9 K. Indeed, an non-optimized coil length produces a tangential deformation that strongly affects the field multipoles. In this case, tangent deformations due to coil length different from the nominal one have a large influence on b_3, b_5, and b_7. Simulations show that a 0.1 mm longer coil, starting from a non-optimized dimension, gives rise to about -3 units of sextupole and 0.5 of decapole. Therefore, the determination of the exact coil length under manufacturing forces and at cold is crucial to obtain a correct estimate of the absolute value of the multipoles.

The contributions of other deformation modes are not very relevant, giving rise to multipole shifts of less than 0.1 units. In particular, the following effects are negligible:

- The effect of the first order tangential mode (tangential waves of compression and dilatation, see Table 5.2, mode $j = 1$) is negligible.
- The radial mode of order zero, i.e. the radial shrinkage due to low temperature, is negligible (see Table 5.2, mode $k = 0$).
- Odd radial modes, i.e. modes related to left-right asymmetries are very low. Therefore, deformations have negligible effect on even multipoles (see Table 5.2, mode $k = 1,3,5$).

This theme will be better discussed later, in 5.4.3, where parametrical analysis of coil length is explained.

5.4 MECHANICAL TOLERANCES

5.4.1 General remarks on the problem

Mechanical pieces are always affected by errors with respect to their nominal geometry, due to the machining process. For LHC dipole magnet components, the nominal tolerances have been determined essentially by mechanical stability requirements [18]. Indeed, it is useful to know the effects of these tolerances on field quality. If they are too large, it is possible that the field quality is not good enough for the particle beam stability. On the other hand, tight tolerances correspond to high production costs and bring the construction process close to the limits of present manufacturing techniques. Knowing the influence of the effects of coils and collars dimensions errors on the field quality, is interesting for two reasons:

- possibility to relax tolerances and to reduce production costs;
- chance to take field quality corrective actions modifying only some magnet components even after the magnet is built.

In the next paragraph, different methods to evaluate these effects will be described and simulation results will be shown.

5.4.2 Methods to evaluate tolerances effects on field quality

Tolerance effects on field quality can be evaluated in different ways, taking into account coils and collar deformations induced by assemblage and cooling or reducing displacements to simple rigid movements of the cables blocks. A first estimation can be done considering only this rigid motion [19]. In this way, it is possible to treat variations in the tangential dimensions of coils and errors on the inner radial part of the collars, i.e. the so-called nose. Nevertheless, using a rigid model it is not possible to evaluate geometry errors on the inner arcs of collars that instead will cause real coil deformations. Anyway, a first estimation of the effects of coil length variation was done using this simplified method. Radial and azimuthal positions of each block of superconducting cables were varied in an independent manner, using a Gaussian distribution around the nominal positions, with an appropriate value of standard deviation.

If we want to give a more precise evaluation of the effects of collar deformations, of the coils different behavior under compression and of the geometry error in circular zone, we have to create a model that is able to calculate deformations [20]. We have built up a model using the finite element code ANSYS®, described in chapter 3. In principle, in order to change the geometry of a component in the model, one should define a new position for the corresponding keypoint, i.e. vertexes of uniform material areas inside the model. In some cases, e.g. for the collars keypoints, this procedure is not straightforward, since a variation in the keypoints position would influence also the geometry of other components, that is defined in terms of the collar internal surface. In such cases, it is convenient to use the interference property of the contact elements instead, already treated in 3.3.3.

Dimensional variations of coil components (blocks of cables and copper wedges) are simulated applying a real change on the geometry design in the finite element model, where all the nominal dimensions are inserted as parameters. This is the best solution, because with keypoints movement it is possible to maintain the required precision both in deformation results and in stress values. Using contact elements interference indeed, some errors occur in evaluating local displacements without the necessary precautions.

Tolerances on collar geometry are simulated using the interference property of contact elements, on boundary surfaces between coils and collars (see 3.2.3.2). In this zone of the model, contact elements are used to reproduce the effects of the presence of insulation layers and shims, which are not explicitly modeled. As already seen in 3.2.3.2, contact elements react like linear springs, transmitting a force directly proportional to their normal stiffness *K*, estimated according to:

$$K = \frac{AE_{eq}}{h}, \tag{5,5}$$

where A is the area on which the single contact element insist, E_{eq} is the elastic modulus of all material layers inserted between coils and collars and h is the element length. If contact elements are given a certain interference value, it means that the spring is pre-loaded and transfers a normal force to the two surfaces in contact, even if no external load is applied. Giving a higher or lower interference value for contact elements between coils and collars, we obtain a transmitted force that is higher or lower for the surfaces that are in contact. Obviously, the force will still be proportional to the element stiffness. Assuming that the error made incrementing this force and not moving keypoints of the collars to add steel has negligible influence on the stress values, as seen in 3.2.3.2, we can simulate a collar geometry different from the nominal one.

In principle, the geometrical deviation from the nominal design of dipole components, like collars, copper wedges, or superconducting blocks, can have any shape. In practice, the production process limits the possible geometry errors. Analyzing the measurements of the available components, we decided to use shapes of the following type.

- We assume that straight lines of the design are preserved and only the end-points of each segment can be displaced, within tolerances, in the same direction (line shift) or in opposite direction (line tilt), see Figure 5.8.
- When arcs of circumference are considered, we assume that the circular shape is preserved and that only the arc end-points can move, within tolerances, in the same direction (shift) or in the opposite direction (tilt), see Figure 5.8.
- Shifts are considered positive when in this way components to which shift is applied result smaller, while tilt are considered positive when the rotation is counter clockwise on the right part of the aperture and clockwise on the left part.

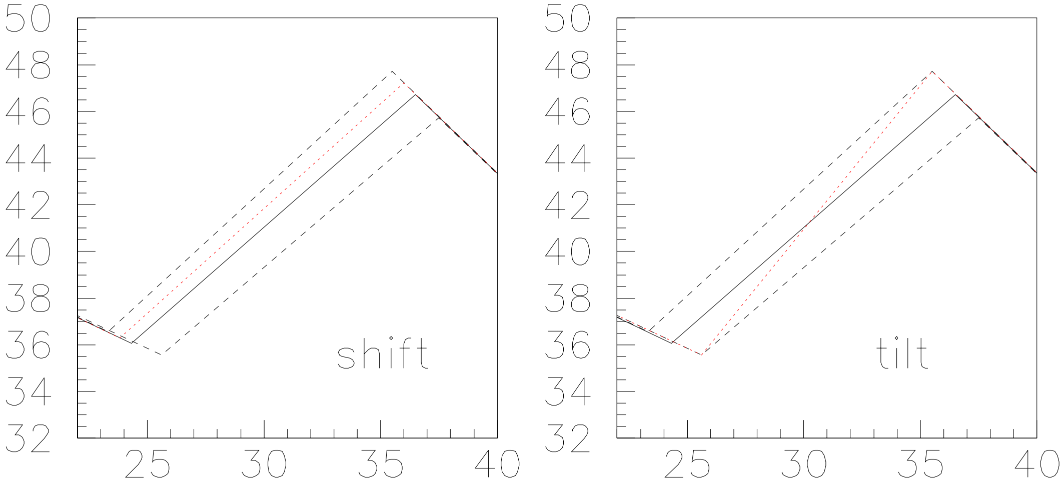

Figure 5.8: Positive shift (left), positive tilt (right).

In a tilt or in a shift the end-points are displaced of the same amount in equal or in opposite directions, respectively. Errors are given a Gaussian distribution, centered on the nominal dimension. The specified tolerances are assumed to represent $3 \cdot \sigma$ of this Gaussian distribution.

For each zone of study, we launched a loop of a certain number of calculations, with different interference or parameter values. Nominal geometry corresponds to the central case for both collar and coil studies, where the errors have the same probability to be of positive or negative sign with respect to the nominal geometry.

Some calculations have to be done defining the coil length. Coil nominal dimension is in fact defined at 1.9 K and under a 40 MPa compression, but its azimuthal length at room temperature and in absence of stress can be obtained with the ANSYS® model itself.

A first calculation is made starting with nominal dimension at room temperature, without stress. Tangential deformation due to assembly and cool down is measured. Than, this value is added to the nominal length to obtain a coil that correspond to project dimensions once assembled and cooled down. This coil dimension represents the central case in each set of calculations.

Five cases are taken for each simulation to cover a range wide enough to prove linear behavior of the function which correlates geometry errors and multipolar coefficients, but also to maintain reasonable working machine time. Interference values vary from nominal value -0.1 mm to nominal value +0.1 mm. This range has been chosen because it permits to cover a much wider range than the tolerance on collar dimensions.

Since our model contains only one quarter of the cold mass cross section, we can only describe shape errors with an inherent up-down symmetry, inducing normal multipoles in the magnetic field. In real life however, skew multipoles will appear, because of the up-down tolerances, and normal and skew harmonics are expected to have the same order of magnitude.

5.4.3 Tolerances on coils

In order to model the tolerances on the coils one has to carefully analyze the industrial process that gives rise to the construction of the coils. We have already discussed in section 2.2.1.3 the coil components and their assemblage. Tolerances on the coil components are the sequent:

- The azimuthal length of the copper wedges can be between 0 and 50 μm longer than the nominal value.
- The thickness of each conductor can vary in the range ± 6 μm. This implies that the inner coil length, containing 15 conductors, can vary by ± 90 μm, and the outer coil length, made by 25 conductors, can vary by ± 150 μm.
- The polyimide insulation has a thickness uncertainty of ± 5 %, inducing a total uncertainty of ± 180 μm for the inner coil and of ± 300 μm in the outer coil.

Summing all these tolerances, the global variation of the coil azimuthal length is of several tenths of millimeters. Indeed, a much lower tolerance is required on this dimension (± 20 μm), after the curing process. In practice, the tolerance of the azimuthal coil length after curing is only determined by the tolerances of the curing mould, since all the component uncertainties are smoothed down by the compression and the heating of the polyimide insulating film. It is reasonable to assume that the copper wedges preserve the original azimuthal length, since they are rather rigid. We also assume that the blocks are deformed proportionally to the number of conductors, until they recover the assumed value of the azimuthal coil length. In these conditions the uncertainty of the insulating film and of the conductors are in practice, ineffective. Summarizing, we used the following tolerances for the cured coil:

- Azimuthal coil length: ± 20 µm.
- Azimuthal copper wedge length: 0 to 25 µm.

In addition to that, we always considered a perfect four-fold symmetry in the coil shape for each dipole aperture, to simplify our simulations.

An estimation of the calculated effects is given in Table 5.3, where sensitivities of multipoles to a shift of + 0.1 mm on the coils length is given. In the first rows results are given for simple variations on the single coils (internal or external), whilst in the last row combined effects on the two coils are presented.

Table 5.3: Multipoles variations for coils 0.1 mm longer with respect to the nominal geometry.

	b_3	b_5	b_7
Inner coil	-2.22	0.41	-0.14
Outer coil	-1.36	0.05	0.02
Both coils	-3.59	0.47	0.12

Because of the restrictive hypothesis on the symmetry of the model, we can study variations of the odd normal multipoles only. Even multipoles (b_{2n}), arising from left/right asymmetry can be estimated by a geometric average, according to (5,6).

$$b_{2n} = \sqrt{b_{2n+1} \cdot b_{2n-1}} \ . \tag{5,6}$$

The geometric average must be used instead of the arithmetic one since the main dependence of multipoles on the order *n* is a power law.

5.4.4 Tolerances on collars

The collar tolerance zones of study are split in straight or circular parts labeled as shown in Figure 5.9. Simulations show that the effect of tolerances on the external part of the collar (9,10,11) have a very limited effect on the coil deformations, as expected. On the other hand, regions 1 to 8, which correspond to the internal part of the collar, strongly influence the coil deformation and therefore field quality.

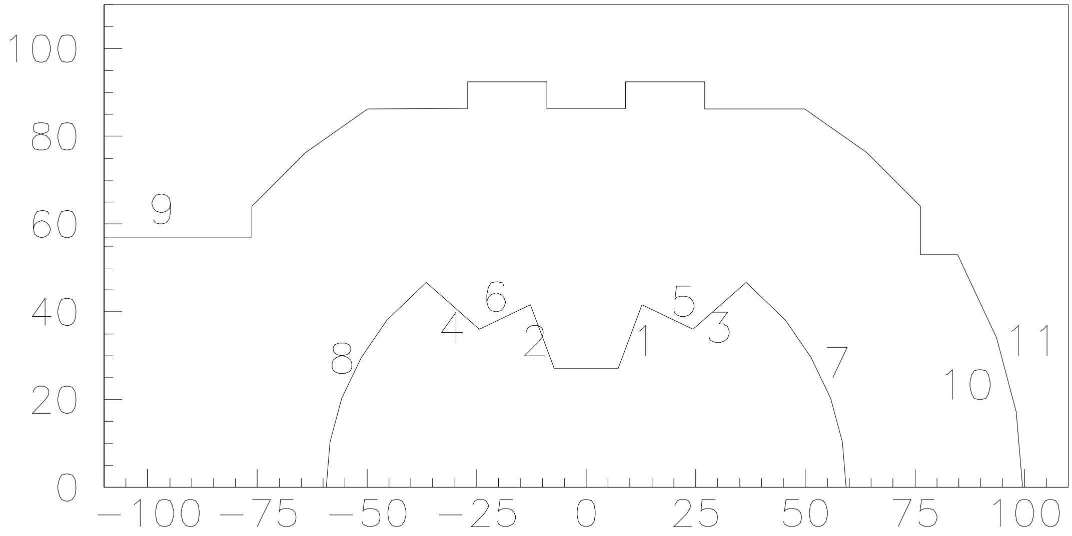

Figure 5.9: Schematic representation of the one-half collar. The numbers indicate the area affected by mechanical tolerances.

A shift or a tilt in these regions may produce a sizeable change of the field-shape multipoles, because these surfaces are the ones nearest to the cables, from whose position the field depends. In the following, we will concentrate our analysis on these parts, analyzing each of them separately.

We first present the data relative to the sensitivity, i.e. the variations in each one of the multipoles due to a tilt or a shift of 0.1 mm in each of the regions 1 to 8. An estimate of the sensitivity to this effect is given in Table 5.3 and in Table 5.4. Here, variations of the lowest order harmonics, from b_2 to b_5, are quoted for a shift or a tilt respectively, in the appropriate areas. Again, we give the variation in the multipoles due to an error in the collar shape with respect to the nominal field components already presented in Table 5.1.

Table 5.4: Variation of the multipoles in units of 10^{-4} at $R_{REF} = 17$ mm, induced by a shift of 0.1 mm on the internal collar.

Shift region	*b2*	*b3*	*b4*	*b5*
1	1.1	0.5	-0.2	-0.1
2	-1.0	0.6	0.2	-0.1
3	1.2	0.6	0.1	0.0
4	-1.2	0.7	-0.1	0.0
5	0.5	0.9	0.3	-0.1
6	-0.5	0.9	-0.3	-0.1
7	-2.2	-0.9	-0.1	0.1
8	2.2	-1.0	0.1	0.0

As we can see in Table 5.4 and in Table 5.5, positive collar shifts and tilts on symmetrical parts of collar (such as zones 1 and 2), produce effects according to previous symmetry considerations (see section 2.3). Even multipolar components are equal in absolute value but opposite in sign for symmetric zones of the collar, whilst odd ones are equal both in value and in sign.

The induced multipoles vary almost linearly with the shape errors in the range ± 0.1 mm, considered in our calculations. This is shown, for instance, in Figure 5.10, where the low order harmonics b_2 to b_5 are plotted as a function of the inner left collar-nose size (region 2). In the same Figure, we also show the difference of behavior between our model (solid lines) and a model (dotted lines) where all the effect of the tolerances is rigidly transmitted to the coil, without taking into account deformations. The latter are results taken out using the "rigid" model, already quoted in 5.4.2.

Table 5.5: Variation of the multipoles in units of 10^{-4} at $R_{REF} = 17$ mm, induced by a tilt of 0.1 mm on the internal collar.

Tilt region	*b2*	*b3*	*b4*	*b5*
1	-0.4	-0.2	0.02	0.2
2	0.4	-0.2	-0.03	0.2
3	0.04	0.02	-0.01	0.0
4	-0.06	0.04	0.01	0.0
5	0.4	0.7	0.3	0.1
6	-0.4	0.7	-0.3	-0.1
7	-0.4	-0.7	-0.4	-0.1
8	0.5	-0.7	0.4	-0.2

The previous results can be used both to relax mechanical tolerances and to identify corrective actions on field quality. New mechanical tolerances will permit the use of components already built but not satisfying the old ones, more restrictive. This will also reduce production costs.

Corrective actions indeed, are based on the use of different thickness shims between the coils and the collar nose or even in the collar cavity, along the curved zone of the collars. They will be useful especially after magnet construction, when, measuring the field, errors will have to be corrected. Knowing the effects on single components of different geometric errors, it will be possible to make corrections only on some of them, maintaining the pieces already built, just disassembling the magnet. However, this is not a trivial task, since one has to avoid stress variations in excess of ± 5 MPa, to preserve the optimum stress window of the layers.

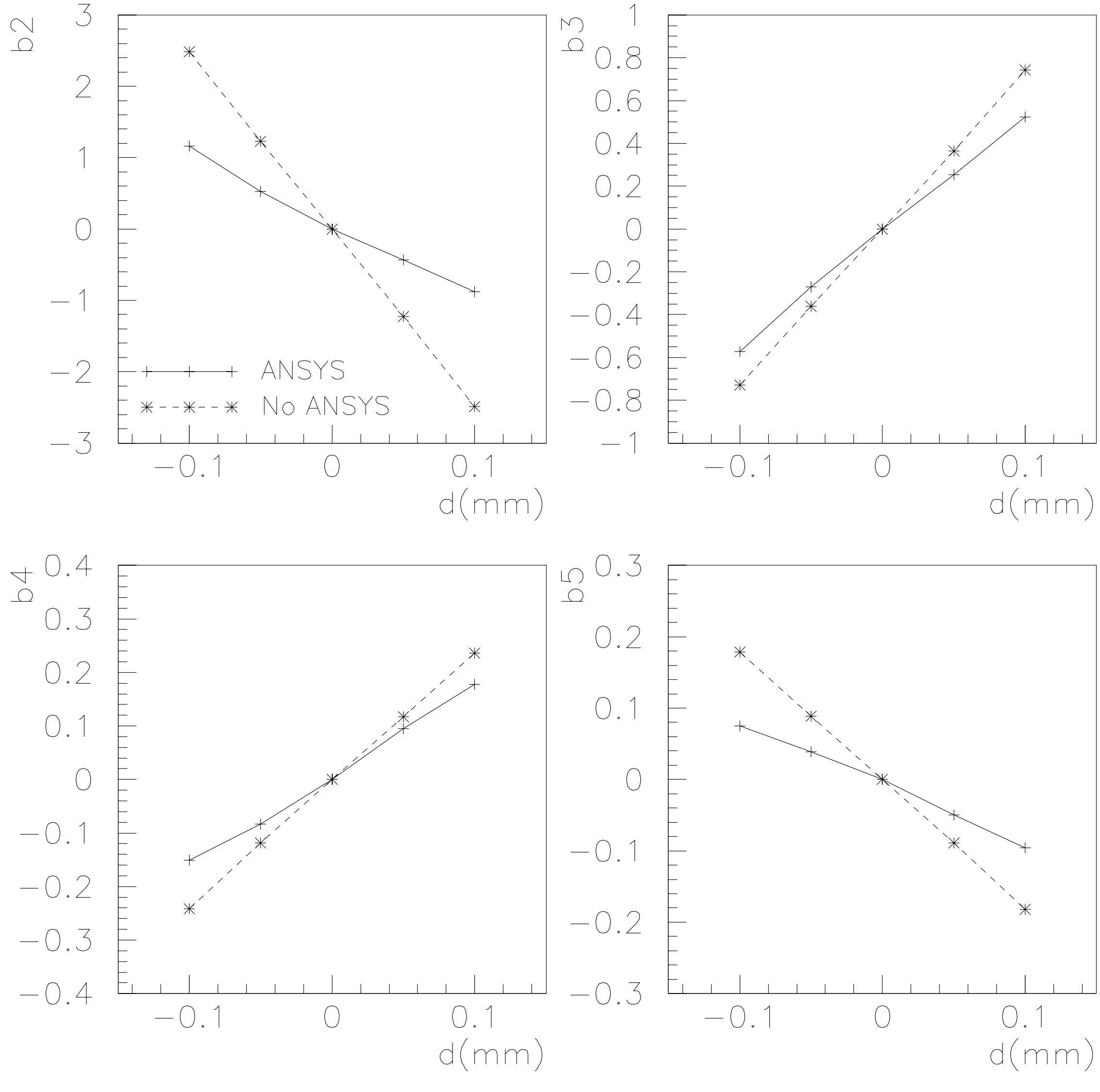

Figure 5.10: Multipoles versus shift of the inner left collar-nose (region 2).

5.5 Monte Carlo analysis

5.5.1 Estimate of several tolerances effects

In the previous section, we calculated the effects of single tolerances; indeed, different tolerances all act together and it is important to find their effect on field quality. It is possible, in fact, that some geometry error, summed to another, give an effect that is different from the algebraic sum of their previously calculated effect. To evaluate this phenomenon, it is possible to adopt different approaches. Let's write the shift induced on multipole b_n by an error t_j in the j zone of the profile according to the equation:

$$\Delta b_n = A_{nj} t_j . \tag{5,7}$$

In equation (5,7), A is the sensitivity matrix filled with values of Tables 3.3 and 3.4 for the collar zones and Table 5.3 for coil length. In a linear approximation, the error distribution for the component b_n is given by:

$$\sigma(b_n) = \sum_j \left| A_{nj} \right| \cdot \tau_j \tag{5,8}$$

where:

τ_j = error t_j sigma (1/3 tolerance range).

Using this approximation, we do not take into account the possibility of self-compensating errors, i.e. we overestimate the total tolerance error. Because of that, it is better to calculate the sigma of each multipole as a sum in quadrature of the single tolerance contributes:

$$\sigma(b_n) = \sqrt{\sum_j A_{nj}^2 \cdot \tau_j^2} . \tag{5,9}$$

To have a better precision and also to take into account error distribution, we used a Monte Carlo method to evaluate real tolerance effects.

5.5.2 Monte Carlo method

Monte Carlo method is based on the use of sequences of random numbers to contemporary vary all the involved parameters and to study their combined effect on the controlled quantities, in our case the multipolar components [22]. The physical system has to be described by probability density functions. In our case, we assume Gaussian distributions. We analyze separately the effect of tolerances on different zones of magnet components and afterwards all the zones were put together, to have a complete view. For each case, a file containing random numbers is used to distribute the errors. Random numbers, created with a routine implemented at CERN, have a Gaussian distribution around zero, with $3\sigma = 1$. Each parameter is given a value equal to its nominal one to which the tolerance multiplied by a random number is added. In this way, the errors distribution becomes a gaussian one, centered on the nominal value, truncated at 3σ, corresponding to the maximum allowed dimension. For each calculation loop, correlations between multipoles were calculated, according to the equation (5,10).

$$r = \frac{\sum \left(b_i - \overline{b_i}\right)\left(b_j - \overline{b_j}\right)}{\sqrt{\sum \left(b_i - \overline{b_i}\right)^2 \sum \left(b_j - \overline{b_j}\right)^2}}. \tag{5,10}$$

Here, b_i and b_j are the multipolar coefficient for which correlation has to be calculated, $\overline{b_i}$ and $\overline{b_j}$ are the medium values of them. Correlation indicates how well the couples of points (b_i, b_j) approximate a line. Its value can vary between -1 and +1, giving a good result if it is next to ± 1, saying that multipoles are not correlated if $r \approx 0$ [23].

5.5.3 Application to coils length

We use Monte Carlo simulation to study 100 different coil realizations with shape errors within tolerances. First, we studied separately the tolerances on copper wedges and on cable blocks. Tolerances applied were:

- ±0.025 mm on copper wedges;
- ±0.020 mm on cables blocks.

The results are given in Table 5.6. In the first row, copper wedges dimensional variations within tolerances are reported. In the second line, coil blocks dimension variation effects are examined. The total r.m.s variation of the multipoles is clearly within the target values considered tolerable for the stability of the circulating beam in the LHC reported in the last row [24].

Table 5.6: R.M.S. variation of the multipoles in units of 10^{-4} at R_{REF} = 17 mm, estimated by 100 seeds Monte Carlo simulation for coil tolerances.

Shape error	b_2	b_3	b_4	b_5
Copper wedge	-	0.21	-	0.05
Coil length	-	0.06	-	0.02
All coil	-	0.22	-	0.05
Target values	-	1.50	0.50	0.70

In addition, because of the asymmetric tolerance of the copper wedge thickness, the average sextupole decreases by 0.7 units and the average decapole by 0.1 units at R_{REF} = 17 mm. No correlation is found between the harmonics of different orders evaluating copper wedge and copper wedge plus coil length variations together, whilst, studying coil length variations, a certain correlation is found between b_3, b_5, b_7 and b_9.

5.5.4 Application to collar tolerances

For collar tolerance studies, we also used the Monte Carlo method to simulate the simultaneous action of all possible shape errors. We consider the following tolerances:

- ± 10 μm on the nose (shapes 1, 2, 3 and 4 in Figure 5.9)
- 0 to 40 μm on the collar cavity (shapes 5, 6, 7, 8)
- ± 20 μm on the external collar (shapes 9, 10, 11).

For each shape, we consider errors with a Gaussian distribution truncated at $3\cdot\sigma$, where $\pm 3\cdot\sigma$, covers the whole tolerance. We consider 100 realizations of the possible error configurations, generated by 100 different seeds, we apply them to our numerical model of the dipole and evaluate the statistical properties of the induced shown in Table 5.7. The induced multipoles are within the specifications. In particular, the multipoles are at least an order of magnitude smaller than the target considered tolerable for the stability of the circulating beam in the LHC.

Table 5.7: R.M.S. variation of the multipoles in units of 10^{-4} at R_{REF} = 17 mm, estimated by 100 seeds Monte Carlo simulation for collar tolerances.

Shape error	b_2	b_3	b_4	b_5
1,2,3,4	0.06	0.03	0.01	0.00
5,6,7,8	0.14	0.10	0.03	0.02
9,10,11	0.01	0.02	0.00	0.00
all tolerances	0.16	0.16	0.04	0.03
Target values	-	1.50	0.50	0.70

This is particularly important, since other effects, like the random fluctuation due to the persistent currents and to the iron magnetization, are not yet included. The multipoles resulting from the Monte Carlo simulation are well approximated (within less that 50 % discrepancy) by the quadratic sum of the multipoles induced by tolerances of the individual regions of the collar. The most sensitive area is the circular part of the cavity, i.e. the regions 5, 6, 7 and 8 of Figure 5.9. The distributions of the geometric multipoles for the 100 seed Monte Carlo simulations are very close to a Gaussian distribution, centered on the nominal values.

We also analyzed correlation between harmonics of various orders. For collars calculations, the correlation is strong between the allowed multipoles b_3, b_5 and b_7, and negligible between the other harmonics. Correlation values are reported in Table 5.8.

The results of these calculations have been used to re-evaluate the tolerances for collar drawings. The initial requirements, used in our simulation, were very demanding, difficult, and costly to be obtained in a consistent manner over mass production. The situation can be substantially improved by relaxing the collar tolerances. Scaling the results of Table 5.7, we can verify that there are no detrimental consequences on field quality when geometrical tolerances of regions 1 to 8 become ± 25 μm and those of regions 9 to 11 become ± 40 μm.

Table 5.8: Correlation between multipoles for all collar tolerances.

2	1.0														
3	-0.1	1.0													
4	0.5	0.0	1.0												
5	0.1	-0.9	0.1	1.0											
6	-0.6	0.0	-0.6	0.0	1.0										
7	-0.1	1.0	-0.1	-1.0	0.0	1.0									
8	0.7	0.0	0.8	0.0	-0.9	0.0	1.0								
9	-0.1	1.0	0.0	-0.9	0.0	0.9	0.0	1.0							
10	0.2	-0.1	-0.1	0.2	0.3	-0.1	-0.3	-0.1	1.0						
11	0.0	0.1	0.0	0.2	0.1	-0.1	0.0	0.1	0.1	1.0					
12	0.8	-0.2	0.7	0.3	-0.8	-0.3	0.9	-0.2	-0.1	0.0	1.0				
13	-0.1	0.9	-0.1	-1.0	-0.1	0.9	0.0	0.9	0.0	0.0	-0.1	1.0			
14	-0.5	-0.2	-0.8	0.2	0.9	-0.3	-0.9	-0.2	0.3	0.1	-0.8	-0.3	1.0		
15	0.1	-1.0	0.0	1.0	0.0	-1.0	0.0	-1.0	0.0	-0.2	0.1	-1.0	0.0	1.0	
16	-0.5	-0.5	-0.3	0.5	0.5	-0.5	-0.5	-0.5	-0.4	-0.1	-0.6	-0.6	0.3	0.5	1.0
17	-0.1	0.3	0.1	-0.2	0.1	0.2	0.0	0.2	0.0	0.1	0.0	0.0	0.0	-0.3	0.0
	2	3	4	5	6	7	8	9	10	11	12	13	14	15	16

6 CONCLUSIONS

The subject of this thesis work has been the analysis of the structural behavior of the LHC superconducting dipoles and its influence on the magnetic field quality. The main goal was to develop a predictive model of the magnet cross section behavior both at room and at cryogenic temperature. In superconducting magnets, field shape errors mostly depend on conductor positions. For this reason, a model that is capable to compute displacements with a precision of 10 μm has been requested.

The finite element code ANSYS® has been used to build up a two-dimensional structural model of the dipole cross-section. The pre-existent FEM model, originally used to perform the structural analysis, has been modified and improved in order to describe in a realistic way the structural behavior and to reach the required precision on deformation evaluation.

Experimental measurements have been taken to determine the material properties of the magnet principal components. The typical feature we had to take into account was the non-linear dependence of the stress versus strain for the coil materials, essential to obtain the required precision on the estimate of conductor displacements. Mechanical test results have been used to describe the non-linear behavior of the dipole components under stress both at warm and at cryogenic temperature. A law to describe the loss of prestress observed in mid-plane of the coils after cooling has been deduced analyzing stress measurements, taken both at 293 K and at 1.9 K.

Interfaces between components have been modeled in ANSYS using contact elements. In some cases, i.e., on the interfaces between coils and collars, contact elements have also been used to simulate material layers not explicitly modeled. This feature, already present in the pre-existent FEM model, has been improved. Some numerical tests have been developed to check the analytical model of the contact. Thanks to the results obtained, contact elements properties have been updated to better reproduce the deformed geometry of the magnet and macros have also been created, which automatically calculate the elements properties with respect to the zone of contact.

Deformations evaluated with structural calculations have been input in ROXIE, a program developed at CERN to compute the magnetic field components. The complete model has been validated by testing it against measurement data, and it has been used to study the effect of geometry errors during manufacturing and their influence on the field quality.

First, deformations calculated on the model have been decomposed in power series, so that it has been possible to describe deformations with a few modes and to check their influence on the field components. Then, a parametrical analysis has been done. The geometry variations with stronger influence on the magnetic field, essentially corresponding to internal collars and coils dimensions, have been identified. Such dimensions have been varied one by one in a range around the nominal values. Each calculation has provided a table containing the sensitivities of the different multipolar components to that parameter variation.

Single parameter sensitivity evaluation is a first stage to give a description of the combined effect that one will find on magnet components. To analyze these effects, a Monte Carlo simulation has been performed overall the set of parameters. In this calculation, all the parameters have been simultaneously varied in a range corresponding to the planned mechanical tolerances. Parameter values have been varied in a random manner over 100 different runs. In this way, a realistic simulation of the possible construction errors on magnet components is obtained.

The results of such analyses have been used to redefine the mechanical tolerances already specified. In particular, it has been possible to relax the requirements for both collar radial and azimuthal dimension. Furthermore, the possibility to take corrective actions on the magnet field after construction has been identified. Since the effects of tolerances on single multipoles are known, corrective actions on the magnets after assembly can be taken, for instance by simply varying the insulation layers between coils and collars.

REFERENCES

[1] Ferracin P., 1998, *Comportamento strutturale e qualita` di campo delle bobine dei dipoli per LHC: studio e confronto con i risultati sperimentali*, Tesi di Laurea, Politecnico di Torino

[2] Vanenkov I., 1999, private communication

[3] Russenschuck S., 1999, ROXIE, the routine for the optimization of magnet X-sections, inverse field computation and coil end design, First international ROXIE users meeting and workshop, Geneva: 1-5

[4] Evans L. R., 1999, The Large Hadron Collider - present status and prospect, IEEE Transactions of applied superconductivity, 10/1: 44-48

[5] LHC Study Group, 1995, *The Large Hadron Collider - conceptual design*, CERN, Geneva

[6] Brianti G., Scandale W., 1992, CERN's Large Hadron Collider: a new tool for investigating the microcosm, Particle World, 3/2: 45-108

[7] Artoos K. et al., 1999, Design, manufacturing status, first results of the LHC main dipole final prototypes and steps towards series manufacture, IEEE Transactions of applied superconductivity, 10/1: 98-102

[8] Spigo G., 1999, private communication

[9] Spigo G., 1995, Facts, observation and measured data gathered during the construction of the Jeumont/GEC-Alsthom superconducting prototype dipole magnet, CERN Internal Note AT/MA 95-115

[10] Mess K.-H., Schmüser P., Wolff S., 1996, *Superconducting accelerator magnets*, World Scientific, Singapore

[11] Perin R., 1996, Field, forces and mechanics of superconducting magnets, CERN accelerator school course on superconductivity in particle accelerators, Hamburg: 71-86

[12] Zienkiewicz O.C., 1977, *The finite element method, 3rd ed.*, McGraw-Hill, London

[13] Ferracin P., Todesco E., Tropea P., 2000, Implementing nonlinear elasticity in ANSYS, CERN Internal Note LHC/MMS 99-04

[14] ANSYS User's Manual for Revision 5.5, Swanson Analysis System Inc., Houston

[15] Todesco E., 1999, private communication

[16] Siegel N., Tommasini D., Vanenkov I., 1997, Design and use of capacitive force transducers for superconducting magnet models for the LHC, 15th International conference on magnet technology, Beijing: 54-58

[17] Bartolini R., Fessia P., Perini D., Scandale W., Todesco E., 1999, Magnetic errors of the LHC dipoles and possible cures, First international ROXIE users meeting and workshop, Geneva: 127-136

[18] Ferracin P., Scandale W., Todesco E., Tropea P., 1999, A method to evaluate the field-shape multipoles induced by coil deformation, 1999 Particle accelerator conference, New York: 3206-3208

[19] Scandale W., Todesco E., Tropea P., 1999, Influence of mechanical tolerances on the field quality in the LHC main dipoles, IEEE Transactions of applied superconductivity, 10/1: 56-59

[20] Scandale W., Ferracin P., Todesco E., Tropea P., Vanenkov I., 2000, Modeling of the thermo-mechanical structure of the main LHC dipole and its influence on field quality, 7th European particle accelerator conference, Vienna: 330-332

[21] Taylor J. R., 1986, *Introduzione all'analisi degli errori*, Zanichelli, Bologna

[22] James F., 1968, *Monte-Carlo phase space*, CERN, Geneva

APPENDIX A

THE ELASTIC CURVE

Using the finite elements code ANSYS a first order modelisation of the coil behavior consists in using a constant elasticity modulus, the tangent one, that is worked out from experimental data. In this case, we obtain an overestimate of the displacements for low stresses and an underestimate for high stresses. This kind of approximation reproduces the average behavior of the coils. Since field quality is very sensitive to coil displacements, one should aim at having a more precise description of the stress strain curve in the model. In the next paragraph, we show how to implement a stress-strain relation that is different from the linear one [10].

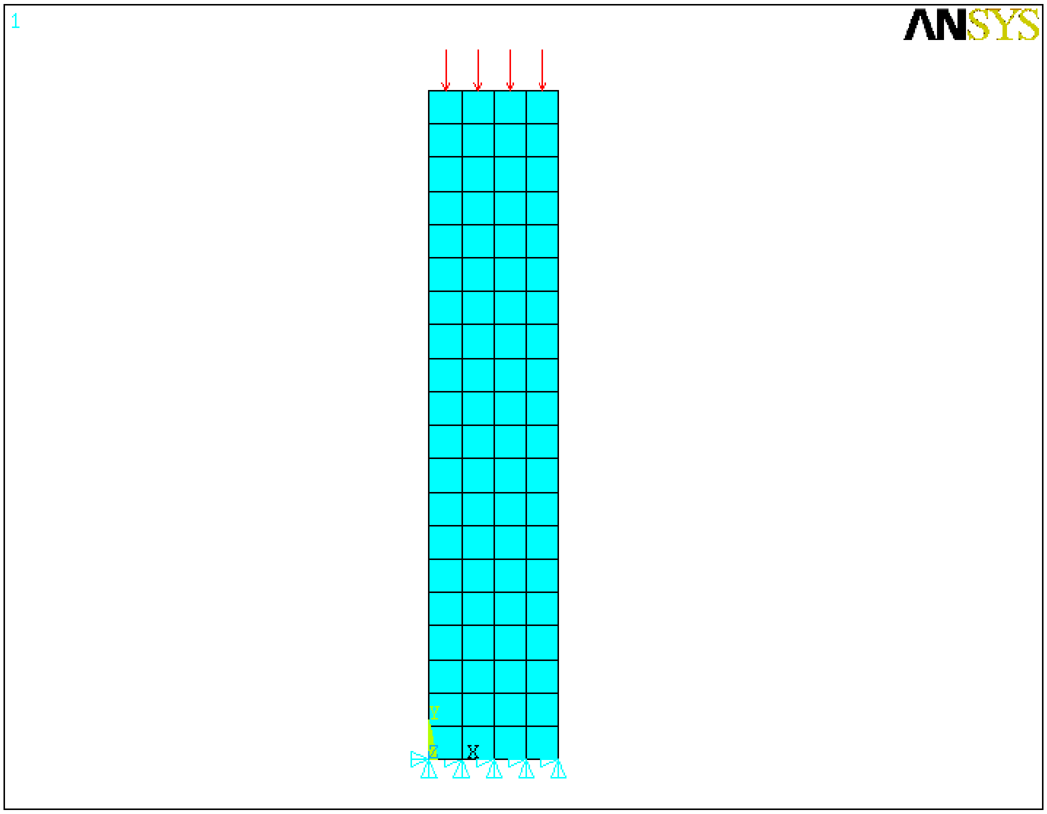

Figure 1: ANSYS model for non-linear behavior tests

First, we take a simplified model, whose analytical solution for deformed geometry under compression is known, using it as a benchmark to check the accuracy of the numerical results. The model consists of a two-dimensional *(x, y)* parallelepiped compressed by a uniform pressure on its top face (see Figure 1). We use PLANE42 elements, which are 2D structural solid elements with the plane strain option (i.e., strain along *z* is zero) [11]. These are the same elements used to model the whole dipole model.

The stress-strain data are inserted in a table using the command "tb, melas", where "melas" indicates a Multilinear Elastic Material (see ANSYS commands list at the end of the paragraph). Its behavior option describes a conservative response in which unloading follows the same stress-strain path as loading and the material behavior is isotropic. This is not the optimum for coils modeling, since radial and azimuthal stress-strain behaviors are different. Anyway, this feature allows one to implement the correct stress-strain relation for the azimuthal direction. An error in the radial direction will be performed, but this is less relevant for our analysis.

We evaluated the displacements in correspondence of 40 different loads between 0 and 100 MPa. We then evaluated the strain according the relation (A.1).

$$\varepsilon_y = \frac{u_y}{l_{0y}} \tag{A.1}$$

where : ε_y = strain along y axe,

u_y = displacement for the evaluated point along x direction,

l_{0y} = starting position in y direction for the evaluated point.

The same values can be obtained directly from the ANSYS post processing asking for the total strain (EPTO) in y direction. Indeed, it must be pointed out the elastic strain (EPEL) does not give the expected results.

We plotted the resulting strains versus the pressure applied and, as we can see in Figure 2, we obtained exactly the same curve given in input.

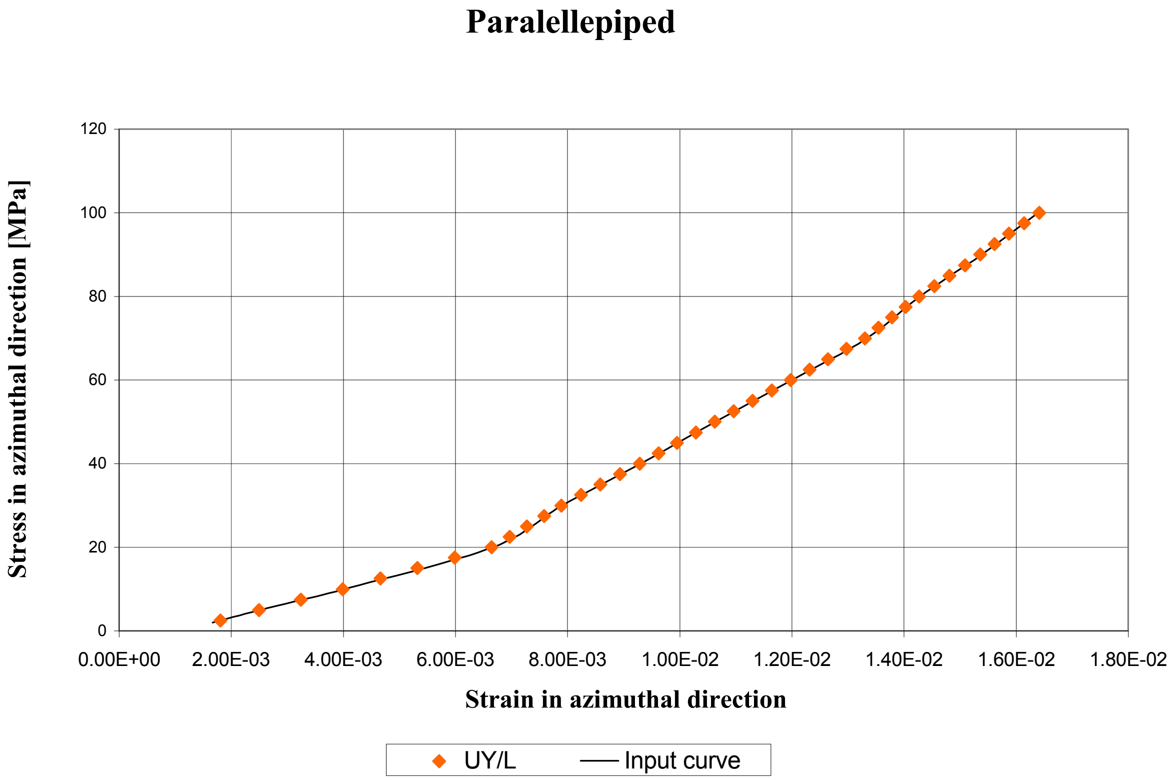

Figure 2: Input and output stress-strain curves for the parallelepiped model

We then implemented the curve on the complete model of the dipole. Both for the inner and the outer coils we input the same stress-strain curve, obtained by a fitting of the experimental data with a second order polynomial. Calculations are carried out at room temperature.

It is not straightforward to calculate an analytical solution for such geometry; moreover, due to coil shape (arc sections) we cannot evaluate the elastic strain simply dividing the displacements by the initial azimuthal length of the coil. However, since we are using a finite element model, it is indeed possible to consider the problem applied to a single element as a linear one, since the curvature radius is large enough with respect to the element dimension and circular shape can be neglected.

We get displacements in azimuthal direction in correspondence of the nodes of twelve elements, positioned in the geometrical center of the conductor blocks, both for right and left coils. For each element, we calculate the strain dividing the difference between the upper and the lower node displacements by their initial distance. Every calculation is made for six different load cases, so that we can cover more or less the whole coil stress working range. In Figure 3, the input curve and the output results are plotted.

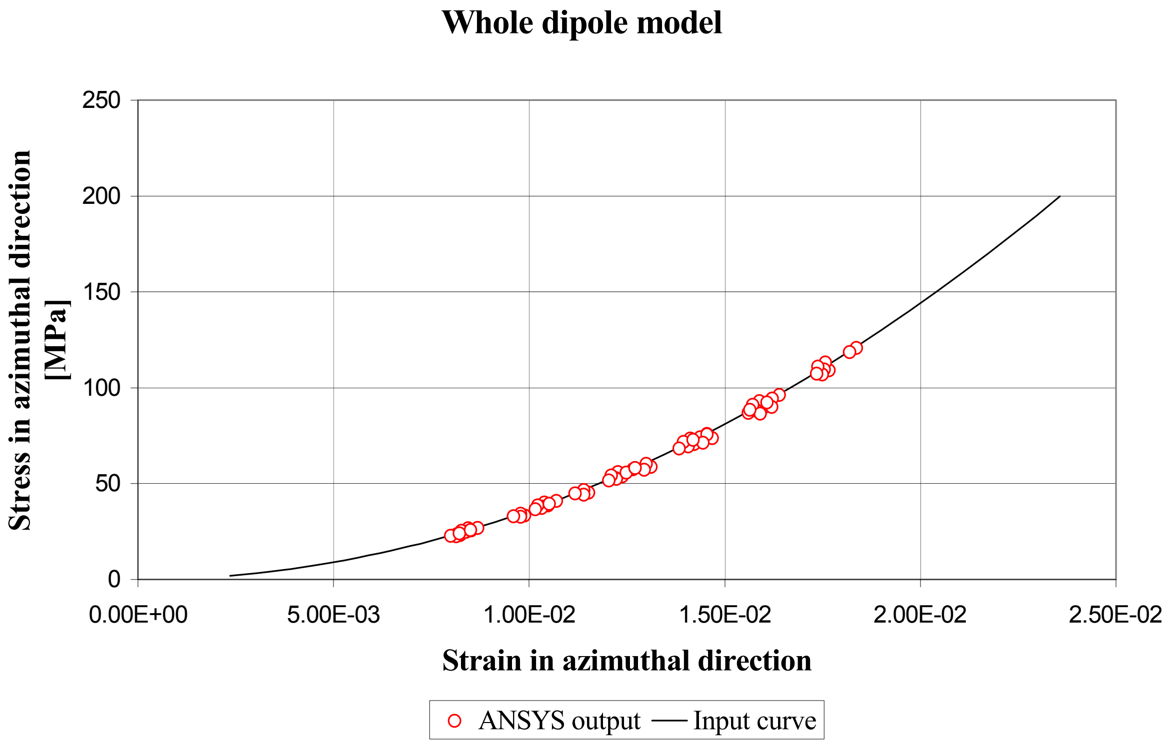

Figure 3: Whole dipole model input and output stress-strain curves

The plot shows a perfect agreement between the input data and the output given by ANSYS. As a consequence of such tests, the non-linear behavior of the coils has been implemented in the dipole model for both warm and cold calculations.

```
ANSYS INPUT FILE FOR THE PARALLELEPIPED MODEL
!               MULTILINEAR ELASTICITY
! initializing constants
```

```
r=2
h=10
load=100          ! 100  MPa
npas=40           ! number of load steps

/prep7
tref,0
! geometry creation
k,1,0,0
k,2,r,0
k,3,r,h
k,4,0,h

l,1,2,4
l,2,3,20
l,3,4,4
l,4,1,20

a,1,2,3,4

! elements
et,1,42
keyopt,1,1,1
keyopt,1,3,3
r,1,1

! material properties
tb,melas,1,1,13
mp,ex,1,100000
tbpt,defi,0,0
tbpt,defi,1.6667e-3,2
tbpt,defi,2.5e-3,5
tbpt,defi,4e-3,10
tbpt,defi,6.6667e-3,20
tbpt,defi,7.8947e-3,30
tbpt,defi,9.3023e-3,40
tbpt,defi,10.6383e-3,50
tbpt,defi,12e-3,60
tbpt,defi,13.3333e-3,70
tbpt,defi,14.2857e-3,80
tbpt,defi,15.3846e-3,90
tbpt,defi,16.3934e-3,100
tbplot,melas,1

! mesh
```

```
asel,all
aatt,1,1,1
amesh,all

! constraints
 nsel,all
nsel,s,loc,y,0
d,all,uy
d,all,ux
nsel,s,,,all
fini

! solution
/solu

! loading
incr=load/npas

*do,i,1,npas
car=incr*i
nsel,s,loc,y,h
sf,all,pres,car
nsel,s,,,all
nsub,2,10,1
autots,on
outres,all,all
solve

! postprocessing
/post1
nsel,s,,,28
/output,ris_ex,out,,append
nlist,all                      ! print all nodes and coordinates
prnsol,u,comp                  ! prints displacements
prnsol,epel,comp              ! prints elastic strain
prns,epto,comp                ! prints total strain
/out
allsel
/solu
*enddo
finish
/eof
```

APPENDIX B

TESTS FOR PROPERTIES COMPUTATION OF THE CONTACT ELEMENTS

In the finite element model of the LHC dipole, the load is given by contact elements. For this reason, a series of tests on contact elements behavior has been done to analyze the influence of their properties and of their response.

A contact element is characterized by two nodes, two stiffnesses (KN and KS), an initial gap or interference (GAP), and an initial element status (START) [11]. First, stiffnesses must be defined as seen in Chapter 3.1.4, taking care of the different kinds of contact we have to represent (with or without an inner layer).

The initial gap defines the gap size (if positive) or the displacement interference (if negative) [11]. Most of the dipole model contact elements are given an interference value to simulate the under pressure assembly of the magnet. Moreover, interference values have been used during parametric analysis to simulate mechanical tolerances. Two simple models can show that increasing the interference of the contact elements between two surfaces has the same consequences than enlarging one of the two surfaces in contact.

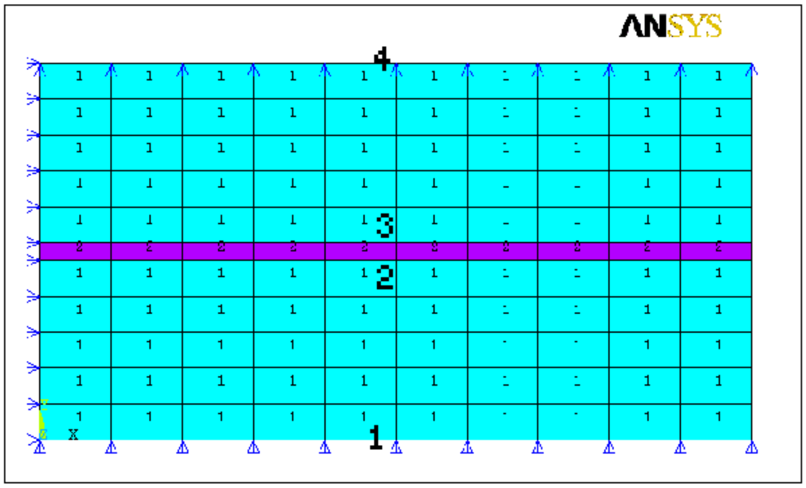

Figure 1: simple model to evaluate interference influence

In Figure 1, the first model is represent, where two different materials are assembled in a sandwich, being the inner one (material number 2) softer that the other. In the second model indeed, material 2 is substituted by contact elements. Both the models are blocked in *y* direction by constraints. The load is applied in the first model increasing the dimension of one of the blocks and maintaining the dimension between constraints equal to a nominal dimension, in the second model simply increasing the interference value of the contact elements. Different calculations have been done (see Table 1), where, for four different nodes, placed at the top and at the bottom of each block, displacements and stresses along the *y* direction are listed. Loads vary from -0.01mm to -0.04 mm.

Table 1: Simulation results for parallelepiped models to test interferences

INT.	NODE	SANDWICH MODEL			CONTACT ELEMENT MODEL		
		sy	*uy*	*Position y*	*sy*	*uy*	*Position y*
[mm]		*[MPa}*	*[mm]*	*[mm]*	*[MPa}*	*[mm]*	*[mm]*
-0.01	1	-33	0.000	0.00	-33	0.000	0.00
	2	-33	-0.003	10.00	-33	-0.003	10.00
	3	-33	-0.007	10.99	-33	0.003	11.00
	4	-33	-0.010	21.00	-33	0.000	21.00
-0.02	1	-67	0.000	0.00	-67	0.000	0.00
	2	-67	-0.007	9.99	-67	-0.007	9.99
	3	-67	-0.013	10.99	-67	0.007	11.01
	4	-67	-0.020	21.00	-67	0.000	21.00
-0.03	1	-100	0.000	0.00	-100	0.000	0.00
	2	-100	-0.010	9.99	-100	-0.010	9.99
	3	-100	-0.020	10.98	-100	0.010	11.01
	4	-100	-0.030	21.00	-100	0.000	21.00
-0.04	1	-133	0.000	0.00	-133	0.000	0.00
	2	-133	-0.013	9.99	-133	-0.013	9.99
	3	-133	-0.027	10.97	-133	0.013	11.01
	4	-133	-0.040	21.00	-133	0.000	21.00

It is immediate to see that both the model built up using the contact elements and the other one give the same results in terms of stresses and final position of the nodes. Using the contact elements indeed, we did not have to modify the initial geometry of the model, but we simply increased the interferences, whose values are reported in the first column, to pass from one load case to the other.

Contact elements can afterwards make easier the mechanical tolerances simulation, but there is still another factor to be considered. Contact elements must be positioned such in a way to be perpendicular to both the surfaces in contact. Otherwise, the transmission of the stresses is not uniform and total, as it should be in a direction that is normal to the surfaces. This assumption comes out from some simple tests made on two different models. They are built up with PLANE42 elements, using two parallelepipeds one onto the top of the other, whose contact surface is modeled with ten CONTAC52 elements. The first model has contact elements built up perpendicularly to the two surfaces, while the second one has contacts a few degrees distorted. A uniform pressure of 40 MPa on the top face loads the models.

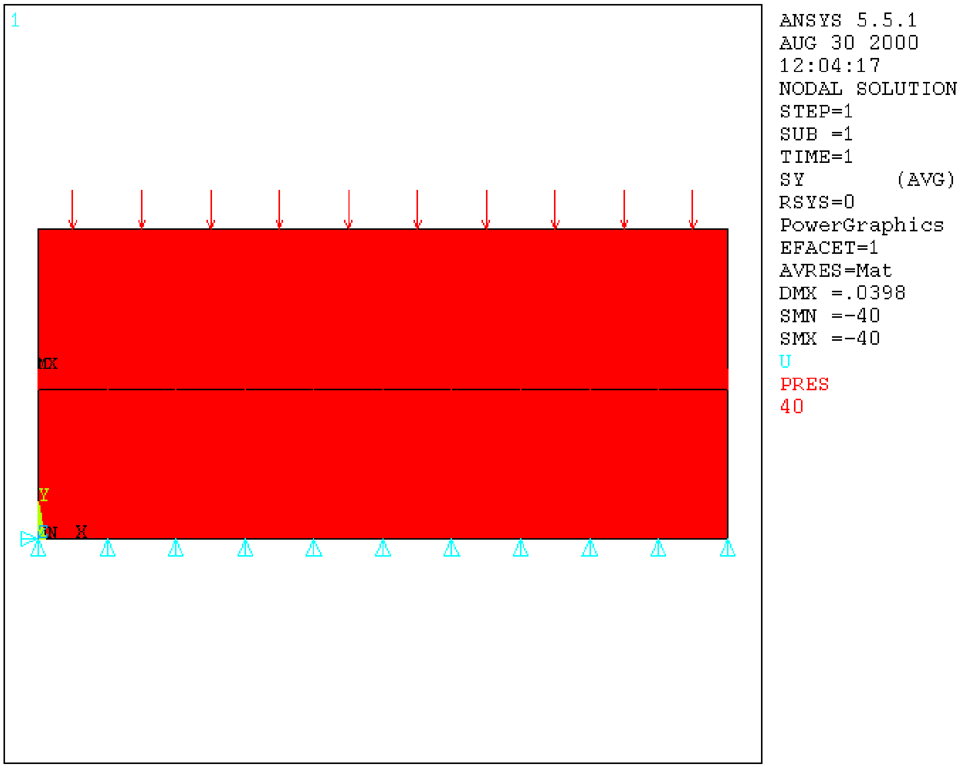

Figure 2: Stress distribution along y direction for the model with perpendicular contact elements

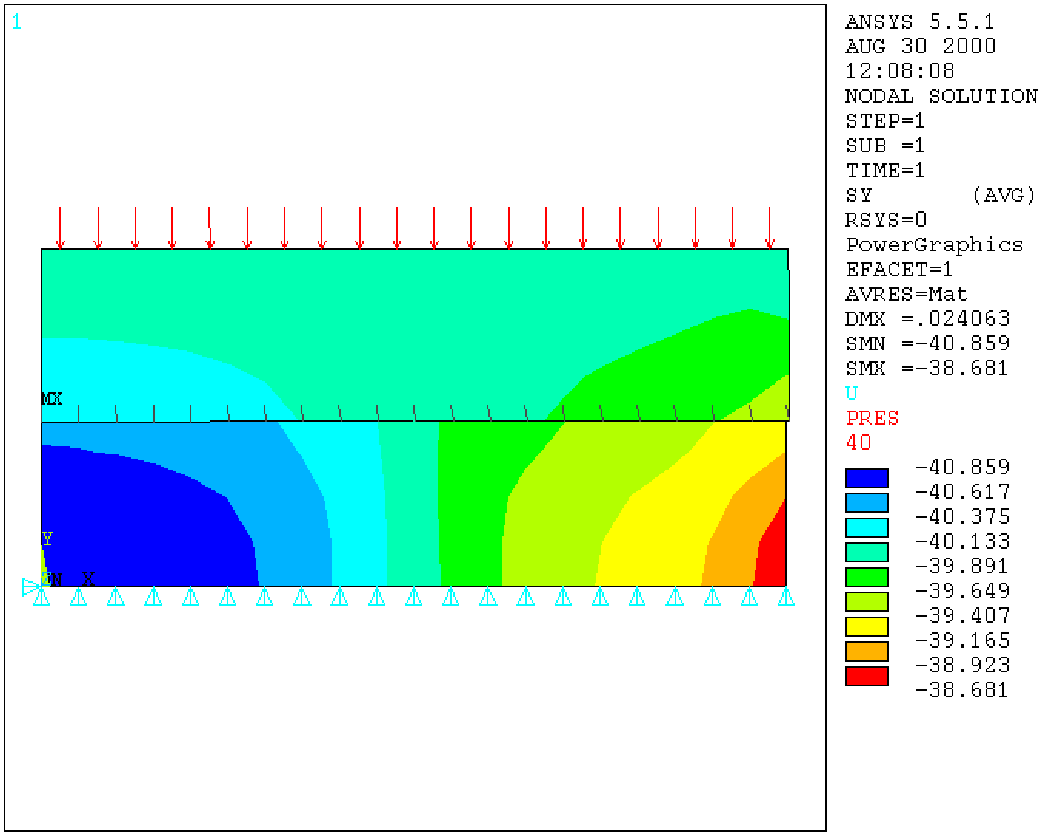

Figure 3: Stress distribution along y direction for the model with distorted contact elements

In Figure 2 and in Figure 3, stress distribution for both perpendicular and distorted contact elements are drawn. It is immediate to see that, while in the first model all the stress in normal direction is uniformly transmitted to the bottom nodes, in the second case this is not true, because some discrepancies exists between the nodal stress inside the model.